

# **Understanding the Sources and Formation Regimes of Present-day PM<sub>2.5</sub> to Mitigate Particulate Pollution in California**

Final Report

Contract No. 21RD010

Prepared for the California Air Resources Board

Principal Investigators:

Don Collins, University of California Riverside

Roya Bahreini, University of California Riverside

Cesunica Ivey, University of California Berkeley

September 25, 2025

## **Disclaimer**

The statements and conclusions in this Report are those of the contractor and not necessarily those of the California Air Resources Board. The mention of commercial products, their source, or their use in connection with material reported herein is not to be construed as actual or implied endorsement of such products.

## **Acknowledgements**

We thank our colleagues at the California Air Resources Board for their useful collaboration in planning the field campaigns and interpreting the resulting datasets. We are especially thankful to the program officers that supported the project: Dr. Toshihiro Kuwayama, Dr. Shang Liu, Dr. Yue Huang, Dr. Morteza Amini, and Dr. Shenglun Wu.

We thank those who made our Wilmington and Bakersfield campaigns possible. Mohammad Sowlat, Payam Pakbin, Olga Pikelnaya, Sumner Wilson, Bill Grant, Robert Wimmer, and Steven Boddeker of the South Coast Air Quality Management District provided the site and many hours of assistance for the Wilmington study. Similarly, we could not have had a successful campaign in Bakersfield without the support of Justin Dingle, Adolfo Garcia, and others from CARB.

## Abstract

This project combined an initial retrospective analysis of trends of fine particulate matter (PM<sub>2.5</sub>) in Riverside, Bakersfield, and San Jose (Task 1) with a series of field campaigns in Riverside, Bakersfield, and Wilmington that generated new datasets to aid in understanding present-day PM<sub>2.5</sub> sources and controls. The generalized additive model (GAM) used in Task 1 provided insight into the meteorological and chemical factors that have the most influence on ambient PM<sub>2.5</sub> concentrations. The four ~1-month field campaigns were designed to build on what was learned from Task 1 and to produce a dataset suitable for additional GAM analysis. The first two were conducted in Riverside, followed by one in Wilmington and one in Bakersfield. An array of online instruments alternated between sampling ambient air, ambient air that is exposed to high oxidant concentrations in a flow reactor, and from each of two environmental chambers located outside. Collectively, the data describes ambient and secondary PM concentrations and composition. The largest contributor to the ambient submicron PM was organic aerosol (58-67%), followed by nitrate in Riverside and sulfate in Wilmington and Bakersfield. The impact on secondary PM formation from the addition of one or more trace gases to an ambient air background was evaluated at all three sites, with a focus on the addition of nitrogen oxides (NO<sub>x</sub>) and ammonia gas. Addition of 10 ppb of ammonia resulted in PM concentration enhancements of as much as ~0.7 μg m<sup>-3</sup> at the Wilmington site. Formation of secondary PM from outside air was evaluated with an oxidation flow reactor. The dependence of the amount of PM formed on the extent of atmospheric photochemical processing and on the presence and amount of liquid water present in the air mixture were found to differ significantly between sites and between days. Two complementary models were used to connect the observed ambient and secondary PM with sources and controls. Positive Matrix Factorization was applied to mass spectra of the organic component of ambient PM to identify responsible sources and processes, while the GAM approach used for Task 1 was applied to understand the factors most closely associated with both ambient PM components and secondary production.

## Executive Summary

The objective of project **21RD010** was to combine retrospective analysis of historical PM<sub>2.5</sub> data with a series of intensive field campaigns to understand both long-term and present-day drivers of particulate pollution. These efforts aimed to support the California Air Resources Board (CARB) by improving understanding of the chemical and meteorological processes controlling PM<sub>2.5</sub> and by informing strategies to meet National Ambient Air Quality Standards (NAAQS).

The project consisted of three major thrusts. **Task 1** analyzed multidecadal PM<sub>2.5</sub> trends using a generalized additive model (GAM) to identify meteorological and chemical variables having the greatest influence on ambient PM concentrations. The analysis incorporated long-term data from the Chemical Speciation Network (CSN) and focused on metrics such as mean bias, root mean square error, and R<sup>2</sup> for PM<sub>2.5</sub> and major species including nitrate, sulfate, ammonium, and organic aerosol. Sensitivity analysis revealed that the factors influencing PM<sub>2.5</sub> varied across regions, with meteorological conditions, precursor concentrations, and secondary formation processes each playing distinct roles. For example, temperature and humidity were closely associated with secondary organic and nitrate aerosol formation. The GAM analysis provided both quantitative and mechanistic insight into seasonal and interannual variability, guiding the subsequent field measurements.

**Tasks 2 and 3** encompassed the design, preparation, and execution of four field campaigns. Each campaign lasted about one month and combined advanced online instrumentation to measure both ambient PM concentrations and potential secondary PM formation. The setups alternated sampling among: (1) ambient air; (2) ambient air processed through an oxidation flow reactor (OFR) to simulate photochemical aging; and (3) air within two parallel environmental chambers—referred to as Captive Aerosol Growth and Evolution (CAGE) chambers. The Accelerated Production and Processing of Aerosols (APPA) reactor complemented the chambers by enabling investigation of the formation of secondary PM under controlled oxidation and humidity conditions. Together, these instruments and techniques enabled simultaneous examination of ambient and secondary aerosol composition and size distributions.

Across all sites, organic aerosol consistently represented the largest fraction of PM<sub>2.5</sub> mass. However, the relative abundance and composition of organic, nitrate, and sulfate PM varied by location and season. At the inland site in Riverside, nitrate contributed significantly during cooler months due to enhanced gas-to-particle partitioning of ammonium nitrate. In contrast, at Wilmington and Bakersfield, with strong marine and industrial influences, PM was impacted more by contributions of organics and sulfate-containing particles. The data demonstrated that secondary aerosol formation, particularly from organic and nitrate species, was sensitive to local precursor availability and meteorological conditions such as temperature, relative humidity, and wind patterns.

The field measurements also investigated the impact of added trace gases on secondary particle formation. Perturbation experiments, in which controlled concentrations of VOCs, NO<sub>x</sub>, or NH<sub>3</sub> were introduced into one of the dual CAGE chambers, provided direct evidence of chemical sensitivities under real-world atmospheric conditions. The results showed that added NO<sub>x</sub> generally had minimal influence on PM<sub>2.5</sub> or its components, while added ammonia enhanced nitrate and, sometimes, organic aerosol

formation, particularly under high relative humidity. The lack of response to added  $\text{NO}_x$  may reflect insufficient  $\text{NH}_3$  in the ambient air during the experiments for formation of ammonium nitrate. Addition of alpha-pinene and toluene led to increased organic aerosol concentration, while addition of isoprene did not and seemed to have an inhibitory effect. The findings are consistent with the expectation that the response of  $\text{PM}_{2.5}$  to changes in precursor emissions is nonlinear and highly dependent on local chemical regimes. The experiments also demonstrated day-to-day variability in potential secondary  $\text{PM}_{2.5}$  formation and its dependence on environmental conditions. Aqueous-phase chemistry is shown to be an important contributor to  $\text{PM}_{2.5}$  formation at each of the three sites.

**Task 4** focused on data analysis and synthesis. Two complementary techniques were used to connect measured PM composition with sources and atmospheric processes. Positive Matrix Factorization (PMF) was applied to the organic aerosol mass spectra to identify and quantify the dominant PM sources and formation pathways. Factors resolved by PMF included hydrocarbon-like organic aerosol (HOA) associated with primary traffic emissions, oxygenated organic aerosol (OOA) linked to secondary formation, and nitrate- and sulfate-rich components indicative of aged aerosols. Correlation analyses between PMF factors and external variables such as temperature, humidity, and gas-phase precursors further highlighted connections between emissions and secondary chemistry. The second approach, expanding the GAM used in Task 1, was applied to the field campaign data to identify the meteorological and chemical drivers most closely associated with both ambient and secondary PM components. The modeling revealed strong regional contrasts, with distinct sets of covariates found to best explain measured concentrations.

The integrated analysis across all sites underscored several consistent patterns. First, organics were the dominant PM component statewide, and their secondary production was modulated by both photochemical and aqueous-phase pathways. Second, while emission reductions in  $\text{NO}_x$  and VOCs have historically lowered  $\text{PM}_{2.5}$  levels, the ongoing decline in the  $\text{NO}_x$ :VOC ratio could alter ozone and secondary aerosol sensitivities in complex ways. Third, ammonia emerged as an important factor in controlling both nitrate and secondary organic aerosol formation, particularly in agricultural and mixed urban regions such as the San Joaquin Valley. Fourth, meteorological variability, especially relative humidity, temperature, and wind direction, significantly influenced day-to-day  $\text{PM}_{2.5}$  concentrations and composition, complicating attribution of changes solely to emissions.

The report concludes that combining long-term data analysis with targeted, comprehensive field measurements provides a powerful framework for evaluating  $\text{PM}_{2.5}$  sources and formation mechanisms. The GAM and PMF approaches together offered complementary perspectives: the former identified causal relationships and meteorological sensitivities, while the latter decomposed complex aerosol mixtures into interpretable source categories. The addition of controlled perturbation experiments using CAGE and aerosol formation under varying conditions using APPA provided a novel experimental capability to isolate and quantify the effects of specific precursors and environmental factors under realistic conditions.

In summary, project 21RD010 successfully achieved its objective of advancing scientific understanding of fine particulate matter sources, chemistry, and controls in California. The results directly support CARB's mission to design effective and equitable air quality policies. The project established a

foundation for future studies that combine observational data and diverse modeling techniques to predict how evolving emissions and climate will shape air pollutant concentrations in the coming decades.

# Table of Contents

Acknowledgements.....	3
Abstract.....	4
Executive Summary.....	5
Table of Contents.....	8
List of Figures .....	9
List of Tables .....	15
1. Task 1 Activities and Results - Multidecadal Analysis of Meteorological and Emissions Regimes for PM <sub>2.5</sub> Across California.....	1
1.1 Background .....	1
1.2 Materials and Methods.....	2
1.2.1 Study Area.....	2
1.2.2 Choice of Covariates .....	3
1.2.3 Air Pollution Data.....	3
1.2.4 Meteorological Data .....	4
1.2.5 Generalized Additive Models (GAMs).....	5
1.2.6 Model Description.....	5
1.2.7 Model Performance Evaluation .....	7
1.2.8 Variable Importance .....	7
1.2.9 Marginal Effects .....	8
1.3 Results and Discussion .....	8
1.3.1 Model Performance Metrics.....	8
1.3.2 Variable Importance .....	9
1.3.3 Marginal Effects .....	12
1.4 Limitations and Future Recommendations.....	15
2. Tasks 2 - 4 Field Campaign Objectives, Sites, and Methods .....	16
2.1 Background .....	16
2.2 Methods.....	16
2.2.1 Site Selection and Timing.....	16
2.2.2 Measurement Instrumentation and Strategy.....	19
2.3 Measurements and Analysis .....	21
2.3.1 Non-refractory PM <sub>1</sub> Composition Measurements.....	21
2.3.2 Equivalent Black Carbon Measurements .....	23

2.3.3	Particulate Size Distributions .....	23
2.3.4	Captive Aerosol Growth and Evolution (CAGE) chambers.....	23
2.3.5	Accelerated Production and Processing of Aerosols (APPA) reactor.....	25
3.	Field Campaign Results .....	27
3.1	Meteorology and Auxiliary Ambient Gaseous Measurements.....	27
3.2	Ambient PM <sub>1</sub> composition.....	31
3.3	Chamber Perturbation Experiments .....	36
3.3.1	VOC Addition Experiments.....	38
3.3.2	NO <sub>x</sub> Addition Experiments .....	42
3.3.3	NH <sub>3</sub> Addition Experiments .....	45
3.3.4	Summary of Perturbation Experiments Results.....	48
3.4	Secondary Aerosol Formation in the APPA Reactor .....	49
3.4.1	Organic and Nitrate Aerosol Enhancements.....	52
3.4.2	Relative Organic Aerosol Enhancements .....	56
3.4.3	Diel Trends .....	59
3.4.4	Organic Aerosol Evolution.....	61
4.1	Source Apportionment of Ambient Organic Aerosol through PMF.....	67
4.1.1	PMF Methodology.....	67
4.1.2	Results and Discussion .....	68
4.2.	Generalized Additive Modeling (GAM) .....	74
4.2.1	Training Data.....	74
4.2.2	Model Description.....	75
4.2.3	Marginal Effects .....	75
4.2.4	Riverside (Mar).....	76
4.2.5	Riverside (Oct).....	79
4.2.6	Wilmington (Mar).....	82
4.2.7	Bakersfield (Apr) .....	88
4.2.8	Summary .....	91
	References .....	92

## List of Figures

Figure 1.1. Map of study area showing locations of CSN sites in California. ....	3
Figure 1.2. Sensitivity analysis results for a) Bakersfield PM <sub>2.5</sub> , b) Riverside PM <sub>2.5</sub> , and c) San Jose PM <sub>2.5</sub> . .....	10
Figure 1.4. Sensitivity analysis results for a) Bakersfield NO <sub>3</sub> <sup>-</sup> , b) Riverside NO <sub>3</sub> <sup>-</sup> , and c) San Jose OC. ....	12
Figure 1.5. Marginal effects plots for the top two most important covariates for the Bakersfield PM <sub>2.5</sub> model (a and b) and the Bakersfield NO <sub>3</sub> <sup>-</sup> model (c and d). ....	13
Figure 1.6. Marginal effects plots for the top two most important covariates for the Riverside PM <sub>2.5</sub> model (a and b) and the Riverside NO <sub>3</sub> <sup>-</sup> model (c and d).....	14
Figure 1.7. Marginal effects plots for the top two most important covariates for the San Jose PM <sub>2.5</sub> model (a and b) and the San Jose OC model (c and d). ....	15
Figure 2.1. Satellite images of all three field sites (top) and of each of sites (bottom).....	17
Figure 2.2. Average PM <sub>2.5</sub> composition at the CSN sites nearest the three study locations. Five years of data from 2015 to 2019 were used to calculate the averages. Winter averages included November, December, January, and February and summer averages included June, July, and August. A factor of 1.4 was used to convert measured organic carbon to total organic aerosol (OA).....	19
Figure 2.3. Experimental configuration for the field studies. The dashed lines represent flow paths for additions to the CAGE chambers while the solid lines represent flow paths for sampling. The colors of the sampling flow paths match those of the source (CAGE A, CAGE B, APPA, or ambient). The thick blue arrows below the CAGE chambers represent the perturbed or unperturbed ambient air that flows across the gas-permeable membrane, as is described below. ....	21
Figure 2.4. Photo and sketch of the CAGE chamber. The labels on the sketch illustrate the connection between conditions inside and just outside of the chambers.....	24
Figure 2.5. Sketch of the APPA flow reactor illustrating the basic operation used to study formation of secondary PM in cloud and fog droplets. ....	26
Figure 3.1. Summary of campaign-average meteorological parameters and auxiliary gas phase measurements during Riverside (Mar). (a) Wind rose of total NR-PM <sub>1</sub> concentrations; (b) Diurnal profiles of ambient temperature, relative humidity (RH), and wind speed; (c) Diurnal profiles of NO <sub>x</sub> , CO, and O <sub>3</sub> . .....	28
Figure 3.2. Summary of campaign-average meteorological parameters and auxiliary gas phase measurements during Riverside (Oct). (a) Wind rose of total NR-PM <sub>1</sub> concentrations; (b) Diurnal profiles of ambient temperature, relative humidity (RH), and wind speed; (c) Diurnal profiles of NO <sub>x</sub> , CO, and O <sub>3</sub> . .....	29
Figure 3.3. Summary of campaign-average meteorological parameters and auxiliary gas phase measurements during Wilmington (Mar). (a) Wind rose of total NR-PM <sub>1</sub> concentrations; (b) Diurnal profiles of ambient temperature, relative humidity (RH), and wind speed; (c) Diurnal profiles of NO <sub>x</sub> , CO, and O <sub>3</sub> .....	30
Figure 3.4. Summary of campaign-average meteorological parameters and auxiliary gas phase measurements during Bakersfield (Apr). (a) Wind rose of total NR-PM <sub>1</sub> concentrations; (b) Diurnal	

profiles of ambient temperature, relative humidity (RH), and wind speed; (c) Diurnal profiles of NO<sub>x</sub>, CO, and O<sub>3</sub>..... 31

Figure 3.5. Summary of NR-PM<sub>1</sub> observations during Riverside (Mar). (a) Time series of NR-PM<sub>1</sub> components (note that the Total mass concentration trace is added to the right axis); (b) Diurnal profiles of the NR-PM<sub>1</sub> mass concentrations; (c) Average distribution of NR-PM<sub>1</sub> components. .... 33

Figure 3.6. Summary of PM<sub>1</sub> and eBC observations during Riverside (Oct). (a) Time series of NR-PM<sub>1</sub> components and eBC (note that the Total mass concentration trace is added to the right axis); (b) Diurnal profiles of the NR-PM<sub>1</sub> and eBC mass concentrations; (c) Average distribution of NR-PM<sub>1</sub> components and eBC. .... 34

Figure 3.7. Summary of PM<sub>1</sub> and eBC observations during Wilmington (Mar). (a) Time series of NR-PM<sub>1</sub> components and eBC (note that the Total mass concentration trace is added to the right axis); (b) Diurnal profiles of the NR-PM<sub>1</sub> mass concentrations; (c) Average distribution of NR-PM<sub>1</sub> components. Note that due to limited eBC data, its diurnal profile and overall average contribution are not calculated. .... 35

Figure 3.8. Summary of PM<sub>1</sub> observations during Bakersfield (Apr). (a) Time series of NR-PM<sub>1</sub> components (note that the Total mass concentration trace is added to the right axis); (b) Diurnal profiles of the NR-PM<sub>1</sub> mass concentrations; (c) Average distribution of NR-PM<sub>1</sub> components. .... 36

Figure 3.9. Time series of particle size distributions in the control chamber (a) and perturbation chamber (b) and mass concentration of organic aerosol in both chambers (c) during the perturbation experiment on April 3, 2022 in Riverside in which alpha-pinene and isoprene were added to the ambient air pulled through one of the two chambers. The orange dotted line indicates the time of sunrise. The perturbation began at 11 pm on April 2, 2022, and continued thereafter. .... 39

Figure 3.10. Time series of particle size distributions in the control chamber (a) and perturbation chamber (b) and mass concentration of organic aerosol in both chambers (c) during the perturbation experiment on April 5, 2022 in Riverside in which alpha-pinene was added to the ambient air pulled through one of the two chambers. The orange dotted line indicates the time of sunrise. The perturbation began at 11 pm on April 4, 2022, and continued thereafter. .... 40

Figure 3.11. Times series of the signal fraction of m/z=44 and m/z=43 in the total organic signal measured by mAMS in the alpha-pinene + isoprene experiment (a) and alpha-pinene-only experiment (b). .... 41

Figure 3.12. Time series of particle size distributions in the control chamber (a) and perturbation chamber (b) and mass concentration of organic aerosol in both chambers (c) during the perturbation experiment on April 6, 2022 in Riverside in which toluene was added to the ambient air pulled through one of the two chambers. The perturbation began at 11:30 am, and continued thereafter. .... 42

Figure 3.13. Time series of particle size distributions in the control chamber (a) and perturbation chamber (b) and nitrate mass concentration for both chambers (c) during the perturbation experiment on October 25, 2022 in Riverside in which NO<sub>2</sub> was added to the ambient air pulled through one of the two chambers. The perturbation began at 9 am, and continued thereafter..... 43

Figure 3.14. Aerosol mass concentrations of nitrate in both chambers during NO <sub>2</sub> perturbation experiments in Wilmington on (a) March 20, 2023 and (b) March 24, 2023. Both perturbations began at 10 am and continued thereafter.....	44
Figure 3.15. Mass concentrations of nitrate aerosol in both chambers during NO <sub>2</sub> perturbation experiments in Bakersfield on April 15, 2024. The perturbations were applied continuously from April 15 to April 16, 2024.....	45
Figure 3.16. Time series of particle size distributions in the control chamber (a) and perturbation chamber (b) and mass concentration of organic aerosol in both chambers (c) during the perturbation experiment on October 27, 2022 in Riverside in which ammonia was added to the ambient air pulled through one of the two chambers. The perturbation began at 11 am and continued thereafter. ....	46
Figure 3.17. Time series of signal fraction of m/z=44 and mass concentration of organics in the perturbation chamber. ....	47
Figure 3.18. Mass concentration of nitrate aerosol in both chambers during NH <sub>3</sub> perturbation experiments in Wilmington on March 28, 2023. The perturbation began at 7:30 am and continued thereafter.....	48
Figure 3.19. Mass concentration of nitrate aerosol in both chambers during NH <sub>3</sub> perturbation experiments in Bakersfield on (a) April 18, 2024, and (b) April 20, 2024. The perturbations were applied continuously from April 17 to April 20, 2024.....	48
Figure 3.20. Time series of organic and nitrate mass concentrations measured in the reactor and ambient air under six experimental conditions: (a) dry seed aerosol at low OH exposure (DRY low OH <sub>exp</sub> ), (b) dry seed aerosol at high OH exposure (DRY high OH <sub>exp</sub> ), (c) aqueous seed aerosol at low OH exposure (AQ low OH <sub>exp</sub> ), (d) aqueous seed aerosol at high OH exposure (AQ high OH <sub>exp</sub> ), (e) cloud droplets at low OH exposure (CLD low OH <sub>exp</sub> ), and (f) cloud droplets at high OH exposure (CLD high OH <sub>exp</sub> ). Data are presented for all four campaigns: Riverside (Mar) (top left), Riverside (Oct) (top right), Wilmington (Mar) (bottom left), and Bakersfield (Apr) (bottom right).....	51
Figure 3.21. Average mass concentration of nitrate and organic aerosol in ambient air and from the OFR for different conditions. (a) Riverside (Mar), (b) Riverside (Oct), (c) Wilmington (Mar), (d) Bakersfield (Apr). ....	54
Figure 3.22. Secondary aerosol enhancement at different reactor conditions relative to that at DRY low OH exp for the first 8h interval (2am-10 am), second 8h interval (10 am-6 pm), and third 8h interval (6 pm-2 am). Box and whisker plots with the average value (dot) and the 10 <sup>th</sup> , 25 <sup>th</sup> , 50 <sup>th</sup> (median), 75 <sup>th</sup> , and 90 <sup>th</sup> percentiles. Data are presented for the four campaigns: Riverside (Mar) (top left), Riverside (Oct) (top right), Wilmington (Mar) (bottom left), and Bakersfield (Apr) (bottom right).....	59
Figure 3.23. Diurnal profiles of SOA concentrations (µg m <sup>-3</sup> ) under each experimental condition: (a) DRY low OH <sub>exp</sub> , (b) DRY high OH <sub>exp</sub> , (c) AQ low OH <sub>exp</sub> , (d) AQ high OH <sub>exp</sub> , (e) CLD low OH <sub>exp</sub> , (f) CLD high OH <sub>exp</sub> , and (g) ambient. Panels (h–l) show the diurnal variation of key ambient gas- and particle-phase species: (h) NO (ppb), (i) NO <sub>x</sub> (ppb), (j) CO (ppb), (k) PM <sub>2.5</sub> (µg m <sup>-3</sup> ), and (l) O <sub>3</sub> (ppb). ....	61
Figure 3.24. Time series and statistical distributions of f43 (f <sub>C<sub>2</sub>H<sub>3</sub>O</sub> ), and f44 (f <sub>CO<sub>2</sub></sub> ) for Riverside (Mar). Box and whisker plots with the average value (dot) and the 10th, 25th, 50th (median), 75th, and 90th percentiles. ....	63

Figure 3.25. Time series and statistical distributions of $f_{43}$ ( $f_{C_2H_3O}$ ), and $f_{44}$ ( $f_{CO_2}$ ) for Riverside (Oct). Box and whisker plots with the average value (dot) and the 10th, 25th, 50th (median), 75th, and 90th percentiles. ....	64
Figure 3.26. Time series and statistical distributions of $f_{43}$ ( $f_{C_2H_3O}$ ), and $f_{44}$ ( $f_{CO_2}$ ) for Wilmington (Mar). Box and whisker plots with the average value (dot) and the 10th, 25th, 50th (median), 75th, and 90th percentiles. ....	65
Figure 3.27. Time series and statistical distributions of $f_{43}$ ( $f_{C_2H_3O}$ ), and $f_{44}$ ( $f_{CO_2}$ ) for Bakersfield (Apr). Box and whisker plots with the average value (dot) and the 10th, 25th, 50th (median), 75th, and 90th percentiles. ....	66
Figure 4.1. Summary of ambient OA PMF results for Riverside (Mar): (a) Mass spectral profiles of the resolved factors; (b) Average contributions of each PMF factor; (c) Diurnal profiles of the average mass concentration of each factor; (d) Diurnal profiles of the fractional contribution of each factor. ....	71
Figure 4.2. Summary of ambient OA PMF results for Riverside (Oct): (a) Mass spectral profiles of the resolved factors; (b) Average contributions of each PMF factor; (c) Diurnal profiles of the average mass concentration of each factor; (d) Diurnal profiles of the fractional contribution of each factor. ....	72
Figure 4.3. Summary of ambient OA PMF results for Wilmington (Mar): (a) Mass spectral profiles of the resolved factors; (b) Average contributions of each PMF factor; (c) Diurnal profiles of the average mass concentration of each factor; (d) Diurnal profiles of the fractional contribution of each factor. ....	73
Figure 4.4. Summary of ambient OA PMF results for Bakersfield (Apr): (a) Mass spectral profiles of the resolved factors; (b) Average contributions of each PMF factor; (c) Diurnal profiles of the average mass concentration of each factor; (d) Diurnal profiles of the fractional contribution of each factor. ....	74
Figure 4.5. Sensitivity analysis for the Riverside (Mar) denoised model. ....	76
Figure 4.6. Marginal effects of (a) $NO_3^-$ , (b) CO, (c) $O_3$ , and (d) $SO_4^{2-}$ for the Riverside (Mar) denoised model with 95% confidence intervals shaded. ....	77
Figure 4.7. Sensitivity analysis for the Riverside (Mar) detrended model. ....	78
Figure 4.8. Marginal effects of (a) $f_{43}$ and (b) $f_{44}$ for the Riverside (Mar) detrended model with 95% confidence intervals shaded. Note: negative covariate values due to detrending. ....	79
Figure 4.9. Sensitivity analysis for the Riverside (Oct) denoised model. ....	80
Figure 4.10. Marginal effects of (a) $SO_4^{2-}$ , (b) CO, (c) RH, and (d) $f_{43}$ for the Riverside (Oct) denoised model with 95% confidence intervals shaded. ....	81
Figure 4.11. Marginal effects of (a) wind speed and (b) wind direction for the Riverside (Oct) denoised model with 95% confidence intervals shaded. ....	82
Figure 4.12. Sensitivity analysis for the Wilmington (Mar) denoised model. ....	83
Figure 4.13. Marginal effects of (a) $NO_3^-$ , (b) CO, (c) temperature, and (d) $O_3$ for the Wilmington (Mar) denoised model with 95% confidence intervals shaded. ....	84
Figure 4.14. Marginal effects of $f_{43}$ for the Wilmington (Mar) denoised model with 95% confidence intervals shaded. ....	85

Figure 4.15. Sensitivity analysis for the Wilmington (Mar) detrended model..... 86

Figure 4.16. Marginal effects of (a)  $\text{NO}_3^-$ , (b)  $\text{Cl}^-$ , (c)  $\text{SO}_4^{2-}$ , (d) CO, (e)  $\text{O}_3$ , and (f)  $f_{44}$  for the Wilmington (Mar) detrended model with 95% confidence intervals shaded. Note: negative covariate values due to detrending..... 88

Figure 4.17. Figure 4.17. Sensitivity analysis for the Bakersfield (Apr) denoised model..... 89

Figure 4.18. Marginal effects of (a)  $\text{NO}_3^-$ , (b)  $\text{SO}_4^{2-}$ , (c)  $\text{Cl}^-$ , (d) CO, (e) temperature, and (f) wind direction for the Bakersfield (Apr) denoised model with 95% confidence intervals shaded. .... 91

## List of Tables

Table 1.1. Summary of terms in Equation 1.5.....	6
Table 1.2. 24-hour, 3-year average annual mean, and 3-year average 98th percentile MB, RMSE, and $R^2$ values for $PM_{2.5}$ and species at the CSN sites under consideration.....	9
Table 2.1. Field campaign summary.....	18
Table 2.2. Measurements and instruments for the field studies. SMPS = scanning mobility particle sizer; CToF mAMS = compact time of flight mini aerosol mass spectrometer; PAX = photoacoustic extincniometer; $\mu m$ = micrometer; $NH_4^+$ = ammonium; $SO_4^{2-}$ = sulfate; $NO_3^-$ = nitrate; $Cl^-$ = chloride; OA = organic aerosol; NO = nitric oxide; $NO_2$ = nitrogen dioxide; $SO_2$ = sulfur dioxide. ....	20
Table 3.1. Location of monitoring sites with auxiliary data used in analysis. ....	27
Table 3.2. Perturbation experiments overview. Experiments ran for the full day except where time ranges are specified.....	37
Table 3.3. Estimated OH exposure ( $molecules\ cm^{-3}\ s^{-1}$ ) under different conditions across the four field campaigns. ....	52
Table 3.4. Estimated equivalent photochemical age (days) under different conditions across four field campaigns, assuming the average atmospheric OH is $1.5 \times 10^6\ cm^{-3}$ .....	52
Table 3.5. Average, median, maximum, and standard deviation of organic aerosol concentrations ( $\mu g\ m^{-3}$ ) at the three sites during March/April campaigns under different conditions. ....	54
Table 3.6. Average, median, maximum, and standard deviation of nitrate aerosol concentrations ( $\mu g\ m^{-3}$ ) at the three sites during March/April campaigns under different conditions. ....	55
Table 4.1. Correlation coefficient of scatter plots between PMF factors and external variables during Riverside (Mar) (a), Riverside (Oct) (b), Wilmington (Mar) (c) and Bakersfield (Apr) (d). ....	70
Table 4.3. Model performance measured as $R^2$ for each campaign and training set.....	75



## **Task Summary and Work Described in This Project**

The five tasks of this project were:

Task 1: Evaluation of long-term trends

Task 2: Design and prepare for field campaigns

Task 3: Conduct field measurements

Task 4: Data analysis

Task 5: Final Report

The results of Task 1 were used to guide some of the measurement approaches and analyses for Tasks 2 – 4. Even so, it was somewhat distinct from the other three. Thus, the activities and results of Task 1 are presented independently of those for Tasks 2 – 4. Tasks 2 and 3 are closely connected, with Task 2 focused on the pre-campaign preparation and Task 3 on campaign execution and initial data analysis. Task 4 builds upon the analysis done as part of Task 3 and adds in datasets from other available sources.

# 1. Task 1 Activities and Results - Multidecadal Analysis of Meteorological and Emissions Regimes for PM<sub>2.5</sub> Across California

## 1.1 Background

As of 2025, large swathes of California remain in nonattainment of the U. S. Environmental Protection Agency (EPA)'s National Ambient Air Quality Standards (NAAQS) for particulate matter (PM) ("Area Designation Maps," n.d.). PM<sub>2.5</sub> nonattainment is concentrated around the state's most populous regions. This puts many millions of California residents at risk of adverse health effects from PM<sub>2.5</sub> exposure. PM<sub>2.5</sub> is associated with adverse health effects, including morbidity and mortality from respiratory and cardiovascular diseases (Ackermann-Liebrich et al., 1997; Atkinson et al., 2001; Dockery et al., 1993; Halonen et al., 2008; Pope et al., 1995; Raizenne et al., 1996; Zanobetti et al., 2000). Furthermore, the EPA has recently revised the PM<sub>2.5</sub> annual standard to 9  $\mu\text{g m}^{-3}$  down from its previous value of 12  $\mu\text{g m}^{-3}$  (US EPA, 2023). For California to meet the revised standard and safeguard public health, the forces driving nonattainment must be well characterized so that effective control strategies can be designed.

Factors influencing high ambient PM<sub>2.5</sub> in California include emissions and meteorology. Emissions of nitrogen oxides (NO<sub>x</sub>) and sulfur oxides (SO<sub>x</sub>) are oxidized to nitrate (NO<sub>3</sub><sup>-</sup>) and sulfate (SO<sub>4</sub><sup>2-</sup>), respectively, while ammonia (NH<sub>3</sub>) emissions form ammonium (NH<sub>4</sub><sup>+</sup>). In addition to these inorganic aerosol species, emissions of reactive organic gases (ROG) provide reactants for secondary organic aerosol (SOA) formation. Further, different aerosol species dominate PM<sub>2.5</sub> pollution in different regions of California. In addition to the geographic variability in PM<sub>2.5</sub> mass profiles, meteorology varies throughout the state and plays a role in high ambient PM<sub>2.5</sub> levels (Zhu et al., 2019). Wind, humidity, and temperature patterns differ, for instance, between coastal regions like the South Coast Air Basin (SoCAB) and inland regions like the San Joaquin Valley (SJV), leading to differential meteorological modulation of PM<sub>2.5</sub> formation regimes. As such, PM<sub>2.5</sub> levels depend on a complex interplay between numerous environmental factors, precluding an immediate understanding of the interaction of meteorological and emissions drivers and their role in PM<sub>2.5</sub> nonattainment in California.

The association between PM<sub>2.5</sub> and a set of covariates can be inferred through the use of generalized additive models (GAMs) (Gao et al., 2022; Pearce et al., 2011a). GAMs enable us to capture complexities in the statistical relationships between PM<sub>2.5</sub> and covariates by fitting nonlinear functions to the covariates of interest. Corresponding to each covariate is a nonlinear fit that can be analyzed independently of others' fits, elucidating the distinct effects of each individual covariate. Moreover, with variable importance ranking, we can identify which covariates are most important for modeling PM<sub>2.5</sub>, thereby identifying potential drivers of high ambient PM<sub>2.5</sub> levels. This makes the problem of understanding PM<sub>2.5</sub> nonattainment in California more tractable.

Knowledge of how different covariates are associated with PM<sub>2.5</sub> throughout California and specifically which covariates drive high ambient PM<sub>2.5</sub> levels can inform regulatory policy design. By taking geographic variability into account and focusing on driving variables, policymakers can better target and tailor regulations to control PM<sub>2.5</sub>.

This regional approach is well suited to informing programs like the California Air Resources Board (CARB)'s Community Air Protection Program ("Community Air Protection Program," n.d.). Implemented in response to Assembly Bill (AB) 617, which seeks to alleviate air pollution impacts on environmental justice communities, the Community Air Protection Program supports community-level efforts to monitor air quality and reduce emissions. As the locations we consider in this paper are all located in AB 617 communities, our results can help inform Community Air Protection Program strategies.

Our main goal is to develop models that characterize the historical  $PM_{2.5}$  response to different chemical and meteorological regimes in California. Exactly how  $PM_{2.5}$  responds to different data variables and how that response differs across the state are not well understood. While Vutukuru et al. (2006) have characterized simulated SOA responses as functions of certain covariates, their analysis examines just one meteorological and two emissions covariates and is limited to the Los Angeles area. More recent work by Nussbaumer and Cohen (2021) produced temperature trends for  $PM_{2.5}$  in the Los Angeles Basin. Numerical modeling by Zhu et al. (2019), however, shows that emissions and meteorological impacts on  $PM_{2.5}$  vary by air basin, indicating that the response curves of Vutukuru et al. and Nussbaumer and Cohen may not be generalizable to the rest of California (Zhu et al., 2019). Our work extends the characterization of  $PM_{2.5}$  response curves to more of California and a greater number of covariates. Moreover, our work incorporates measured rather than simulated data, leveraging California's extensive measurement network. In this paper, we present a series of GAMs for total and speciated  $PM_{2.5}$  at 3 Chemical Speciation Network (CSN) sites in the state of California. These models characterize  $PM_{2.5}$  responses to chemical and meteorological variables throughout the state and how that response differs from site to site.

## 1.2 Materials and Methods

### 1.2.1 Study Area

We construct GAMs at 3 CSN sites in the state of California over many years of data. These sites are located in Bakersfield (2004-2019), Riverside (2001-2019), and San Jose (2011-2019) and are selected as representative of three major geographical regions each located in distinct air basins.

From these sites, we obtain  $PM_{2.5}$  mass and speciation data. We also utilize data from meteorological stations in the proximity of these CSN sites, as well as from the nearest radiosonde stations or the North American Mesoscale (NAM) historical analysis product.

Bakersfield is located in the San Joaquin Valley, which has topography characterized by mountain ranges in the east, west, and south that inhibit the transport of air pollutants out of the valley. Climate in the San Joaquin Valley is characterized by high temperatures, low humidity, and sparse rainfall (Marjollet et al., 2015).  $NO_x$  and VOC emissions in the San Joaquin Valley are dominated by mobile sources and oil and gas production, respectively, while primary  $PM_{2.5}$  emissions come mainly from road and agricultural dust ("ARB Almanac 2013," n.d.).

Riverside is found in the South Coast Air Basin, which is bounded by the Pacific Ocean on the west and mountains to the north and east. The regional climate is characterized by warm, sunny days and stagnant air conditions exacerbated by frequent inversions ("ARB Almanac 2013," n.d.).  $NO_x$  and VOC emissions

are dominated by on-road motor vehicles while primary  $PM_{2.5}$  emissions come predominantly from commercial cooking (“ARB Almanac 2013,” n.d.; Cheung et al., n.d.).

San Jose is in the San Francisco Bay Area, which is a coastal area dominated by the San Francisco Bay, leading to year-round mild temperatures and good ventilation. Emissions are dominated by on-road motor vehicles for  $NO_x$  and VOC and wood burning for primary  $PM_{2.5}$  (“ARB Almanac 2013,” n.d.; “Protecting Public Health in the San Francisco Bay Area,” 2012).

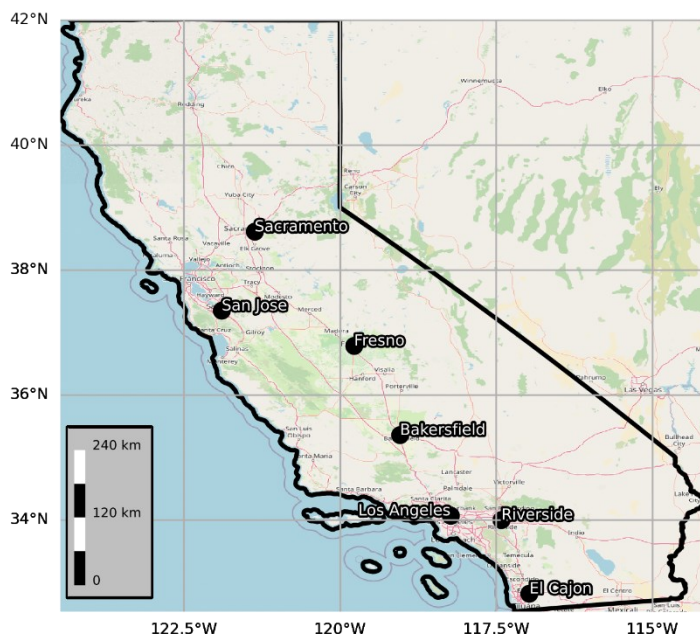


Figure 1.1. Map of study area showing locations of CSN sites in California.

### 1.2.2 Choice of Covariates

We investigate a set of covariates chosen based on existing work as well as first principles (Blanchard et al., 2019; Gao et al., 2022; Ivey et al., 2022; Pearce et al., 2011a; Seinfeld and Pandis, 2016). Our models include meteorological and gaseous covariates. Meteorological covariates include surface and upper-air measurements. Gaseous covariates included are those measured at collocated photochemical assessment monitoring stations (PAMS) and play a role in secondary PM formation (details below).

### 1.2.3 Air Pollution Data

Air pollution data are obtained from the EPA Air Quality System (AQS)’s pre-generated data files. We retrieve daily summary data for all species, although species measurements are not available every day. Species of interest include total  $PM_{2.5}$  mass ( $PM_{2.5}$ ), organic carbon (OC), elemental carbon (EC), nitrate ( $NO_3^-$ ), sulfate ( $SO_4^{2-}$ ), and ammonium ( $NH_4^+$ ). We use  $PM_{2.5}$  as measured at selected  $PM_{2.5}$  Monitoring Network sites and its speciated components as measured at collocated CSN sites, which all sample for 24 hours at a collection frequency of 1-in-3 days (“40 CFR 58.12 -- Operating schedules,” n.d.). The  $PM_{2.5}$

Monitoring Network sites under consideration sample PM<sub>2.5</sub> either with Federal Reference Method (FRM) R&P Model 2025 PM<sub>2.5</sub> Sequential Air Samplers or Federal Equivalent Method (FEM) MetOne BAM-1020 samplers. CSN sites sample 33 aerosol species on Teflon filters and ions on nylon filters in MetOne SASS/SuperSASS samplers. Quartz filters in URG3000N samplers are used to sample carbon. Both carbon species, EC and OC, are measured using the thermal optical transmittance (TOT) method. OC is corrected for sampling artifacts according to Ahangar et al. 2021: we linearly regress OC against PM<sub>2.5</sub> and calculate corrected OC by subtracting the model’s intercept and omitting negative values (Enayati Ahangar et al., 2021).

In addition to PM data, gaseous species are also retrieved from AQS. These include formaldehyde (HCHO), nitrogen oxides (NO<sub>x</sub>), and ozone (O<sub>3</sub>) as representatives of reactants in secondary PM<sub>2.5</sub> formation or, in the case of HCHO, as a tracer of those reactants. These species are measured at PAMS via automated gas chromatography coupled with a mass spectrometer or flame ionization detector, an automated chemiluminescence detector, or a UV absorbance monitor, respectively (Hafner and Penfold, 2018).

#### 1.2.4 Meteorological Data

All surface meteorological data are retrieved from the California Air Resources Board’s (CARB) Air Quality and Meteorological Information System (AQMIS) or meteorological monitors available at CSN-located PAMS (“AQ Data Query,” n.d.). From AQMIS, we retrieved daily maximum solar radiation from the meteorological monitors located nearest to the CSN site under consideration. Daily average relative humidity, daily average surface temperature, and daily average 10-meter wind speed and direction are retrieved from PAMS.

Upper-air meteorology observations, defined as meteorological data measured at the 850 mb air pressure level, are retrieved from the NOAA Earth System Research Laboratory (NOAA/ESRL) Radiosonde Database (“NOAA/ESRL/GSL - RAOB,” n.d.). We used upper-air meteorology at this pressure level following Blanchard et al. (2019) to quantify potential transport effects. The radiosonde station chosen for each CSN site is the nearest one with a data archive that does not restrict our timespan. From NOAA/ESRL, we retrieved wind speed, wind direction, temperature, and dew point depression data. Dew point is recovered from the depression and combined with temperature to calculate upper-air relative humidity using the August-Roche-Magnus equation (Equation 1.1) (Alduchov and Eskridge, 1997).

$$e_s(T) = 6.1094 \exp\left(\frac{17.625 T}{T + 243.04}\right) \quad (\text{Equation 1.1})$$

In Equation 1.1,  $e_s$  is saturation vapor pressure and  $T$  is temperature in Celsius. Based on Equation 1.1, relative humidity is calculated as

$$RH = 100\% \times \frac{e_s(T_d)}{e_s(T)} \quad (\text{Equation 1.2})$$

In Equation 1.2,  $T$  and  $T_d$  are temperature and dew point, respectively (Seinfeld and Pandis, 2016).

In addition to observed upper-air meteorology, we incorporate modeled upper-air data because the Bakersfield CSN site is not within reasonable proximity to active radiosonde launch sites. We used the North American Mesoscale (NAM) 12-kilometer historical analysis product for the same covariates at the

same pressure level as our radiosonde data, namely wind speed and direction (recovered from the U and V components of wind) as well as relative humidity at the 850 mb pressure level.

### 1.2.5 Generalized Additive Models (GAMs)

The modeling tool we employ in this study is the generalized additive model, introduced by Hastie and Tibshirani in 1986 (Hastie and Tibshirani, 1986). We use GAMs because of their ability to capture nonlinear relationships between covariates and the target variable to be modeled and for how they facilitate a covariate-by-covariate analysis of the resulting models (Gao et al., 2022; Pearce et al., 2011a). A GAM is analogous to a generalized linear model (GLM) of the form

$$g(\mu) = \beta_0 + \sum_i \beta_i x_i + \epsilon \quad (\text{Equation 1.3})$$

In Equation 1.3,  $g$  is the link function that represents the relationship between the covariates  $x_i$  and the expected value  $\mu$  of the target variable, where the  $\beta_i$  are the fitted model coefficients,  $\beta_0$  is the intercept, and  $\epsilon$  are the residuals. When  $g$  is the identity function, we have multiple linear regression, whereas we have logistic regression in the case where  $g$  is the logit link  $g(p) = \log\left(\frac{p}{1-p}\right)$ . Many choices for the link function exist.

In contrast to the form of a GLM, which fits constant coefficients of the covariates  $x_i$ , a GAM fits functions of  $x_i$ . GAMs therefore have the form

$$g(\mu) = \beta_0 + \sum_i f_i(x_i) + \epsilon \quad (\text{Equation 1.4})$$

In Equation 1.4, the functions  $f_i$  are fit with smoothing algorithms and typically take the form of splines. The fits are therefore data driven and capture nonlinear relationships naturally.

We fit our GAMs using the package `mgcv` in the R environment for statistical computing (R Core Team, 2021; Wood, 2011, 2000). We use `mgcv`'s `gam` function to fit our models. For full algorithm details see Wood (2011) and Wood et al. (2016) (Wood, 2011; Wood et al., 2016). Briefly, `gam` constructs and iteratively penalizes basis functions for each smoothing spline using one of several smoothing parameter selection criteria such as generalized cross validation (GCV) or restricted maximum likelihood (REML) scores ("R: Generalized additive models," n.d.). For the model specification detailed next, we choose REML as our scoring criterion because it is less prone than GCV to selecting local minima rather than the desired global minimum in the score space ("R: Generalized additive models," n.d.).

### 1.2.6 Model Description

Our base model is

$$\begin{aligned} \hat{y} = \log(\mu) = & \beta_0 + s(\text{TMAX}) + s(\text{WINDS}) \\ & + s(\text{WINDDD}) + s(\text{RH}) \\ & + s(\text{SR}) + s(\text{RH850}) \\ & + s(\text{WS850}) + s(\text{WD850}) \\ & + s(\text{NOX}) + s(\text{HCHO}) \\ & + s(\text{O3}) + \epsilon \end{aligned} \quad (\text{Equation 1.5})$$

In Equation 1.5,  $\hat{y}$  is the model fit and the argument of the log link,  $\mu$ , is the expected value of the target

variable, which is 24-hour average  $PM_{2.5}$  mass or one of its speciated components. We use the log link in our models following precedent (Aldrin and Haff, 2005; Gao et al., 2022; Pearce et al., 2011a). Moreover, we found the log link to reduce bias in our models’ fit against annual 98<sup>th</sup> percentile values as compared with the identity link. As mentioned before,  $\beta_0$  is the model intercept and  $\epsilon$  is the residual. We express spline fits as  $s(\cdot)$ . Table 1.1 summarizes the covariates.

Table 1.1. Summary of terms in Equation 1.5.

Covariate	Description	Units
TMAX	Daily maximum surface temperature	°C
WINDS	Daily average 10 m wind speed	$m\ s^{-1}$
WINDD	Daily average 10 m wind direction	Degrees from north
RH	Daily average surface relative humidity	%
SR	Daily maximum solar radiation	$W\ m^{-2}$
RH850	850 mb daily average relative humidity	%
WS850	850 mb daily average wind speed	$m\ s^{-1}$
WD850	850 mb daily average wind direction	Degrees from north
NOX	Daily average nitrogen oxides concentration	ppb
HCHO	Daily average formaldehyde concentration	ppb of carbon (ppbC)
O3	Daily average ozone concentration	ppb

Each fit  $s(\cdot)$  is a cubic regression spline (cyclic for wind direction) with an extra shrinkage penalty that enables the spline to be penalized to zero at sufficiently high smoothing parameters (“R: Generalized additive models,” n.d.). This manifests as automatic model selection, zeroing out and essentially dropping terms that the smoothing process heavily penalizes, which are the terms that do not contribute explanatory power to the model. This facilitates a data driven approach to distinguish on a site-by-site basis which covariates drive  $PM_{2.5}$  levels and which have less impact.

A further important detail about our model specification is the number of knots chosen for the spline fits. The choice of knot quantity has consequences for fit, with too many knots often resulting in overfitting and too few knots leading to bias from underfitting (Perperoglou et al., 2019). In all of our models, we fit splines with 4 knots. While our use of penalization would help control overfitting if we used many knots, we found no improvement in models fit with more than 4 knots per spline.

Finally, we need to specify an error distribution. Defaulting to a Gaussian distribution produces heteroscedastic residuals with predictions that are biased low at large observations of the target variable. The resulting error distribution suggests a skewed distribution is most appropriate. Therefore, we choose a Gamma distribution, and the resulting models produce homoscedastic residuals.

### 1.2.7 Model Performance Evaluation

Model performance metrics reported are calculated by 10-fold cross validation. Performance metrics include mean bias (MB), root-mean-square error (RMSE), and coefficient of determination ( $R^2$ ). We use the standard  $R^2$  over the adjusted  $R^2$  because our models are penalized and zero out non-explanatory covariates.

$$MB = \sum_{i=1}^N (\hat{y}_i - y_i) \quad (\text{Equation 1.6})$$

$$RMSE = \sqrt{\frac{\sum_{i=1}^N (\hat{y}_i - y_i)^2}{N}} \quad (\text{Equation 1.7})$$

$$R^2 = 1 - \frac{\sum_{i=1}^N (\hat{y}_i - y_i)^2}{\sum_{i=1}^N (y_i - \bar{y})^2} \quad (\text{Equation 1.8})$$

In Equations 1.6-8,  $\hat{y}_i$  are the modeled values,  $y_i$  are the observed values,  $N$  is the number of data points, and  $\bar{y}$  is the mean of the observed data.

### 1.2.8 Variable Importance

While penalization in the model fitting algorithms helps identify driving covariates, we additionally employ a variable importance ranking method to further distinguish between impactful covariates and those that do not hold significant explanatory potential.

We use a variance-based method of global sensitivity analysis for our variable importance determination. Global sensitivity analysis, as opposed to local sensitivity analysis, better characterizes model sensitivity to covariates in the presence of non-additivity, typically manifesting as covariate interactions (Ferretti et al., 2016). Therefore, global sensitivity analysis enables the ranking of covariates by importance while simultaneously testing for the presence of significant interactions.

The measure of importance we calculate is the Sobol' index, which apportions the variance in model output attributable to different covariates. The index of any given covariate is the proportion of total model variance attributable to that covariate (Puy et al., 2021).

To find the first order Sobol' index of a covariate  $x_i$ , we first calculate the model output  $\hat{y}$  after varying all other covariates with fixed  $x_i$ . Borrowing notation from sensitivity analysis, we denote by  $\mathbf{x}_{\sim i}$  all covariates except the  $i$ th, where " $\sim i$ " indicates all except  $i$ . We do this for each value of  $x_i$  and then take the mean of the variance in model output,

$$E[V(\hat{y}|x_i)],$$

where  $E(\cdot)$  and  $V(\cdot)$  are the mean and variance operators, respectively. We note that

$$V(\hat{y}) = V[E(\hat{y}|x_i)] + E[V(\hat{y}|x_i)] \quad (\text{Equation 1.9})$$

where  $V(\hat{y})$  is the model variance. Let

$$V_i = V[E(\hat{y}|x_i)]$$

Then the first order Sobol' index for covariate  $x_i$  is

$$S_i = \frac{V_i}{V(\hat{y})} \quad (\text{Equation 1.10})$$

$S_i$  measures the individual variance contribution of  $x_i$ . We can additionally calculate the total index

$$T_i = 1 - \frac{V[E(\hat{y}|\mathbf{x}_{\sim i})]}{V(\hat{y})} \quad (\text{Equation 1.11})$$

The total index  $T_i$  measures the sensitivity of the model to  $x_i$  and any interactions. If  $S_i < T_i$ , this suggests the presence of significant covariate interactions. On the other hand, if  $S_i \approx T_i$  and  $\sum_i S_i \approx 1$ , this suggests the model is additive and has no significant interactions. Any significant interaction terms can be analyzed with higher order Sobol' indices, which would fix two or more covariates together and compute the model variance attributable to their interactions. Sobol' indices are estimated with the `sensobol` package in R via Monte Carlo methods with 95% confidence intervals bootstrapped (Puy et al., 2021).

### 1.2.9 Marginal Effects

Additionally, we report the influence of individual covariates as marginal effects. We calculate marginal effects as follows. We hold each covariate except that which is under consideration, that is,  $\mathbf{x}_{\sim i}$ , constant at the observation corresponding to the mean fitted value  $\bar{y}$ . We then make predictions as we vary only the covariate of interest  $x_i$  over its observed range. We denote this by

$$ME = 100\% \times [\exp\{s_i(x_i) - s_i(x_i|\bar{y})\} - 1] \quad (\text{Equation 1.12})$$

In Equation 1.12,  $ME$  is the marginal effect,  $s_i(x_i)$  is the spline fit for covariate  $x_i$ , and  $s_i(x_i|\bar{y})$  is the spline fit for covariate  $x_i$  at the value of  $x_i$  that corresponds to the mean fitted value  $\bar{y}$ . The marginal effect is interpreted as the percent change from the mean fitted value as  $x_i$  varies (Pearce et al., 2011b). To see this, note that the full model would include the exponential of the sum of every spline, but we would subtract each spline evaluated at the value corresponding to the mean fitted value  $\bar{y}$ . Since we are holding  $\mathbf{x}_{\sim i}$  constant at that same value, all but two terms cancel, leaving us with Equation 1.12.

## 1.3 Results and Discussion

### 1.3.1 Model Performance Metrics

We report model performance metrics for selected species at the CSN sites in San Jose, Bakersfield, and Riverside. Results are highlighted for  $PM_{2.5}$  and the dominant speciated component for each site. These sites are selected as representatives of three distinct air sheds and geographic regions of California.

We report metrics for the 24-hour average, 3-year average annual mean, and 3-year average 98<sup>th</sup> percentile values, the latter two of which are the values regulated by the  $PM_{2.5}$  NAAQS. All models predict 24-hour average values, so the metrics reported are for 24-hour values and 24-hour values aggregated to annual values. Annual and 98<sup>th</sup> percentile values include an additional rolling average over the preceding two years to produce 3-year backward rolling averages.

Table 1.2. 24-hour, 3-year average annual mean, and 3-year average 98th percentile MB, RMSE, and R<sup>2</sup> values for PM<sub>2.5</sub> and species at the CSN sites under consideration.

Metric	Category	Bakersfield PM <sub>2.5</sub>	Bakersfield NO <sub>3</sub>	Riverside PM <sub>2.5</sub>	Riverside NO <sub>3</sub>	San Jose PM <sub>2.5</sub>	San Jose OC
MB ( $\mu\text{g m}^{-3}$ )	24-hour	-0.22	-0.22	-0.065	0.022	-0.11	-0.018
	Annual	0.22	-0.17	-0.72	-0.40	-0.13	-0.011
	98 <sup>th</sup> Percentile	-2.0	-1.1	-2.5	-1.0	-1.1	-0.30
RMSE ( $\mu\text{g m}^{-3}$ )	24-hour	8.9	4.4	7.8	3.8	4.0	1.2
	Annual	3.4	1.6	3.0	1.5	0.99	0.40
	98 <sup>th</sup> Percentile	6.1	3.0	5.4	2.7	3.3	1.1
R <sup>2</sup> (%)	24-hour	66	67	54	54	68	71
	Annual	77	79	71	75	74	71
	98 <sup>th</sup> Percentile	71	70	67	67	66	76

We report MB and RMSE to characterize the distribution of fitted values around the observed value, with MB representing a measure of central tendency and RMSE measuring spread. Generally, the models perform reasonably well with respect to MB and RMSE, with daily MB values below  $0.25 \mu\text{g m}^{-3}$ , although daily RMSE attains a wider range.

The most salient metric for our objective, however, is the coefficient of determination, R<sup>2</sup>. R<sup>2</sup> measures the proportion of observed variability captured by the model and therefore measures how well the model characterizes the data's behavior, which is our primary goal. From this perspective, our models are performing well. Our worst-performing model still captures 54% of the observed 24-hour average variability.

While our models perform satisfactorily with respect to daily metrics, their performance improves when aggregated to NAAQS values. This suggests our models may be useful for investigating factors that influence attainment or a lack thereof.

In general, our San Jose models are performing best while our Riverside models perform worst. Based on R<sup>2</sup>, one potential reason for this trend is that our models are missing important sources of variability, such as organic vapors or mixing layer height, and the relative importance of those missing sources is greatest in Riverside.

### 1.3.2 Variable Importance

We report variable importance from our sensitivity analysis for each of the three sites under consideration for both their PM<sub>2.5</sub> and speciated component models.

An important result from our sensitivity analysis is the finding that, for each model, the sum of first order Sobol' indices is approximately unity and each covariate's first order index is indistinguishable from its total index. The implication is that there are no significant interactions among the selected covariates in the models. That is, our models are truly additive.

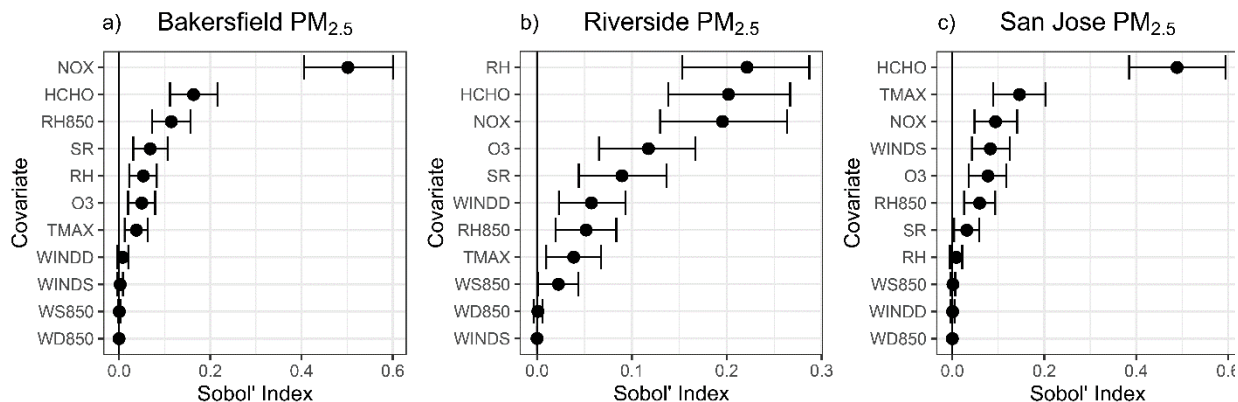


Figure 1.2. Sensitivity analysis results for a) Bakersfield PM<sub>2.5</sub>, b) Riverside PM<sub>2.5</sub>, and c) San Jose PM<sub>2.5</sub>.

We see that Bakersfield PM<sub>2.5</sub> is influenced most strongly by gaseous precursors, suggesting a strong secondary component to Bakersfield PM<sub>2.5</sub>. The only meteorological covariates that contribute variance significantly different from zero are solar radiation as well as upper-air and surface relative humidity, altogether contributing 24% of model variance. NO<sub>x</sub> and HCHO, on the other hand, account for 66% of model variance, with NO<sub>x</sub> alone contributing 50%. The remainder of the model variance is contributed by O<sub>3</sub> and temperature. Given the importance of NO<sub>x</sub>, we might expect nitrate aerosol to be a prominent speciated component of Bakersfield PM<sub>2.5</sub>. In fact, it is the dominant speciated component, as we see in Figure 1.3. Distinguishing between meteorological and gaseous precursor covariates, we find that direct meteorological effects contribute 29% of model variance with the remaining 71% attributable to chemistry.

In Riverside, we see that meteorology plays a more significant role than in Bakersfield, with relative humidity appearing as the most important covariate, contributing 22% of model variance. Altogether, the significant meteorological covariates, i.e., those whose 95% confidence intervals do not cross zero, contribute 48% of model variance, nearly twice as much as in Bakersfield. Gaseous precursors account for the remaining 52%. Therefore, we see a differential in meteorological importance between Bakersfield and Riverside. In the former, less than a third of model variance is attributable to meteorology, while one half is contributed by meteorology in Riverside.

San Jose PM<sub>2.5</sub> is dominated by the influence of HCHO, indicating a strong association with photochemistry and potentially the presence of significant SOA. Indeed, OC, which includes SOA, constitutes the dominant speciated component of San Jose PM<sub>2.5</sub>. Including NO<sub>x</sub> and O<sub>3</sub>, gaseous covariates contribute 66% of model variance, with the remaining 34% attributable to direct meteorology. Thus, San Jose falls in between Bakersfield and Riverside on a spectrum from meteorology-dominance to precursor-dominance with respect to PM<sub>2.5</sub>.

While meteorology influences chemistry, our additive model structure excludes covariate interactions

because they were found to contribute negligible explanatory power at the modeled timescales. Therefore, the effects we see are the main effects attributable to the direct or proxy influences of precursors and meteorology.

We focus next on the dominant speciated components for our sites, i.e., OC in San Jose and  $\text{NO}_3^-$  in Bakersfield and Riverside, as illustrated in Figure 1.3.

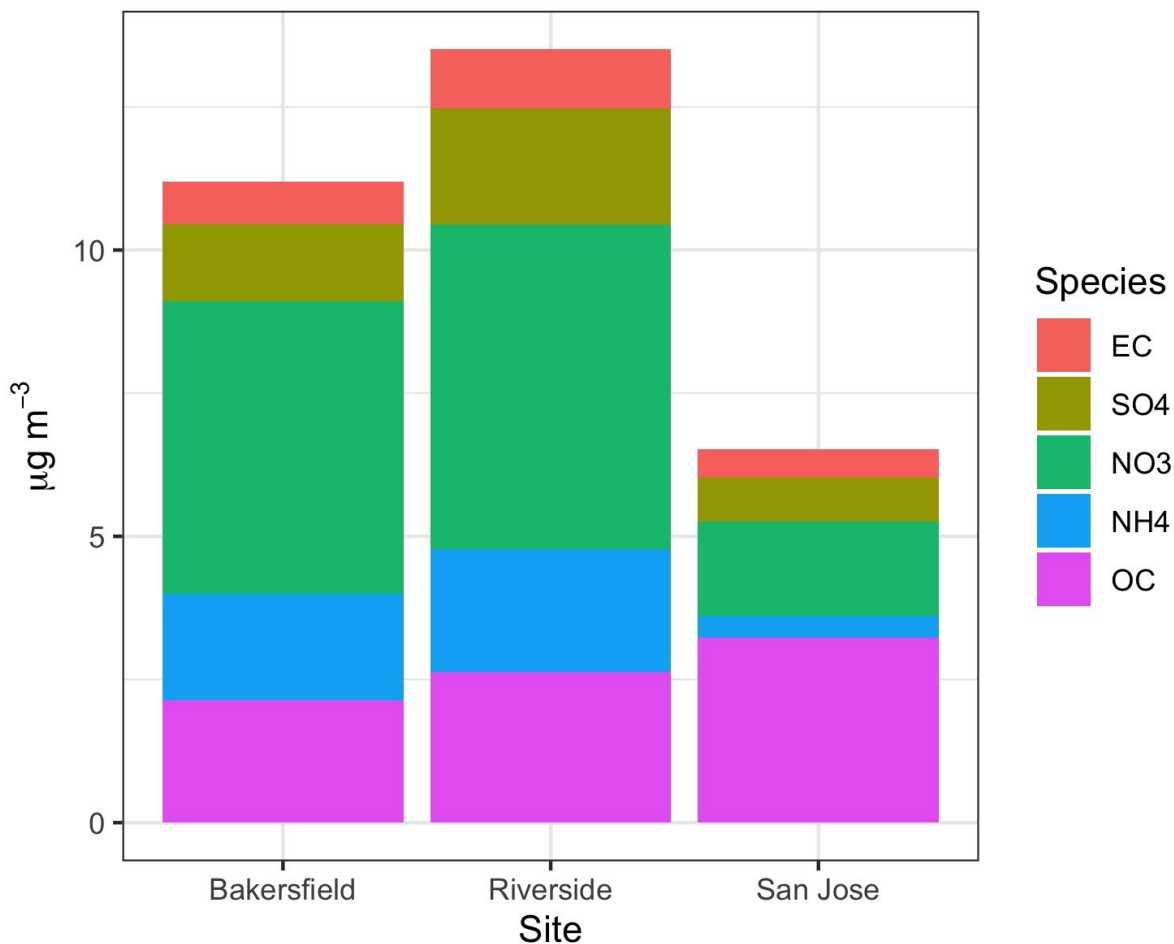


Figure 1.3. Average PM<sub>2.5</sub> speciation by study site.

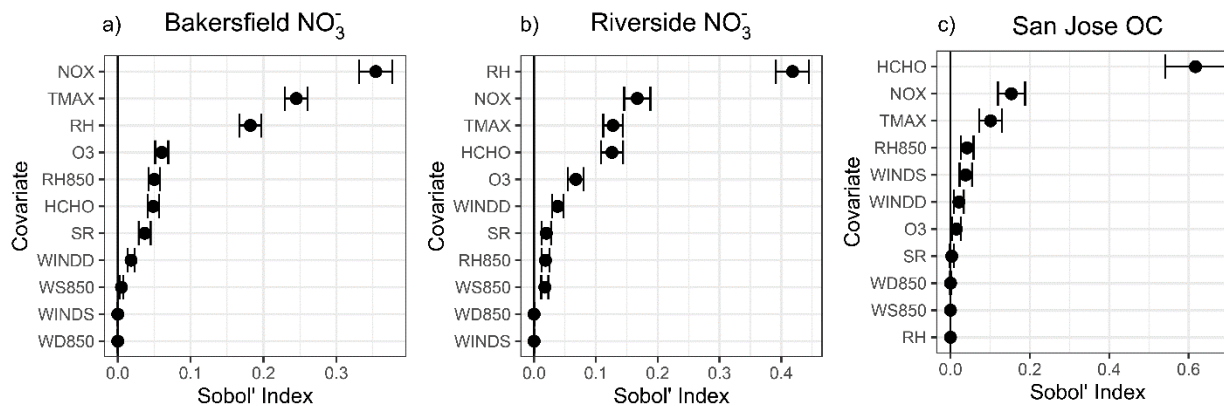


Figure 1.4. Sensitivity analysis results for a) Bakersfield NO<sub>3</sub><sup>-</sup>, b) Riverside NO<sub>3</sub><sup>-</sup>, and c) San Jose OC.

Gaseous precursors account for 46% of Bakersfield NO<sub>3</sub><sup>-</sup> model variance, with NO<sub>x</sub> contributing 35%. This leaves 54% of model variance attributable to meteorology, with temperature being the dominant covariate at 25% followed by relative humidity at 18%.

The Riverside NO<sub>3</sub><sup>-</sup> model's variance is dominated by relative humidity, which contributes 42% of model variance. Altogether, meteorology contributes 64% of model variance, leaving 36% attributable to gaseous precursors. The dominant gaseous precursor is NO<sub>x</sub> at 17%. The importance of relative humidity for both Riverside and Bakersfield NO<sub>3</sub><sup>-</sup> may be at least partly explained by the ion's hygroscopicity and equilibrium partitioning of nitric acid (HNO<sub>3</sub>), which is greater at higher relative humidity and leads to aqueous NO<sub>3</sub><sup>-</sup> production (Seinfeld and Pandis, 2016).

San Jose OC is dominated by HCHO, to which 62% of model variance is attributable. This is likely a result of HCHO acting as a tracer for ROG chemistry that produces secondary OC PM while OC contributes the majority of PM mass (Fig. 1.3). Altogether, gaseous precursors contribute 79% of model variance, leaving 21% attributable to meteorology, with daily maximum temperature dominating meteorological contributions at 10%.

The preceding discussion presents our sensitivity analysis results. However, it must be noted that Sobol' indices measure variable importance with respect to the model and not with respect to observations. A simple back-of-the-envelope calculation might qualify the numbers as follows. With 52% of Riverside PM<sub>2.5</sub> model variance attributable to gaseous precursors and considering that the model explains 54% of observed daily variability, we might conclude that the gaseous precursors we consider in our model explain  $52\% \times 54\% = 28\%$  of observed variability. Similarly, 26% of observed daily variability is explained by the particular set of meteorological variables we consider, leaving 46% of observed daily variability to be explained by some set of covariates for which we have not accounted.

### 1.3.3 Marginal Effects

We highlight marginal effects plots for the top two most important covariates identified from our sensitivity analysis for each site's PM<sub>2.5</sub> and speciated component models. Marginal effects curves are plotted along with their 95% confidence bands. Rug plots are included to indicate observation density.

Because our models are truly additive, as indicated by our sensitivity analysis, we can analyze marginal effects on an individual covariate basis without caveats or the need to qualify our interpretations with any consideration of interactions.

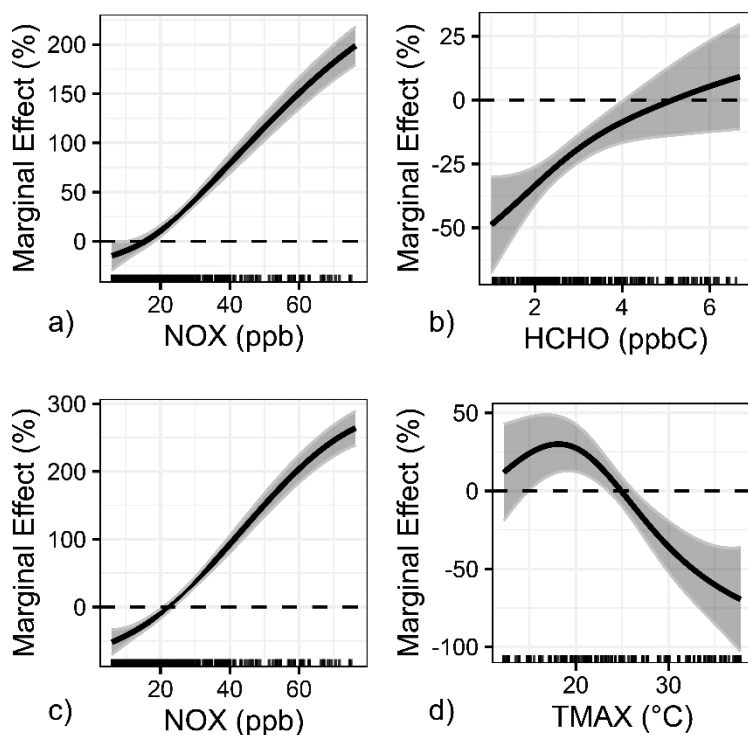


Figure 1.5. Marginal effects plots for the top two most important covariates for the Bakersfield PM<sub>2.5</sub> model (a and b) and the Bakersfield NO<sub>3</sub><sup>-</sup> model (c and d).

For both NO<sub>x</sub> and HCHO in our Bakersfield PM<sub>2.5</sub> model, the marginal effects curves exhibit nonlinear monotonic positive associations. We see that there is a correlation between NO<sub>x</sub> enhancement of PM<sub>2.5</sub> while HCHO levels are correlated with an opposing effect on PM<sub>2.5</sub> formation. The positive association exhibited by NO<sub>x</sub> is consistent with a modeling study by Chen et al. (2014) that suggests reduced NO<sub>x</sub> levels would reduce PM<sub>2.5</sub> in the San Joaquin Valley (Chen et al., 2014). Although that study indicates ROG does not strongly influence PM<sub>2.5</sub> levels, while our HCHO response curve indicates otherwise, a separate measurement study by Zhao et al. (2013) suggests that reduced gaseous organic precursors would reduce SOA levels in Bakersfield (Zhao et al., 2013). This discrepancy arises because Chen et al. modeled wintertime PM<sub>2.5</sub> in Bakersfield, which is dominated by NO<sub>3</sub><sup>-</sup>, whereas Zhao et al. measured summertime organic aerosol, which is the dominant speciated component of PM<sub>2.5</sub> during the summer season. Therefore, we have identified the top two most influential drivers of PM<sub>2.5</sub> in Bakersfield, with the most influential being the wintertime and the second most influential being the summertime driver. This ranking makes sense given that PM<sub>2.5</sub> levels are worst in the winter (Chen et al., 2014). This may also explain the negative marginal effect we see with HCHO. As a tracer for ROG, the influence of HCHO is strongest when the organic PM mass fraction is greatest, which occurs in the summer. Overall PM<sub>2.5</sub> is greatest during the winter, however, so HCHO exhibits a negative marginal effect over most of its range because it is correlated with relatively lower summertime PM<sub>2.5</sub>.

We observe a similar story for  $\text{NO}_3^-$  and  $\text{NO}_x$  as for  $\text{PM}_{2.5}$  and  $\text{NO}_x$ , however, temperature exhibits non-monotonic behavior. This suggests cooler temperatures may be optimal for  $\text{NO}_3^-$  formation, as we see a correlation to that effect. This effect is due to the higher likelihood of ammonium nitrate formation during cooler weather, given its potential to evaporate back to the gas phase in warmer weather (Nussbaumer and Cohen, 2021).

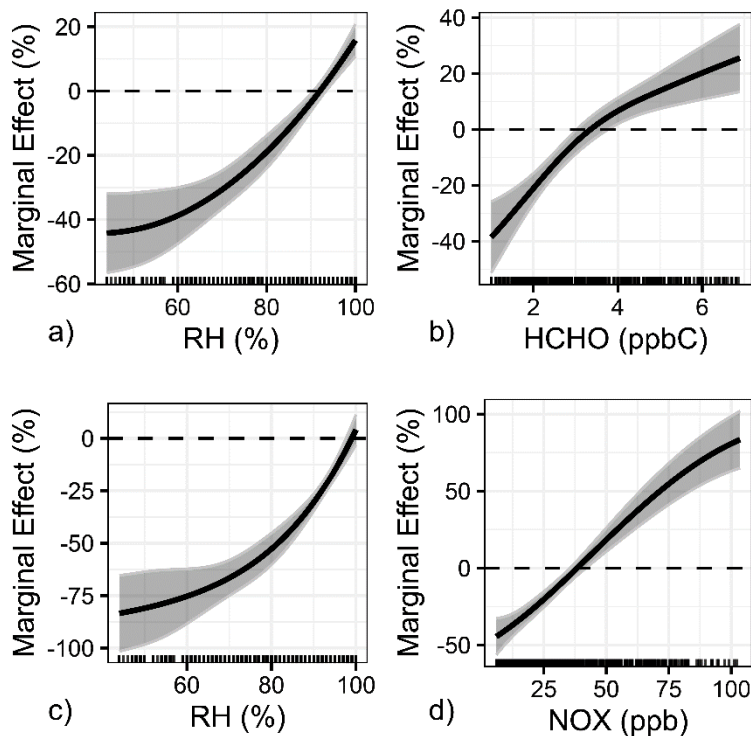


Figure 1.6. Marginal effects plots for the top two most important covariates for the Riverside  $\text{PM}_{2.5}$  model (a and b) and the Riverside  $\text{NO}_3^-$  model (c and d).

In Riverside, relative humidity is correlated with reductions in total  $\text{PM}_{2.5}$  as well as speciated  $\text{NO}_3^-$  over most of its range, but at sufficiently high values relative humidity is correlated with enhancements in  $\text{PM}_{2.5}$  concentrations. The positive association is likely due to  $\text{HNO}_3$  conversion to  $\text{NO}_3^-$  in aqueous aerosol, which explains the  $\text{NO}_3^-$ - $\text{NO}_x$  relationship given  $\text{NO}_x$  conversion to  $\text{HNO}_3$  (Seinfeld and Pandis, 2016). Unlike in Bakersfield, HCHO in Riverside is correlated with enhancements in  $\text{PM}_{2.5}$  over the majority of its range rather than reductions. This is an expected outcome due to the prevalence of SOA formation in the South Coast Air Basin (Woody et al., 2016). While the OC mass fraction in Bakersfield grows from winter (0.13) to summer (0.17), the Riverside OC mass fraction, to a lesser extent, decreases from winter (0.17) to summer (0.16). Therefore, in Riverside we see  $\text{PM}_{2.5}$  enhancement over a greater range of the marginal effect of HCHO than we did for Bakersfield because HCHO is not correlated with relatively less ambient  $\text{PM}_{2.5}$  in Riverside.

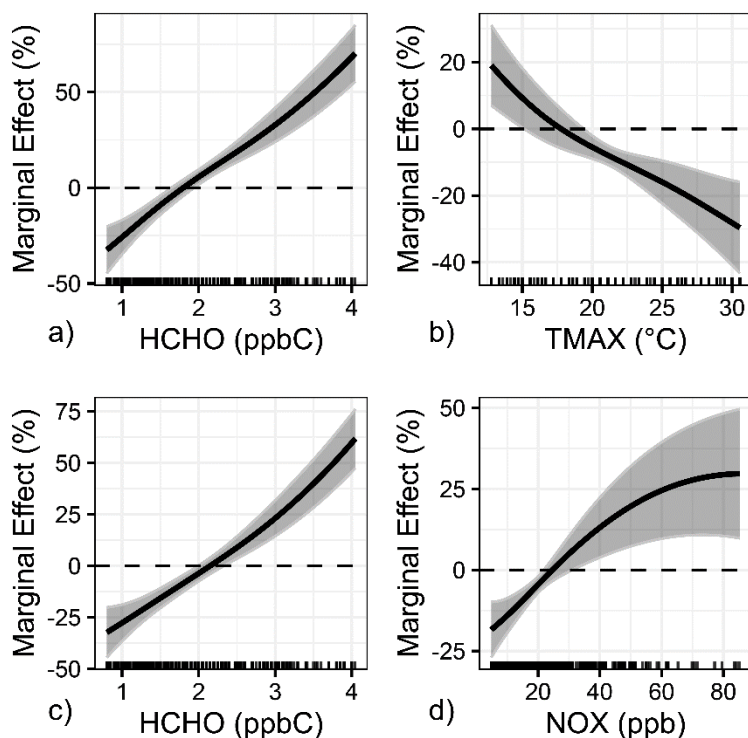


Figure 1.7. Marginal effects plots for the top two most important covariates for the San Jose PM<sub>2.5</sub> model (a and b) and the San Jose OC model (c and d).

San Jose HCHO is correlated with enhancements in both PM<sub>2.5</sub> and OC over most of the covariate's range. We see daily maximum temperature playing an important role, with cooler temperatures correlated with PM<sub>2.5</sub> enhancement. This is because PM<sub>2.5</sub> levels are greatest during cool weather in the wintertime ("Protecting Public Health in the San Francisco Bay Area," 2012). Like HCHO, NO<sub>x</sub> is also correlated with enhanced OC, suggesting contributions from organic NO<sub>3</sub><sup>-</sup> aerosol. Indeed, secondary PM<sub>2.5</sub> in the San Francisco Bay Area is dominated by NO<sub>3</sub><sup>-</sup> ("Understanding Particulate Matter: Protecting Public Health in the San Francisco Bay Area," 2012). OC appears as the dominant speciated component overall, likely in the form of primary PM<sub>2.5</sub>, because of significant wood burning emissions ("Understanding Particulate Matter: Protecting Public Health in the San Francisco Bay Area," 2012). Such emissions also explain the importance of HCHO in its role as an ROG tracer, because ROG are important precursors for SOA and are co-emitted with primary OC from wood burning.

#### 1.4 Limitations and Future Recommendations

We acknowledge the following limitations in our work. Our models do not resolve seasonality, which can lead to different dominant speciated components and emissions sources between seasons. Future work should seek to construct models that account for seasonality, whether through factor interactions or separate models per season. Moreover, our models use point data from stationary observation stations, and therefore are not necessarily generalizable to other locations within their regions or air basins. Future work should test this generalizability by making predictions with the models described in this work on

new data sets within the models' respective regions. We are further limited by data quality and availability through the EPA's AQS. While we have taken steps to correct OC in particular, future work should consider a more careful treatment of blank corrections and may conduct new measurements for greater control over data quality and density. New measurements may especially benefit from the use of more recent measurement techniques, such as aerosol mass spectrometry (AMS). In Bakersfield, the marginal effect of HCHO is negative over a substantial portion of its range, whereas NO<sub>x</sub> remains positive over almost its entire range, only turning negative for very low NO<sub>x</sub> concentrations. This indicates that HCHO precursors, like alkenes and other hydrocarbons, may be more efficacious targets for control, since it would take a smaller reduction in HCHO to reduce PM<sub>2.5</sub> than it would take in NO<sub>x</sub> to achieve the same result.

Compared to Bakersfield, NO<sub>x</sub> controls may be more effective in Riverside because more of the range of the marginal effect of NO<sub>x</sub> is negative. HCHO controls may be similarly as effective as in Bakersfield.

In San Jose, both NO<sub>x</sub> and HCHO marginal effects are positive over most of their ranges, indicating that strong controls for both may be necessary as neither is significantly more efficacious than the other.

## **2. Tasks 2 - 4 Field Campaign Objectives, Sites, and Methods**

### **2.1 Background**

A series of four field campaigns was designed to characterize ambient concentrations and potential for secondary formation of PM<sub>2.5</sub>. The duration of each of the campaigns was approximately four weeks, which was sufficient to capture variability in conditions and concentrations and to permit multiple sensitivity experiments using the outdoor chambers. A multi-tiered strategy was employed that combined measurement of i) ambient PM and precursors, ii) secondary PM formed through gas- and aqueous-phase chemistry in a flow reactor, and iii) secondary PM formed from ambient air in parallel chambers with and without added precursors.

### **2.2 Methods**

#### **2.2.1 Site Selection and Timing**

Sites were selected to represent EJ communities with distinct causes of high PM, while also considering site-dependent costs of travel, site preparation, and materials. The sites selected were Riverside, Wilmington, and Bakersfield, with two campaigns in Riverside and one each in the other two cities. The campaigns are referred to by location and the month on which each study was centered: Riverside (Mar), Riverside (Oct), Wilmington (Mar), and Bakersfield (Apr). The locations are shown in the regional and local satellite images in Figure 2.1. Riverside is representative of the Inland Empire region of southern California where the prevailing westerly winds frequently bring high primary and secondary PM and where there is significant influence from emissions associated with the goods movement industry. Wilmington is one of the areas selected for the Year-1 Assembly Bill (AB) 617 Community Emissions Reduction Program and is significantly impacted by port and truck emissions. Bakersfield experiences high PM<sub>2.5</sub> during the winter like many locations in the San Joaquin Valley (SJV) and is in a region

impacted by significant oil and gas operations, and agricultural operations. All three sites were in SB 535 designated Disadvantaged Communities (“SB 535 Map,” n.d.).

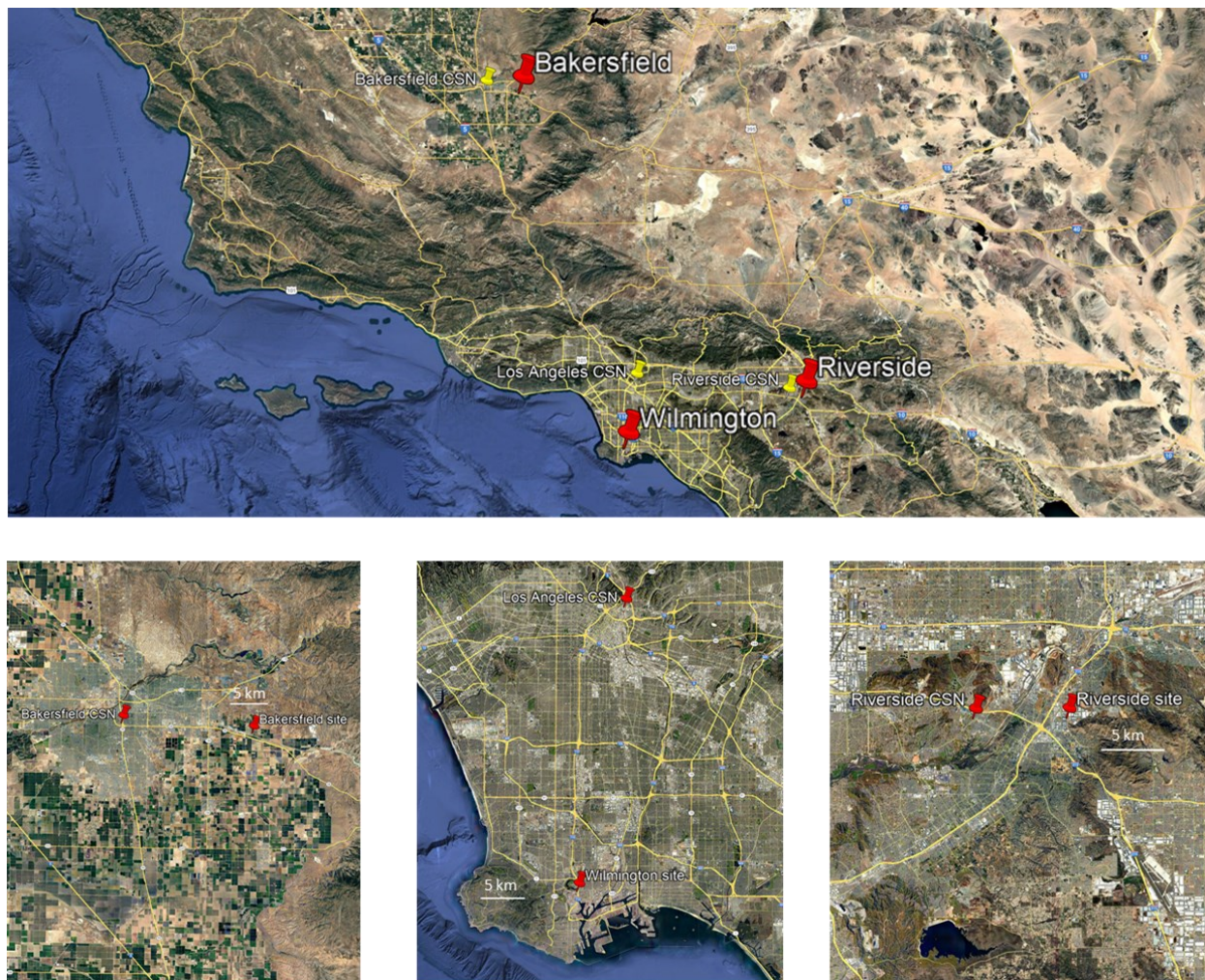


Figure 2.1. Satellite images of all three field sites (top) and of each of sites (bottom).

The Riverside site was on the grounds of the College of Engineering Center for Environmental Research and Technology (CE-CERT), which is near the northern edge of the city in an industrial area that has seen significant warehouse construction over the past several years. The site is about 1.5 km east of I-215, such that freeway emissions impact concentrations of PM and pollutant gases, but not so much as to make the site not representative of the surrounding region. The site is 15 km east of the Mira Loma CARB site, which has among the highest 24-hour  $PM_{2.5}$  design values in the South Coast Air Basin (SCAQMD, 2021). That, combined with being impacted by emissions sources that are common throughout the Inland Empire, made the site an excellent choice for contributing to the development of  $PM_{2.5}$  state implementation plans. As importantly, having the first of the field studies in a location with ease of access and with adjacent laboratory facilities was critical to the success of the overall project because it allowed the research team to optimize the sampling strategy and troubleshoot any initial issues encountered as all of the instruments were configured and operated together for the first time.

The Wilmington site was a South Coast Air Quality Management District (SCAQMD) site used for special studies and some limited longer-term measurements, but not for regulatory monitoring. It is behind a small neighborhood and impacted by emissions from the Ports of Los Angeles and Long Beach a few km to the south to southeast, the 110 Freeway 0.15 km to the east, and the Phillips 66 refinery that begins just meters to the west. The trailer at the site was large enough to accommodate all of the sampling instrumentation and there is a large open area for the mobile chambers.

The Bakersfield site was in an agricultural area to the east of the urban area. It was at the location of the CARB Edison monitoring site (# 15242). It was selected following a lengthy screening process that considered about 10 options throughout the Bakersfield region. Though outside of the urban core, it captures the regional air quality aspects of the area and provides interesting data on emissions and exposure in agricultural areas.

Field studies at each of the sites were planned for winter when 24-hr PM<sub>2.5</sub> exceedances are most common at the sites. For the Riverside site only, an additional study targeted summer conditions when average PM<sub>2.5</sub> is highest. The site coordinates and project periods are summarized in Table 2.1.

Table 2.1. Field campaign summary

	Riverside (Mar) –	Riverside (Oct)	Wilmington (Mar)	Bakersfield (Apr)
Location	34°00'0.08"N 117°20'7.45"W	34°00'0.08"N 117°20'7.45"W	33°46'40.28"N 118°16'54.58"W	35°20'44.63"N 118°51'6.22"W
Project period	March 15–April 7, 2022	September 28– October 27, 2022	February 28– March 28, 2023	March 30–April 22, 2024

Variability in the sources and processes responsible for PM<sub>2.5</sub> at the sites is evident in Figure 2.2, which shows the average composition at the CSN site nearest each of the study locations. Averages were calculated for the 5-year period from 2015 to 2019, excluding July 4 and 5 and January 1. The pie charts labelled NDJF (November, December, January, February) represent averages for the late fall/early winter period of the proposed studies and that labelled JJA (June, July, August) represents the average for the summertime period. Though there are similarities among the sites, there are important differences as well, with sulfate ranging from 4.1% to 14.9%, nitrate from 25.0% to 41.9%, and elemental carbon (EC) from 4.6% to 10.1%. It is likely that there are also significant differences in the organic PM composition, which will be examined using the mini Aerosol Mass Spectrometer (mAMS) data and then exploited for the source apportionment analysis.

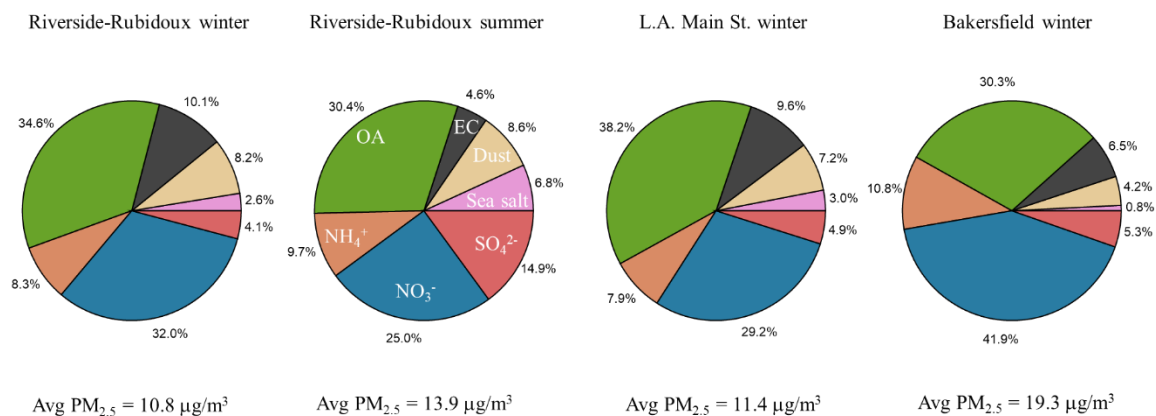


Figure 2.2. Average  $PM_{2.5}$  composition at the CSN sites nearest the three study locations. Five years of data from 2015 to 2019 were used to calculate the averages. Winter averages included November, December, January, and February and summer averages included June, July, and August. A factor of 1.4 was used to convert measured organic carbon to total organic aerosol (OA).

### 2.2.2 Measurement Instrumentation and Strategy

The analyzers used to measure primary and secondary PM and secondary PM precursor gases are summarized in Table 2.2. Relevant details of each of the analyzers are provided below. Some analyzers measured only concentrations in ambient air while others alternated between sampling ambient air and processed air from the Accelerated Production and Processing of Aerosols (APPA) flow reactor and/or Captive Aerosol Growth and Evolution (CAGE) chambers through the use of automated valves that, like many of the measurement systems, were controlled using data acquisition systems and Labview software (National Instruments). The configuration of the instruments and the flow schematic are shown in Figure 2.3. As indicated in that figure, the gas and particle analyzers were located indoors (trailer or building) and the chambers were positioned just outside.

Table 2.2. Measurements and instruments for the field studies. SMPS = scanning mobility particle sizer; CToF mAMS = compact time of flight mini aerosol mass spectrometer; PAX = photoacoustic extinctionmeter;  $\mu\text{m}$  = micrometer;  $\text{NH}_4^+$  = ammonium;  $\text{SO}_4^{2-}$  = sulfate;  $\text{NO}_3^-$  = nitrate;  $\text{Cl}^-$  = chloride; OA = organic aerosol; NO = nitric oxide;  $\text{NO}_2$  = nitrogen dioxide;  $\text{SO}_2$  = sulfur dioxide.

Measurement	Instrument	Time resolution	Samples from	Measurement details
<b><i>Particulate measurements</i></b>				
<b>Size distribution</b>	SMPS (fabricated)	3 min	Ambient, 2 x CAGE, APPA	0.02 – 0.5 $\mu\text{m}$
<b>Size-resolved non-refractory composition</b>	CToF mAMS (Aerodyne)	3 min	Ambient, 2 x CAGE, APPA	$\text{NH}_4^+$ , $\text{SO}_4^{2-}$ , $\text{NO}_3^-$ , $\text{Cl}^-$ , OA
<b>Equivalent black carbon</b>	PAX (DMT) or MA200 (AethLabs)	3 min	Ambient	
<b>Metals and <math>\text{PM}_{2.5}</math> concentration</b>	PX-375 (Horiba)	20 min	Ambient	Al, Ba, Ca, Cl, Cr, Cu, Fe, K, Mn, Ni, Pb, S, Sb, Si, Ti, V, Zn
<b><i>Gas measurements</i></b>				
<b>NO and <math>\text{NO}_2</math></b>	T200U (Teledyne API)	1 min	Ambient	
<b><math>\text{SO}_2</math></b>	T100U (Teledyne API)	1 min	Ambient	
<b><math>\text{O}_3</math></b>	T400 (Teledyne API)	1 min	Ambient	

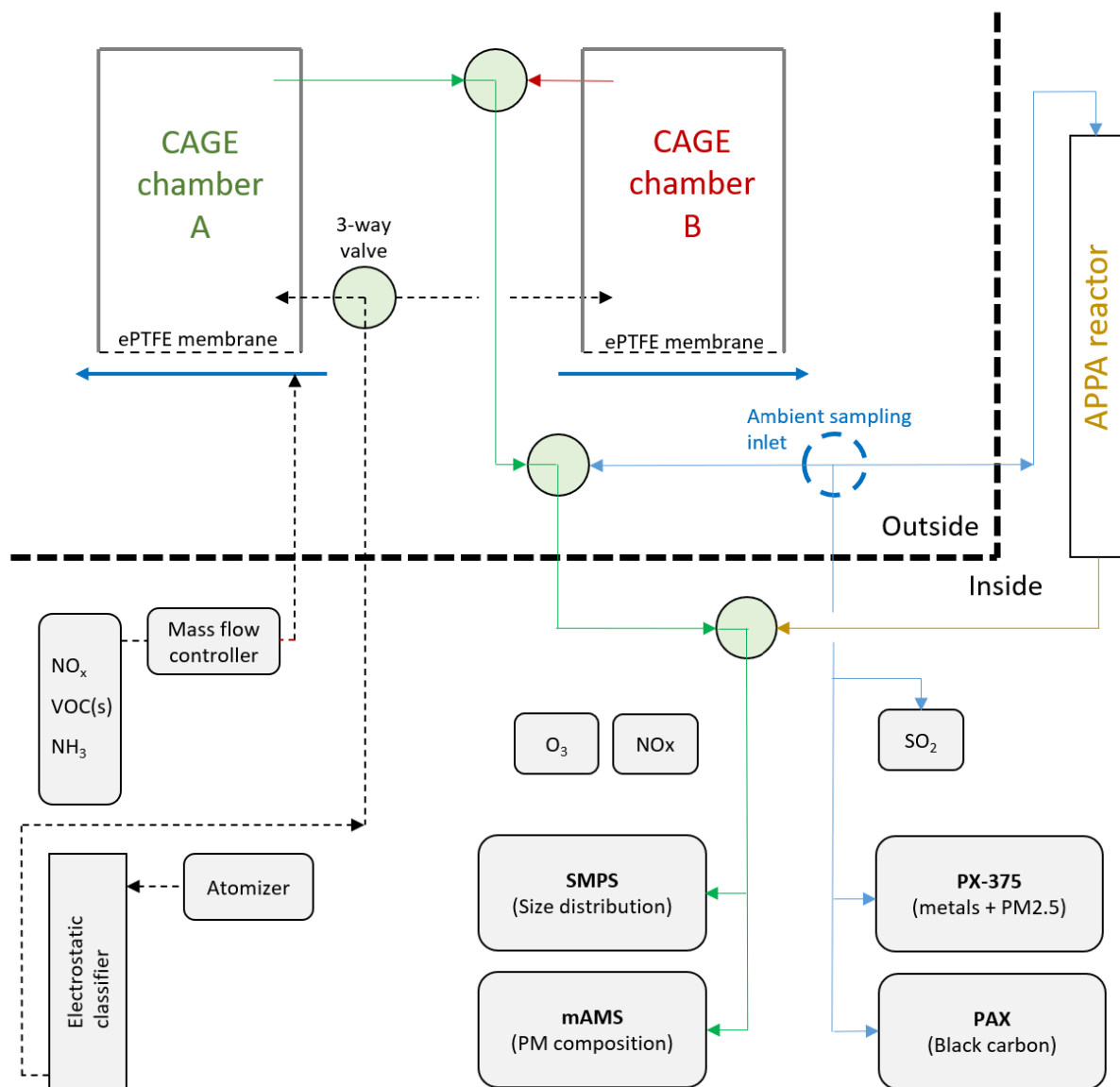


Figure 2.3. Experimental configuration for the field studies. The dashed lines represent flow paths for additions to the CAGE chambers while the solid lines represent flow paths for sampling. The colors of the sampling flow paths match those of the source (CAGE A, CAGE B, APPA, or ambient). The thick blue arrows below the CAGE chambers represent the perturbed or unperturbed ambient air that flows across the gas-permeable membrane, as is described below.

## 2.3 Measurements and Analysis

### 2.3.1 Non-refractory PM<sub>1</sub> Composition Measurements

A mini aerosol mass spectrometer (mAMS) was used to measure fast, size-resolved composition of non-refractory aerosol particles in the submicron range (Bahreini et al., 2012, 2003; Canagaratna et al., 2007;

Dingle et al., 2016; Jayne et al., 2000; Vu et al., 2016). The mAMS is a newer and more compact version of the typical Aerodyne aerosol mass spectrometers; it is equipped with a compact time-of-flight mass spectrometer (C-ToF) and a chopper wheel for obtaining speciated mass distributions. Ambient air at a flow rate of  $\sim 100$  cubic centimeters per minute ( $\text{cm}^3 \text{min}^{-1}$ ) is sampled through a critical orifice and a system of aerodynamic lenses where particles are focused into a narrow beam. After exiting the lens and passing through a skimmer, sample flow is expanded into a differentially pumped chamber where particles travel with different speeds, depending on their size. At the end of the chamber, particles impact on a tungsten vaporizer ( $600^\circ\text{C}$ ) and non-refractory components are vaporized. Vapors are ionized by electron impact and ions are extracted into the mass analyzer. A servo motor is used to move a multi-slit chopper wheel in and out of the aerosol beam to determine the mass spectrum of the ensemble of particles. If the chopper is positioned at its chopped setting, mass distributions of the ensemble particles are determined by measuring the time particles take to travel the known distance of the particle time-of-flight chamber.

During typical operations, aerosol mass spectra and mass distributions were obtained every  $\sim 17$  s. However, on top of this, the mAMS sampled from APPA and the CAGE chambers intermittently as described below. The mAMS data were analyzed using Squirrel (v. 1.62G) and Pika (v. 1.22G) toolkits written in IGOR- Wavemetrics (Allan et al., 2004, 2003). Detection limit ( $2\sigma$ ) for different species in the mass spectrum mode was 0.18-0.26 micrograms per cubic meter ( $\mu\text{g m}^{-3}$ ) for ammonium ( $\text{NH}_4^+$ ), 0.03-0.08 ( $\mu\text{g m}^{-3}$ ) for sulfate ( $\text{SO}_4^{2-}$ ), 0.02-0.04  $\mu\text{g m}^{-3}$  for nitrate ( $\text{NO}_3^-$ ), 0.01  $\mu\text{g m}^{-3}$  for chloride ( $\text{Cl}^-$ ), and 0.08-0.15  $\mu\text{g m}^{-3}$  for organic aerosol (OA). The uncertainty in the measured mass concentrations is estimated to be  $\sim 34$ -38% (Bahreini et al., 2009).

During each campaign, the flow rate-inlet pressure relationship, size calibration, and sensitivity to ammonium nitrate and sulfate were determined and used in the quantification. Furthermore, a composition-dependent collection efficiency (CDCE) was applied following the methodology outlined in Middlebrook et al. (Middlebrook et al., 2012). Quantification of the mAMS species was further refined to match the mass concentration from mAMS with those estimated from size distributions and the mAMS-derived composition-based effective density.

With the typical mass resolution of a C-ToF mass spectrometer (DeCarlo et al., 2008), higher-resolution analysis of the OA spectra was carried out to provide information on the relative contribution of purely hydrocarbon vs. oxygenated hydrocarbon ions to the signal at each fragment (i.e.,  $\text{C}_x\text{H}_y^+$  vs.  $\text{C}_x\text{H}_y\text{O}_z^+$ , where x, y, and z are positive integers) (Bahreini et al., 2012). Furthermore, to constrain the fate of  $\text{NO}_x$  as it relates to aerosol formation, measured ratios of  $\text{NO}_2^+$  to  $\text{NO}^+$  in the ambient air along with the ratios measured when sampling pure ammonium nitrate were used in a formulation previously set forth by Farmer et al. (Farmer et al., 2010). First, the fractional contribution of  $\text{NO}_x^+_{\text{org}}$  ions to total  $\text{NO}_3^-$  is calculated as follows (x):

$$x = \frac{(R_{obs} - R_{AN})(1 + R_{lit})}{(R_{lit} - R_{AN})(1 + R_{obs})} \quad (\text{Equation 2.1})$$

where  $R_{obs}$  is the observed  $[\text{NO}^+]/[\text{NO}_2^+]$  in the ambient data,  $R_{AN}$  is the calculated  $[\text{NO}^+]/[\text{NO}_2^+]$  value from mAMS ammonium nitrate ( $\text{NH}_4\text{NO}_3$ ) calibration in each campaign (1.43-1.65), representing the

inorganic nitrate contribution to  $\text{NO}_3^-$ , and  $R_{lit}$  is the expected  $[\text{NO}^+]/[\text{NO}_2^+]$  from organonitrate ( $\text{RONO}_2$ ) or nitroorganic ( $\text{RNO}_2$ ) species. Previous work indicates that  $R_{AN}/R_{lit}$  is typically 2.75 (Day et al., 2022; Fry et al., 2013), allowing campaign-specific estimation of  $R_{lit}$ . Concentrations of the organic aerosol portion of the measured nitrate are then estimated by the product of  $x$  and the measured total  $\text{NO}_3^-$ .

### 2.3.2 Equivalent Black Carbon Measurements

During Riverside (Mar), Riverside (Oct), and Wilmington (Mar), a Photoacoustic Extinctionmeter (PAX-375, Droplet Measurement Technology) was deployed to estimate concentrations of equivalent black carbon (eBC) from its online measurements of absorbing coefficients ( $\beta_{abs}$ ) at 375 nm using photoacoustic technique (Dingle et al., 2019; Nakayama et al., 2015). Measurements were performed at 1-Hz, with internal aerosol filtering (for removing gaseous interferences) set for every 10 min. By using the mass absorption coefficient of BC at 375 nm ( $\text{MAC}_{375}=11 \text{ m}^2 \text{ g}^{-1}$ ) and the measured  $\beta_{abs}$ , eBC mass concentration ( $C_{eBC}$ ) was estimated from the following equation:

$$\beta_{abs} = \text{MAC}_{375} \times C_{eBC} \quad (\text{Equation 2.2})$$

It is worth noting that this approach has the potential to overestimate the concentration of eBC due to contributions from brown carbon (BrC) at the short wavelength of 375 nm. During Riverside (Mar), the instrument was not set up properly for most of the campaign and did not provide much of a reliable measurement. Furthermore, during Wilmington (Mar), only limited data are available due to water condensation in the PAX inlet.

During Bakersfield (Apr), PAX-375 was not available and eBC was estimated from a micro-aethalometer (MA200, AethLabs). This is a filter-based measurement with automatic tape-advance technology that measures the rate of change of transmitted light through the filter, due to continuous particle deposition on the filter, at 5 wavelengths. The aethalometer was run using its DualSpot sampling mode, which allowed for correcting artifacts related to filter loading, and data were recorded with a 1-min time resolution. Mass concentration of eBC is estimated internally from the measurements at 880 nm.

### 2.3.3 Particulate Size Distributions

The PM size distribution from 0.015 to 0.5 micrometer ( $\mu\text{m}$ ) diameter ( $D_p$ ) was measured by a scanning mobility particle sizer (SMPS, fabricated in-house). The measurement time resolution was about 3 minutes (min). The SMPS employed a high flow differential mobility analyzer to reduce the time needed for each measurement. The measured size distributions were used to calculate quantities such as PM mass concentration for comparison with other PM measurements.

### 2.3.4 Captive Aerosol Growth and Evolution (CAGE) chambers

The sensitivity of PM concentration and composition to changes in precursor gas concentrations was investigated using the CAGE chambers. These are the most recent versions in a series of portable chambers that employ the same basic function and methodology. The first generation chambers were used to study atmospheric processing of soot particles in Houston and Beijing (Peng et al., 2017, 2016). Second generation chambers were used to study the contributions of important oxidants and precursor

gases to daytime and nighttime secondary PM production at a site north of Houston, Texas (Sirmollo et al., 2021). Just prior to their use in the first of the campaigns of this project, the same two CAGE chambers were operated at a Department of Energy site in Oklahoma (Zhu et al., 2025).

A photo and sketch of the redesigned chambers are shown in Figure 2.4. At the core of each of the two identical systems is a 2 m<sup>3</sup> cylindrical all-Teflon chamber that rotates along its horizontal axis to minimize particle loss. Each chamber is suspended in a powder coated stainless steel rectangular enclosure that is covered in UV-transmitting acrylic panels (Spartech Solacryl SUVT). The use of UV-transmitting materials for the chamber and enclosure, together with a UV-reflective gasket sheet below the chamber, results in a solar spectral intensity inside that is similar to that just outside.

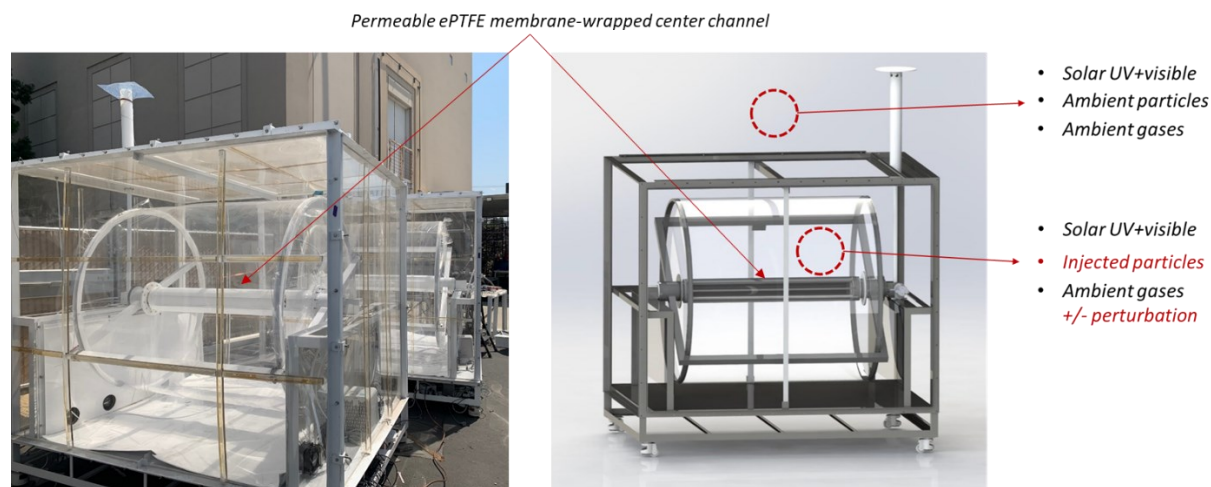


Figure 2.4. Photo and sketch of the CAGE chamber. The labels on the sketch illustrate the connection between conditions inside and just outside of the chambers.

Approximately 75 liters per minute (L min<sup>-1</sup>) of ambient air is pulled into an inlet from about 1 m above each chamber and filtered through an all-Teflon particle filter. For this project, controlled injections of gases such as NO<sub>x</sub>, VOCs, or NH<sub>3</sub> can be added to the ambient air flow for one of the two chambers. The ambient or perturbed ambient air is then directed through a channel through the center of the chamber that is wrapped in a permeable expanded polytetrafluoroethylene (ePTFE) membrane, across which gas-phase species are exchanged with the air in the chamber. The transmission efficiency of the ePTFE membrane and the resulting relationship between ambient and chamber gas phase composition were evaluated by Zhu et al. (2024). Trace gas concentrations in the chamber can be explained by treating the volume as a continuous stirred-tank reactor (CSTR). The resulting rate of change of the concentration of any trace gases can then be expressed as

$$\frac{dC_{ch}}{dt} = P - L + \frac{Q_{ex}}{V_{ch}} C_{amb} - \frac{Q_{ex}}{V_{ch}} C_{ch} \quad (\text{Equation 2.3})$$

Where  $C_{ch}$  is the concentration in the chamber,  $C_{amb}$  is the ambient concentration,  $V_{ch}$  is the volume of the chamber (2 m<sup>3</sup>),  $P$  and  $L$  are the per unit volume rates of chemical production and loss in the chamber, respectively, and  $Q_{ex}$  is the effective exchange “flow rate” across the ePTFE membrane, which was calculated from the recorded time series and was found to result in a turnover time,  $\tau_g$ , of about 65 min. For reactive species, chemical loss and/or production over that turnover time in the chambers may be significant. For free radicals and other highly reactive or condensable species with typical atmospheric

lifetimes much shorter than 65 min (e.g., hydroxyl radical, OH $\cdot$ , and nitrate radical, NO $_3\cdot$ ), exchange across the ePTFE membrane is insignificant and  $P \approx L$ .

In contrast to gases, for which the composition inside the chamber tracks that outside, the ambient and chamber particle populations are distinct because the ePTFE membrane is non-permeable to particles. Only particles that are intentionally injected into the chambers are present and those are exposed to the ambient- or perturbed ambient-mirroring environment until being sampled or lost to the walls. Monodisperse ammonium sulfate seed particles are generated by atomizing a solution with a Collison atomizer (TSI 3076), drying with a molecular sieves diffusion dryer, and separating a narrow size range (0.2  $\mu\text{m}$  most often, with 0.05  $\mu\text{m}$  for select experiments) with a differential mobility analyzer (DMA) configured as an electrostatic classifier. Injections of fresh particles were generally timed to maintain a stable concentration of 0.2  $\mu\text{m}$  particles or to re-establish a population of 0.05  $\mu\text{m}$  to track over time. The monodisperse particle mode is injected into one of the chambers at a time. Particle retention is maximized by rotating the chambers and by taking steps to minimize static charge on the Teflon surfaces. With this approach, experiments are continuous and measurements are made 24 h day $^{-1}$ . The size distribution and composition of the particles in each chamber was intermittently measured, with a repeated sampling sequence of Chamber A  $\rightarrow$  Chamber B  $\rightarrow$  OFR (described below)  $\rightarrow$  ambient, such that sample is extracted from each chamber only 1/4th of the time in order to minimize the loss rate of the captive particles.

### 2.3.5 Accelerated Production and Processing of Aerosols (APPA) reactor

Formation of secondary PM in the CAGE chambers proceeds at a rate comparable to that in the surrounding air. Though that rate varies considerably with time of day, pollution level, and meteorology, the timescale of conversion of precursors to PM is typically hours. To characterize short-term variability in PM precursors and to explore different formation pathways, an oxidation flow reactor (OFR; e.g., Kang et al., 2007) was used to accelerate chemistry that would occur over hours in the atmosphere to occur in just a couple of minutes. Ambient air was continuously introduced into the inlet of the OFR and the secondary PM that formed from it was intermittently measured with both the particle sizing instruments and the mAMS. As described by Xu et al. (2024), the core of the OFR used is a Perfluoroalkoxy (PFA) Teflon flow tube in which high concentrations of OH $\cdot$  result in equivalent atmospheric exposure ranging from a few hours to more than a week. Ambient air is pulled into the top of the reactor and reactive components are rapidly oxidized as they travel through the reactor tube. Secondary PM that forms is sampled from the outlet at the bottom of the reactor and measured with the particle sizing instruments and the mAMS.

To generate OH·, O<sub>3</sub> is produced externally (Jelight Co., Inc. model 610) and introduced into the reactor, where it is photolyzed by 254-nm emitting germicidal UV lamps. The resulting excited oxygen atom (O(<sup>1</sup>D)) reacts with water vapor to create OH· concentrations ranging from ~10<sup>8</sup> to ~10<sup>10</sup> cm<sup>-3</sup>, which, for the average reactor residence time of 120 seconds, results in equivalent exposure, or photochemical age, of between about 2.5 h and 1 week for an assumed average atmospheric [OH·] of 1.5 x 10<sup>6</sup> cm<sup>-3</sup>. The reactor assembly is enclosed in an aluminum shell with all interior surfaces covered by highly UV-reflective 6 millimeter (mm) thick PTFE gasket (Intertech, Inc. SQ-S) to maximize UV intensity uniformity throughout the reactor. A pair of 254-nm emitting UV lamps are mounted inside the aluminum enclosure and outside of the reactor. The UV intensity is controlled using a dimmable ballast and is typically maintained at a level that results in photolysis of 15% of the added O<sub>3</sub>, which represents a balance between maximizing the OH·/O<sub>3</sub> concentration ratio (high UV desirable) and minimizing the OH· gradient over the length of the reactor (low UV desirable).

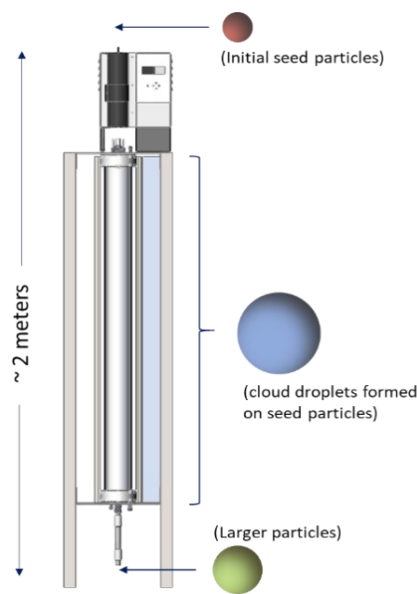


Figure 2.5. Sketch of the APPA flow reactor illustrating the basic operation used to study formation of secondary PM in cloud and fog droplets.

The APPA reactor differs from that of all other OFRs described in the literature in that it is also used to simulate aqueous phase chemistry in aerosol liquid water and in clouds and fogs. To do so, temperature is precisely controlled by circulating water from a chiller between the PFA reactor and a quartz tube surrounding it. Droplets with a median diameter of about 3.5 μm are formed on monodisperse seed particles using a modified Spot Sampler (Aerosol Devices, Inc.) and introduced into the top of the reactor, as depicted in Figure 2.5. Ammonium sulfate was used during all of the field studies in part because it is not refractory and does not accumulate in the mAMS as would other types used for other experiments. The initial dry seed particle composition, concentration, and size were the same for all humidity conditions to facilitate isolation of the role of water content on measured secondary PM formation. The droplet-containing flow is rapidly mixed with ambient air, O<sub>3</sub>, and water vapor. The temperature and RH of the gas mixture flow and the temperatures of the droplet-containing flow and the reactor are controlled such that the resulting RH in the reactor is 85% to surround the gas sample with aqueous aerosol particles (abbreviated as AQ mode below) or 100% to surround the gas sample with droplets (abbreviated as CLD mode below). To minimize the influence of the reactor walls and to narrow the particle residence time distribution (RTD), the central 50% (1.5 L min<sup>-1</sup>) of the total flow is subsampled and directed to the aerosol analyzers. The resulting RTD in the APPA is much narrower than those reported for other OFRs, as described by Xu et al. (2024). The narrow RTD results in a correspondingly narrow range of photochemical aging, which aids in data interpretation.

To study gas phase-only chemistry, only the RH and temperature of the gas mixture flow are changed such that the resulting RH in the reactor is 40% (abbreviated as DRY mode below). The contribution of aqueous phase chemistry to the total PM formed is reflected in the difference between what is measured during cloud chemistry experiments and that formed for the same experimental conditions but at low RH. The reactor was alternated between production of PM from gas- and aqueous-phase chemistry.

### 3. Field Campaign Results

#### 3.1 Meteorology and Auxiliary Ambient Gaseous Measurements

Figures 3.1-3.4 provide context for interpretation of our observations given the local meteorology and diurnal profiles of several auxiliary gases. It is important to note that the meteorological parameters and trace gas concentrations were often not co-located with our measurements but within 4-13 miles of the measurement sites (Table 3.1). Therefore, their absolute values are less relevant to the report and degree of correlations between our measurements and the trace gases may not be high, but their evolution during the day can still guide the interpretation of our results.

Table 3.1. Location of monitoring sites with auxiliary data used in analysis.

	<b>Riverside (Mar) and Riverside (Oct)</b>	<b>Wilmington (Mar)</b>	<b>Bakersfield (Apr)</b>
Station name	Riverside-Rubidoux	Long Beach-Signal Hill	Edison
Latitude and longitude	33.99952, -117.41595	33.79371, -118.17102	35.34561, -118.85183
Data used	CO, NO <sub>x</sub> , O <sub>3</sub> , Wind direction and speed	NO <sub>x</sub> , O <sub>3</sub>	NO <sub>x</sub> , O <sub>3</sub>
Auxiliary Station name	March Air Reserve Base (KRIV)	Compton-700 North Bullis Road	Bakersfield-Municipal Airport
Latitude and longitude	33.88194, -117.25902	33.90145, -118.20499	35.33156, -118.99990
Data used	Temperature and humidity	CO	CO
Station name	-	Zamperini Field Airport (KTOA)	Meadows Field Airport (KBFL)
Latitude and longitude	-	33.80338, -118.33961	35.43386, -119.05767
Data used	-	Wind direction and speed, temperature, humidity	Wind direction and speed, temperature, humidity

The wind rose plots indicate that regardless of the season, westerly flows dominated transport during Riverside (Mar) and Riverside (Oct) (Figure 3.1 and 3.2), making the Riverside site ideal for sampling air masses originating from coastal and western parts of the Los Angeles Basin. During Wilmington (Mar), winds at a nearby airport (Zamperini Field airport) were predominantly westerly with some flows from north (Figure 3.3). It is worth noting that it is possible that wind direction at the measurement site was not best represented by the measurements at Zamperini Field airport, given the complex topography of nearby neighborhoods. During Bakersfield (Apr), the meteorology at Meadows Field airport was dominated by easterly flows (Figure 3.4). Assuming a similar behavior at the sampling site, and given its location, this corresponds to air masses travelling over agricultural fields and foothills of the southern Sierra Nevada. However, some air masses from north and west (urban/industrial parts of Bakersfield) were also transported, with typically higher concentrations of NR-PM<sub>1</sub>.

These figures illustrate that despite sampling in different seasons in Riverside during Riverside (Mar) and Riverside (Oct) (Figure 3.1 and 3.2), campaign-average maximum and minimum temperatures were within 5 degrees of each other and relative humidity (RH) was also within 10%. Cooler temperature and higher RH was observed during Wilmington (Mar) (Figure 3.3), while conditions during Bakersfield (Apr) (Figure 3.4) were most similar to those of Riverside (Mar) .

In all locations, a sharp morning rush-hour peak is observed for CO and NO<sub>x</sub> from ~4-7 am, with a secondary peak beginning at ~6 pm. With the exception of observations at Bakersfield, this nightly increase continues and plateaus out by midnight. At Bakersfield, the afternoon peaks in CO and NO<sub>x</sub> subside by 8 pm.

At all sites, O<sub>3</sub> peaks in the early afternoon, consistent with the time of maximum photochemistry.

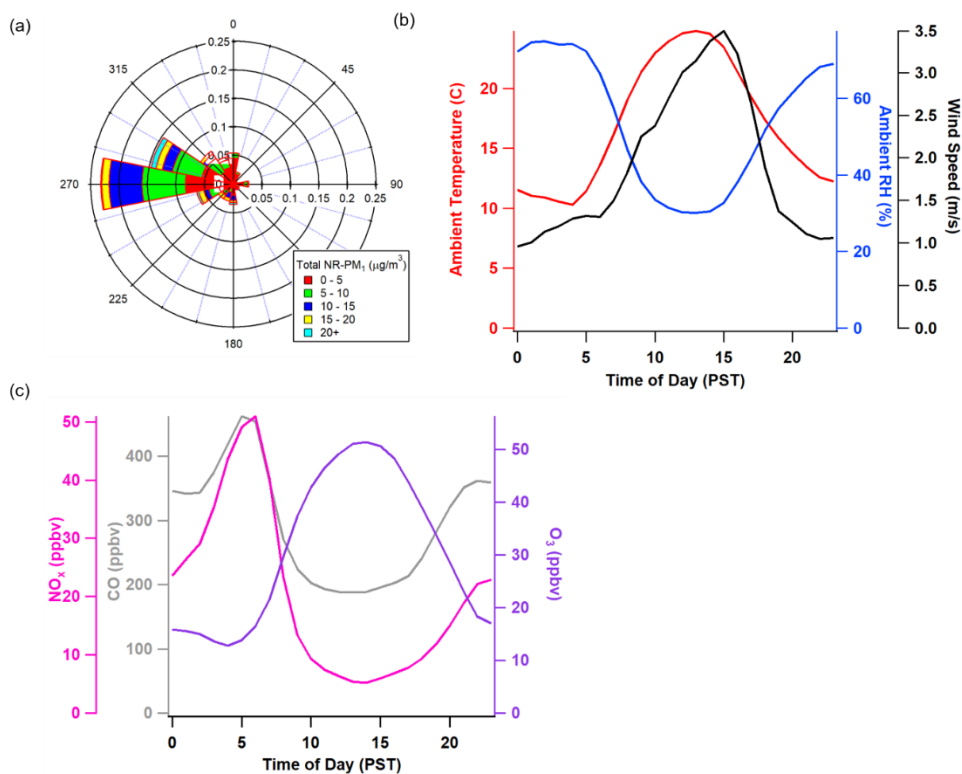


Figure 3.1. Summary of campaign-average meteorological parameters and auxiliary gas phase measurements during Riverside (Mar). (a) Wind rose of total NR-PM<sub>1</sub> concentrations; (b) Diurnal profiles of ambient temperature, relative humidity (RH), and wind speed; (c) Diurnal profiles of NO<sub>x</sub>, CO, and O<sub>3</sub>.

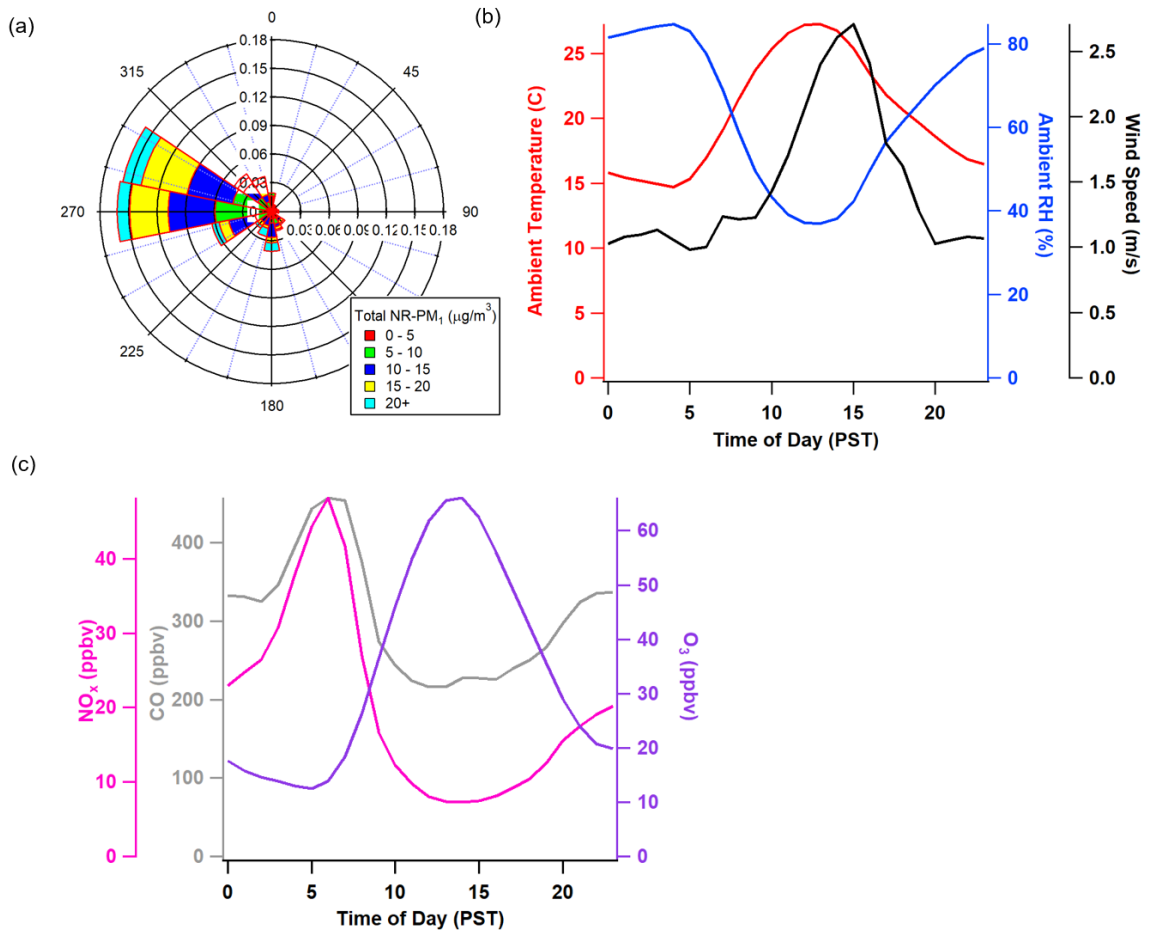


Figure 3.2. Summary of campaign-average meteorological parameters and auxiliary gas phase measurements during Riverside (Oct). (a) Wind rose of total NR-PM<sub>1</sub> concentrations; (b) Diurnal profiles of ambient temperature, relative humidity (RH), and wind speed; (c) Diurnal profiles of NO<sub>x</sub>, CO, and O<sub>3</sub>.

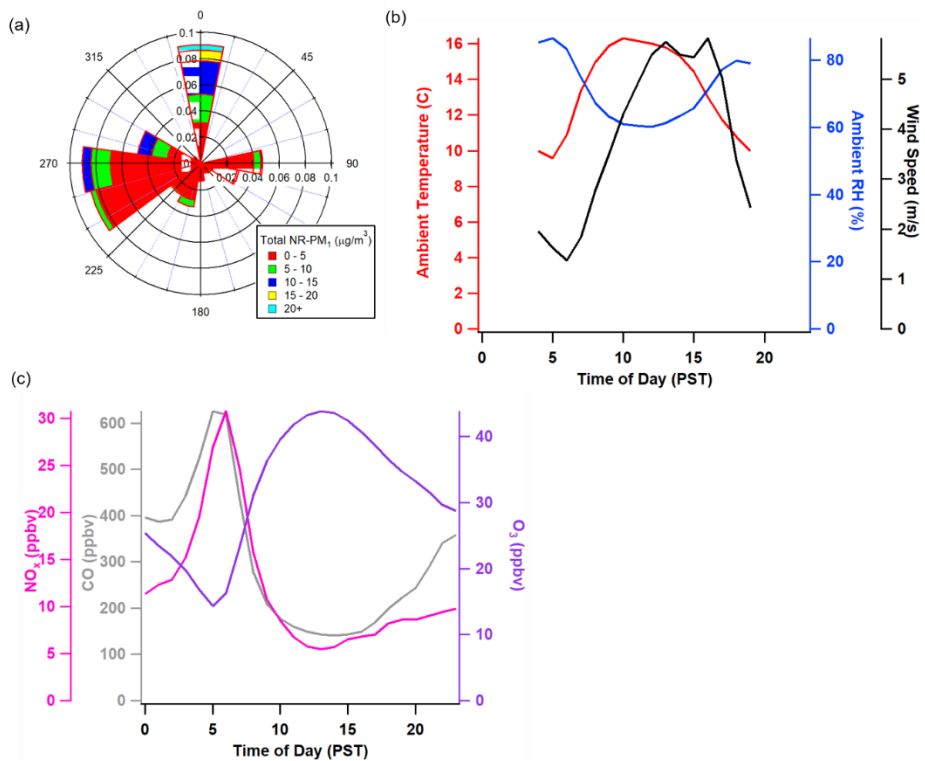


Figure 3.3. Summary of campaign-average meteorological parameters and auxiliary gas phase measurements during Wilmington (Mar). (a) Wind rose of total NR-PM<sub>1</sub> concentrations; (b) Diurnal profiles of ambient temperature, relative humidity (RH), and wind speed; (c) Diurnal profiles of NO<sub>x</sub>, CO, and O<sub>3</sub>.

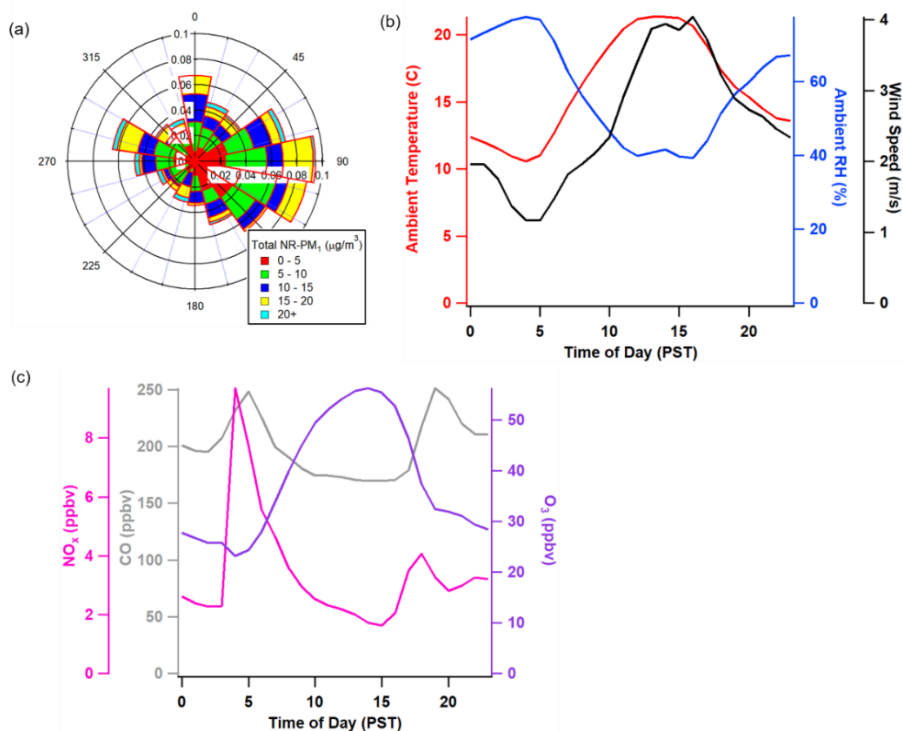


Figure 3.4. Summary of campaign-average meteorological parameters and auxiliary gas phase measurements during Bakersfield (Apr). (a) Wind rose of total NR-PM<sub>1</sub> concentrations; (b) Diurnal profiles of ambient temperature, relative humidity (RH), and wind speed; (c) Diurnal profiles of NO<sub>x</sub>, CO, and O<sub>3</sub>.

### 3.2 Ambient PM<sub>1</sub> composition

Figures 3.5-3.8 summarize the general observations of ambient non-refractory PM<sub>1</sub> composition and eBC. Consistently during all campaigns, OA contributed to 58-67% of NR-PM<sub>1</sub>. The second highest contributor to NR-PM<sub>1</sub> mass was nitrate (14-19%) in Riverside (Mar and Oct) and sulfate in Wilmington (Mar) and Bakersfield (Apr) (17-21%). Surprisingly, the contribution of nitrate to NR-PM<sub>1</sub> was not significant in Bakersfield (Apr) and the average concentration was less than the PM<sub>2.5</sub> total nitrate that was measured during the same period at CSN's Bakersfield site. This may partially be explained by the different size cuts of the two measurements if nitrate mass distribution was extended to the super-micron size range. Another potential explanation is differences in the measurement site location: the Bakersfield CSN site is located ~10 miles west of our sampling location and in the more urbanized area of Bakersfield. As suggested by Figure 3.4, our measurement site which was closer to the foothills and among the agricultural fields was predominantly upwind of the CSN site. NR-PM<sub>1</sub> chloride was insignificant during all campaigns. During Riverside (Oct) and Bakersfield (Apr), when longer measurements of eBC were available, the contribution of eBC was low at ~3%. Despite sampling in different seasons in Riverside, the overall composition was similar during March and October, although the absolute concentrations were higher during Riverside (Oct) (Figures 3.5-3.6).

At all sites, nitrate aerosol concentration peaked during the early morning rush-hour and its concentration decreased with increased ambient temperature, presumably due to the semivolatile nature of ammonium nitrate, as well as deepening of the daytime boundary layer its mixing with the nocturnal residual-layer. OA increased during morning rush-hour and then decreased continuously until the afternoon rush-hour during Riverside (Mar) and Wilmington (Mar). During Riverside (Oct), there are minimal changes in the OA concentration after the morning peak, suggesting significant secondary production that along with a deeper boundary layer mid-day resulted in more or less constant concentrations. During Bakersfield (Apr), the OA concentration increased after sunset by ~30%, which as discussed under Task 4, is consistent with a nighttime source of secondary OA (Figure 3.8b). The concentration of sulfate in all campaigns was mostly constant during the day, consistent with its regional distribution and suggesting again some contribution from secondary production that counteracts the daytime dilution due to boundary layer deepening. During Riverside (Oct) and Bakersfield (Apr), eBC concentrations peaked during early morning hours (Figure 3.6 and Figure 3.8), consistent with vehicular traffic emissions that also resulted in enhanced CO and NO<sub>x</sub> levels (Figure 3.2 and Figure 3.4). However, during Bakersfield (Apr) a secondary peak was also observed in mid-morning, which could indicate influence from a more local emission source (Figure 3.8b).

As indicated above, a comparison between the nitrate fragmentation pattern when sampling ambient air and those during regular ammonium nitrate calibrations can be used to estimate the contribution of organonitrate/nitroorganics to the nitrate signal. Following these procedures, 60-80% of the observed nitrate in Riverside is attributed to organic molecules ( $f_{\text{NO}_3,\text{org}}$ ) (Figures 3.5-3.6). Furthermore, elevated nitrate (and ammonium) signal corresponded to lower values of  $f_{\text{NO}_3,\text{org}}$ , consistent with morning production of inorganic nitrate (i.e., ammonium nitrate) during the cooler times of the day. During Wilmington (Mar) and Bakersfield (Apr) (Figures 3.7-3.8), the calculated  $f_{\text{NO}_3,\text{org}}$  is noisier because of the overall much lower concentration of nitrate during the campaigns; hence there is no obvious trend in  $f_{\text{NO}_3,\text{org}}$ .

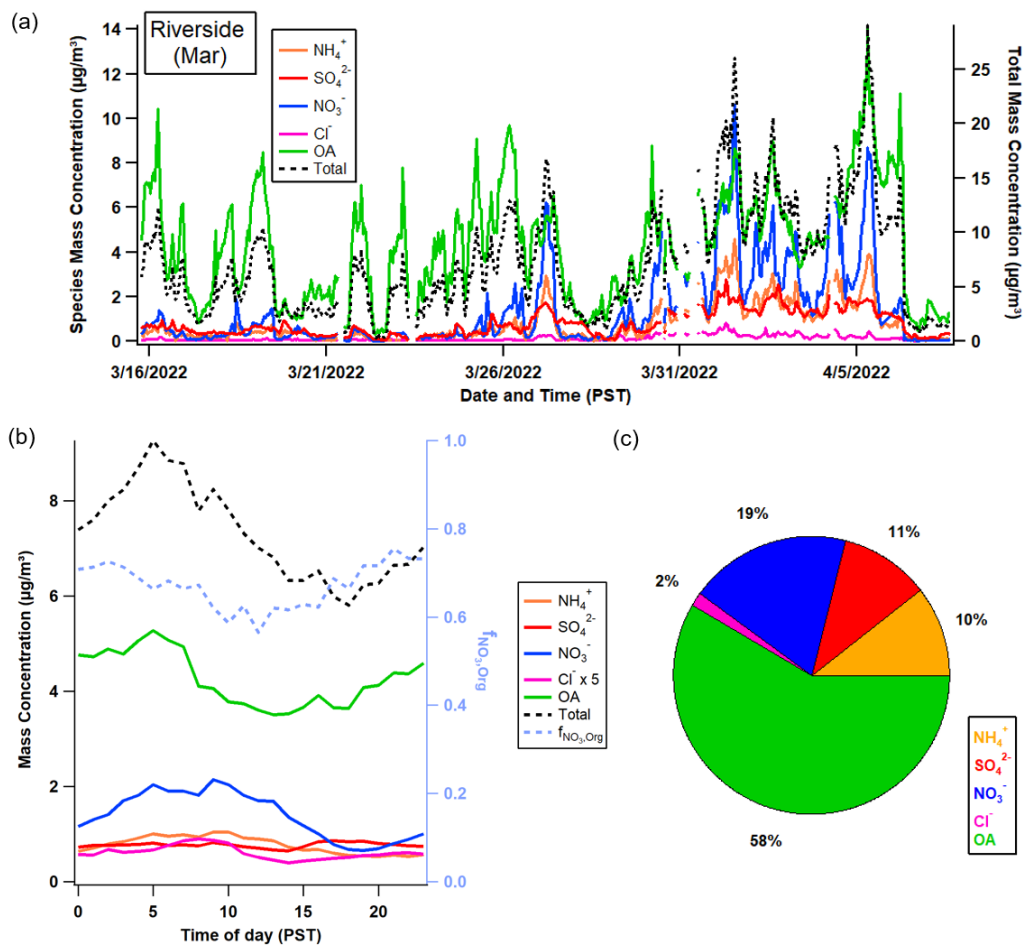


Figure 3.5. Summary of NR-PM<sub>1</sub> observations during Riverside (Mar). (a) Time series of NR-PM<sub>1</sub> components (note that the Total mass concentration trace is added to the right axis); (b) Diurnal profiles of the NR-PM<sub>1</sub> mass concentrations; (c) Average distribution of NR-PM<sub>1</sub> components.

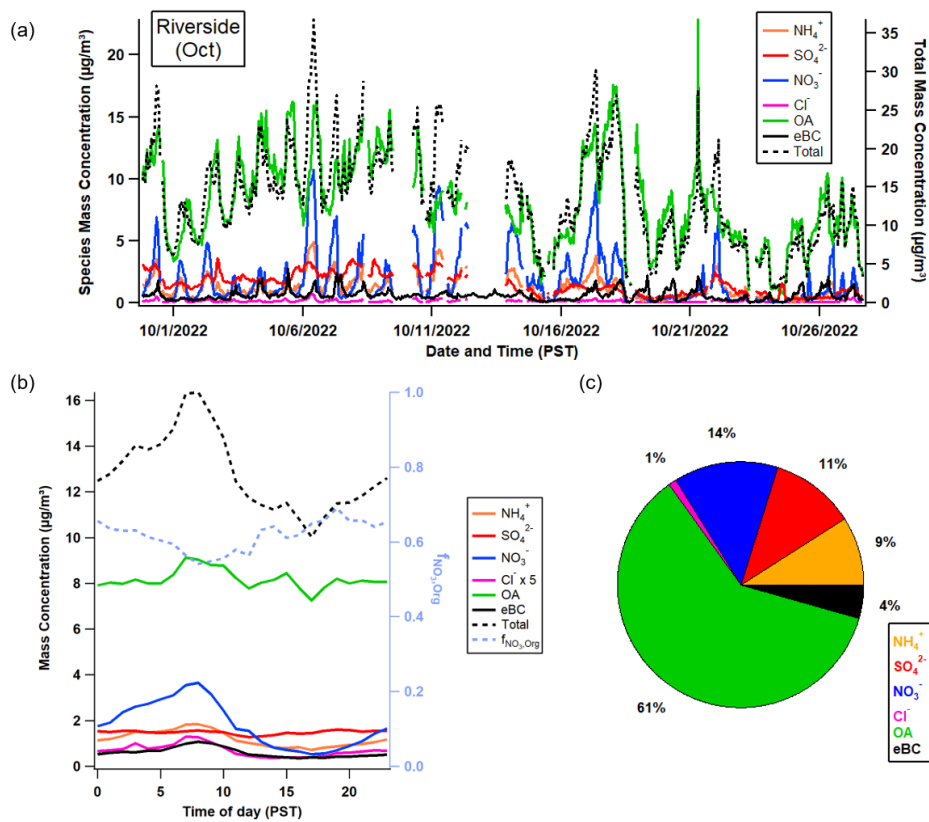


Figure 3.6. Summary of PM<sub>1</sub> and eBC observations during Riverside (Oct). (a) Time series of NR-PM<sub>1</sub> components and eBC (note that the Total mass concentration trace is added to the right axis); (b) Diurnal profiles of the NR-PM<sub>1</sub> and eBC mass concentrations; (c) Average distribution of NR-PM<sub>1</sub> components and eBC.

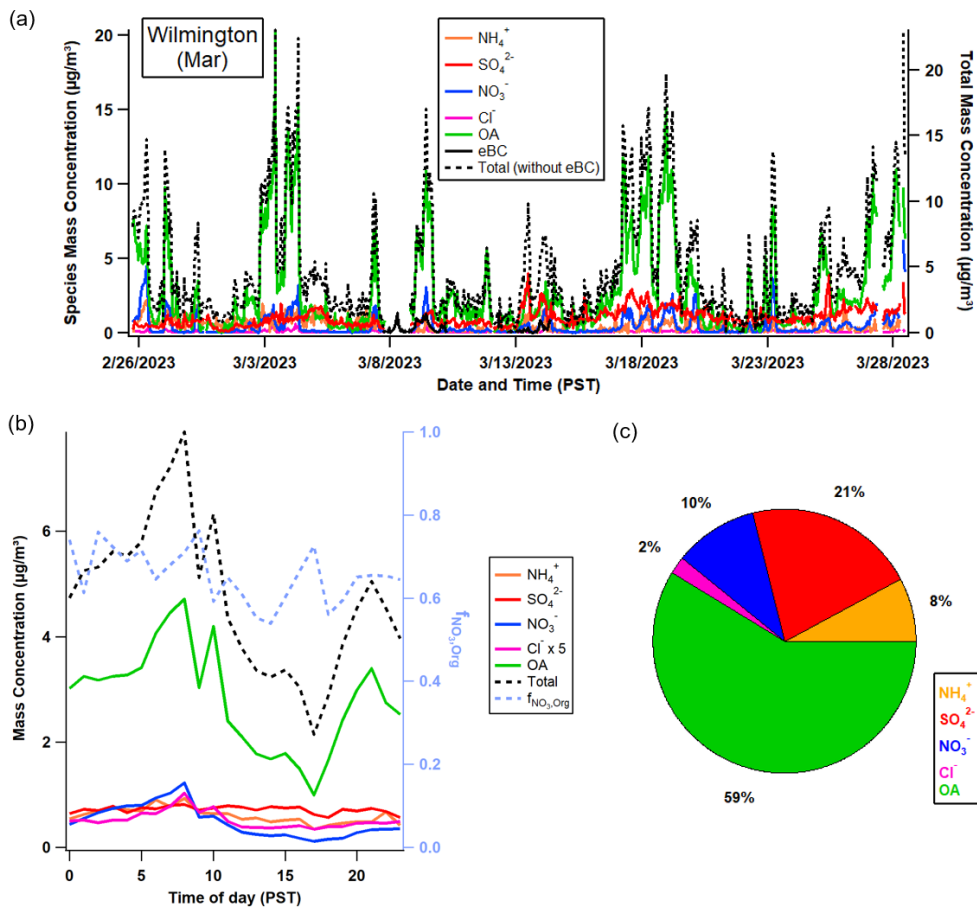


Figure 3.7. Summary of  $\text{PM}_{10}$  and eBC observations during Wilmington (Mar). (a) Time series of NR- $\text{PM}_{10}$  components and eBC (note that the Total mass concentration trace is added to the right axis); (b) Diurnal profiles of the NR- $\text{PM}_{10}$  mass concentrations; (c) Average distribution of NR- $\text{PM}_{10}$  components. Note that due to limited eBC data, its diurnal profile and overall average contribution are not calculated.

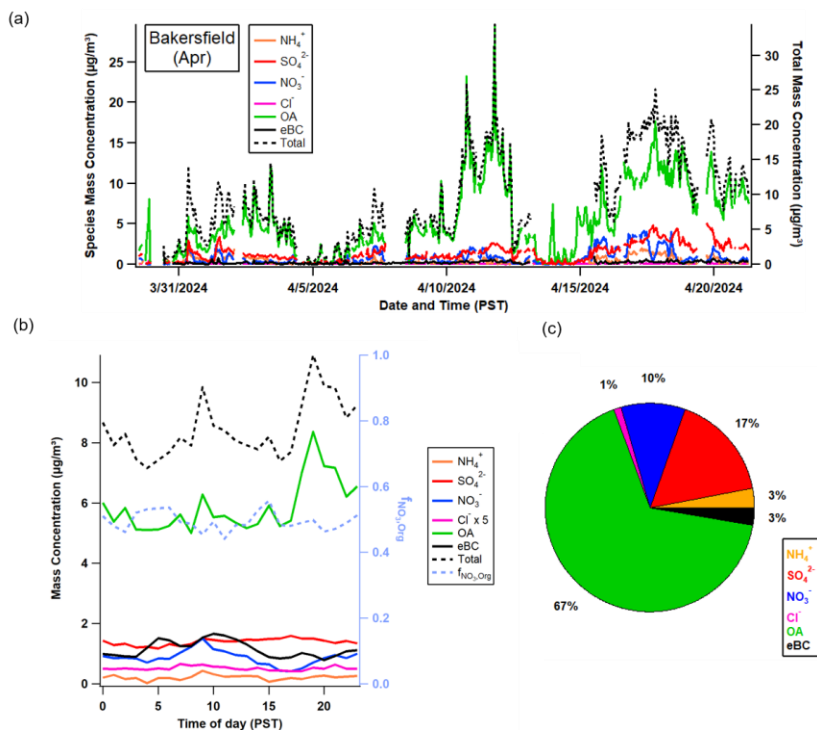


Figure 3.8. Summary of PM<sub>1</sub> observations during Bakersfield (Apr). (a) Time series of NR-PM<sub>1</sub> components (note that the Total mass concentration trace is added to the right axis); (b) Diurnal profiles of the NR-PM<sub>1</sub> mass concentrations; (c) Average distribution of NR-PM<sub>1</sub> components.

### 3.3 Chamber Perturbation Experiments

As described above, perturbation experiments were conducted at the three field sites using the dual CAGE chamber system. During these experiments, controlled injections of NO<sub>2</sub>, VOCs, or NH<sub>3</sub> were continuously introduced into the ambient air flow pulled through one of the two chambers. Each precursor was added at a controlled rate using a mass flow controller to increase its mixing ratio by a prescribed and constant amount. The details of the perturbation experiments and the observed enhancements are provided in Table 3.2.

Prior to initiating a new type of perturbation, both chambers were operated under identical conditions for several hours, with ambient particle-free air circulated through their membrane-wrapped center channels, to minimize contamination and confirm chamber similarity. Perturbation experiments began at the start times specified in Table 3.2. Most continued for 10 - 24 hours with continuous chamber operation. When the same perturbation type was conducted over multiple consecutive days, particularly in Bakersfield, where NO<sub>2</sub> or NH<sub>3</sub> was injected continuously, the experiments were continued without repeating similarity tests.

Table 3.2. Summary of perturbation experiments and observed chamber enhancements.

#	Date	Start time	Duration	Type	Mixing ratio delta	Observed change	Location
1	4/3/22	11:00 pm (on 4/2)	18 h	Isoprene+ $\alpha$ -pinene	$\Delta$ 5 ppb	OA: +0.35 $\mu\text{g m}^{-3}$	Riverside
2	4/5/22	11:00 pm (on 4/4)	15 h	$\alpha$ -pinene	$\Delta$ 5 ppb	OA: +0.6 $\mu\text{g m}^{-3}$	Riverside
3	4/6/22	11:30 am	10 h	Toluene	$\Delta$ 5 ppb	OA: +0.4 $\mu\text{g m}^{-3}$	Riverside
4	10/25/22	9:00 am	22 h	NO <sub>2</sub>	$\Delta$ 5 ppb	None	Riverside
5	10/27/22	11:00 am	10 h	NH <sub>3</sub>	$\Delta$ 10 ppb	Nitrate: +0.35 $\mu\text{g m}^{-3}$ , then OA: +0.7 $\mu\text{g m}^{-3}$	Riverside
6	3/20/23	10:00 am	24 h	NO <sub>2</sub>	$\Delta$ 10 ppb	None	Wilmington
7	3/24/23	10:00 am	20 h	NO <sub>2</sub>	$\Delta$ 10 ppb	None	Wilmington
8	3/28/23	7:30 am	8 h	NH <sub>3</sub>	$\Delta$ 10 ppb	Nitrate: +0.68 $\mu\text{g m}^{-3}$	Wilmington
9	4/3/24	10:00 am	10 h	NO <sub>2</sub>	$\Delta$ 10 ppb	None	Bakersfield
10	4/4/24	10:00 am	9 h	NO <sub>2</sub>	$\Delta$ 10 ppb	None	Bakersfield
11	4/5/24	10:00 am	10 h	NO <sub>2</sub>	$\Delta$ 20 ppb	None	Bakersfield
12	4/6/24	6:00 pm	6 h	NO <sub>2</sub>	$\Delta$ 20 ppb	None	Bakersfield
13	4/7/24	10:00 am	8 h	NO <sub>2</sub>	$\Delta$ 20 ppb	None	Bakersfield
14	4/8/24	3:00 pm	9 h	NO <sub>2</sub>	$\Delta$ 20 ppb	None	Bakersfield
15	4/9/24	9:00 am	22 h	NH <sub>3</sub>	$\Delta$ 10 ppb	None	Bakersfield
16	4/11/24	9:00 am	22 h	NH <sub>3</sub>	$\Delta$ 10 ppb	None	Bakersfield
17	4/13/24	9:00 am	22 h	NO <sub>2</sub>	$\Delta$ 20 ppb	None	Bakersfield
18	4/14/24	9:00 am	22 h	NO <sub>2</sub>	$\Delta$ 20 ppb	None	Bakersfield
19	4/15/24	9:00 am	22 h	NO <sub>2</sub>	$\Delta$ 20 ppb	Nitrate: +0.8 $\mu\text{g m}^{-3}$	Bakersfield
20	4/16/24	9:00 am	22 h	NO <sub>2</sub>	$\Delta$ 20 ppb	None	Bakersfield
21	4/17/24	9:00 am	22 h	NH <sub>3</sub>	$\Delta$ 20 ppb	None	Bakersfield
22	4/18/24	9:00 am	22 h	NH <sub>3</sub>	$\Delta$ 20 ppb	Nitrate: +0.1 $\mu\text{g m}^{-3}$	Bakersfield
23	4/19/24	9:00 am	22 h	NH <sub>3</sub>	$\Delta$ 20 ppb	None	Bakersfield
24	4/20/24	9:00 am	22 h	NH <sub>3</sub>	$\Delta$ 20 ppb	Nitrate: +0.18 $\mu\text{g m}^{-3}$	Bakersfield

### 3.3.1 VOC Addition Experiments

VOC perturbation experiments were conducted only during the Riverside (Mar) campaign. These experiments included biogenic volatile organic compounds (BVOCs; isoprene and  $\alpha$ -pinene) and an anthropogenic volatile organic compound (AVOC; toluene). For the perturbation experiment in which the BVOC mixture was added, formation of SOA resulted in an observed growth in 50 nm seed particles in the perturbation chamber and an increase in organic aerosol concentration measured by the mAMS of  $0.35 \mu\text{g m}^{-3}$  relative to the control chamber (Figure 3.9). Based on the SMPS volume size distribution, the enhancement in organic content was primarily attributed to oxidation product condensation on larger seed particles and not new particle formation. Notably, less SOA was produced during daytime than at night during these experiments. The effect of alpha-pinene addition without isoprene was evaluated under similar conditions during an experiment on April 5, 2022. The resulting growth rate of the seed particles and SOA mass formed both exceeded those measured for the biogenic mixture experiment, with a  $0.6 \mu\text{g m}^{-3}$  enhancement relative to the control chamber (Figure 3.10). These findings align with previous research that reported negligible SOA formation from isoprene and that isoprene addition to alpha-pinene may inhibit SOA formation (Voliotis et al., 2022). Analysis of organic fractions revealed lower  $f_{44}$  ( $m/z=44$ ) and higher  $f_{43}$  ( $m/z=43$ ) values in both experiments (Figure 3.11). The  $f_{44}$  signal represents highly oxidized  $\text{CO}_2^+$  fragments from decarboxylation, while  $f_{43}$  corresponds to less oxidized  $\text{C}_2\text{H}_3\text{O}^+$  fragments. The observed lower oxygenation products are consistent with  $\alpha$ -pinene's tendency to form less oxidized products (Voliotis et al., 2022).

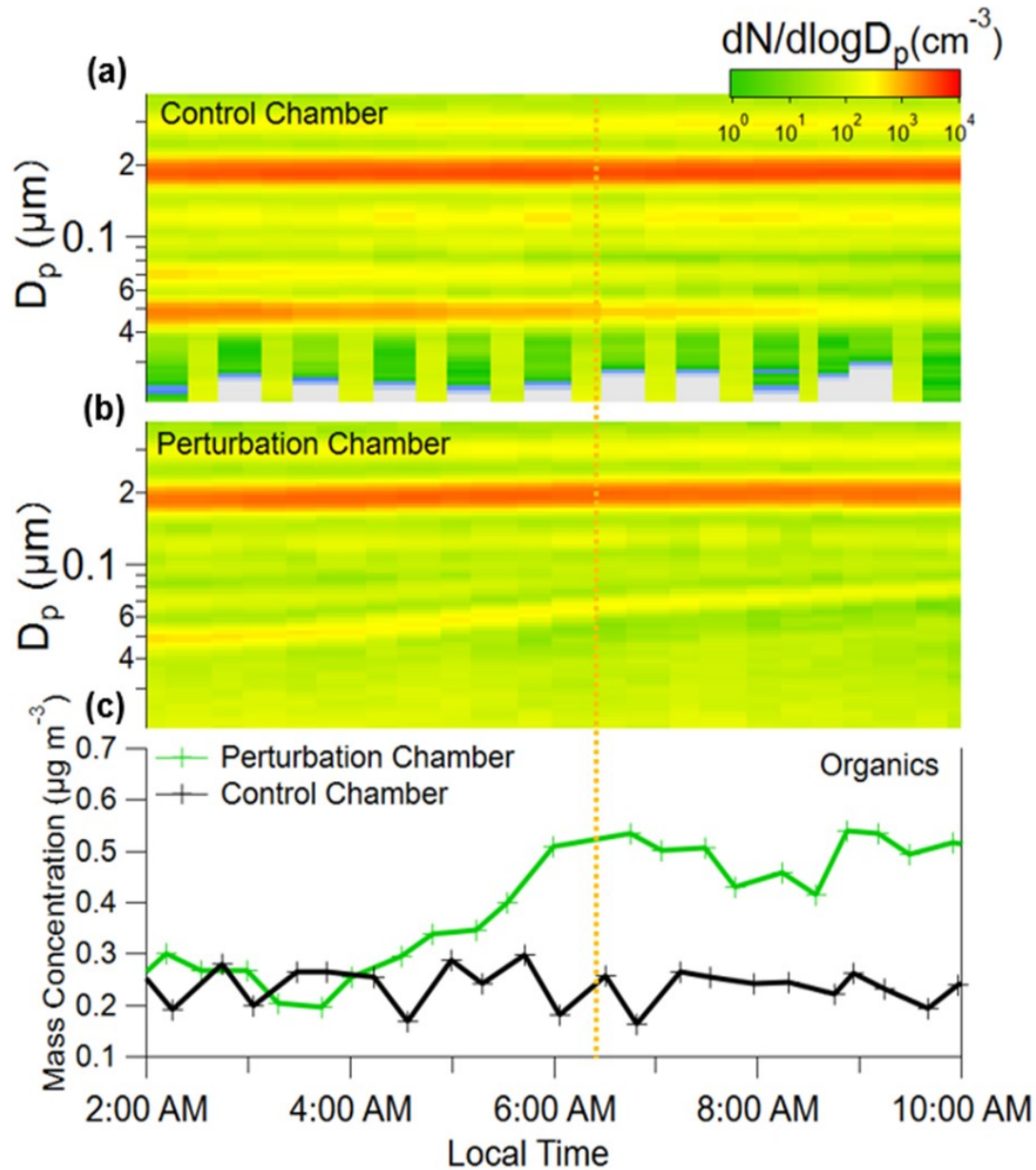


Figure 3.9. Time series of particle size distributions in the control chamber (a) and perturbation chamber (b) and mass concentration of organic aerosol in both chambers (c) during the perturbation experiment on April 3, 2022 in Riverside in which  $\alpha$ -pinene and isoprene were added to the ambient air pulled through

one of the two chambers. The orange dotted line indicates the time of sunrise. The perturbation began at 11 pm on April 2, 2022 and continued for approximately 18 h.

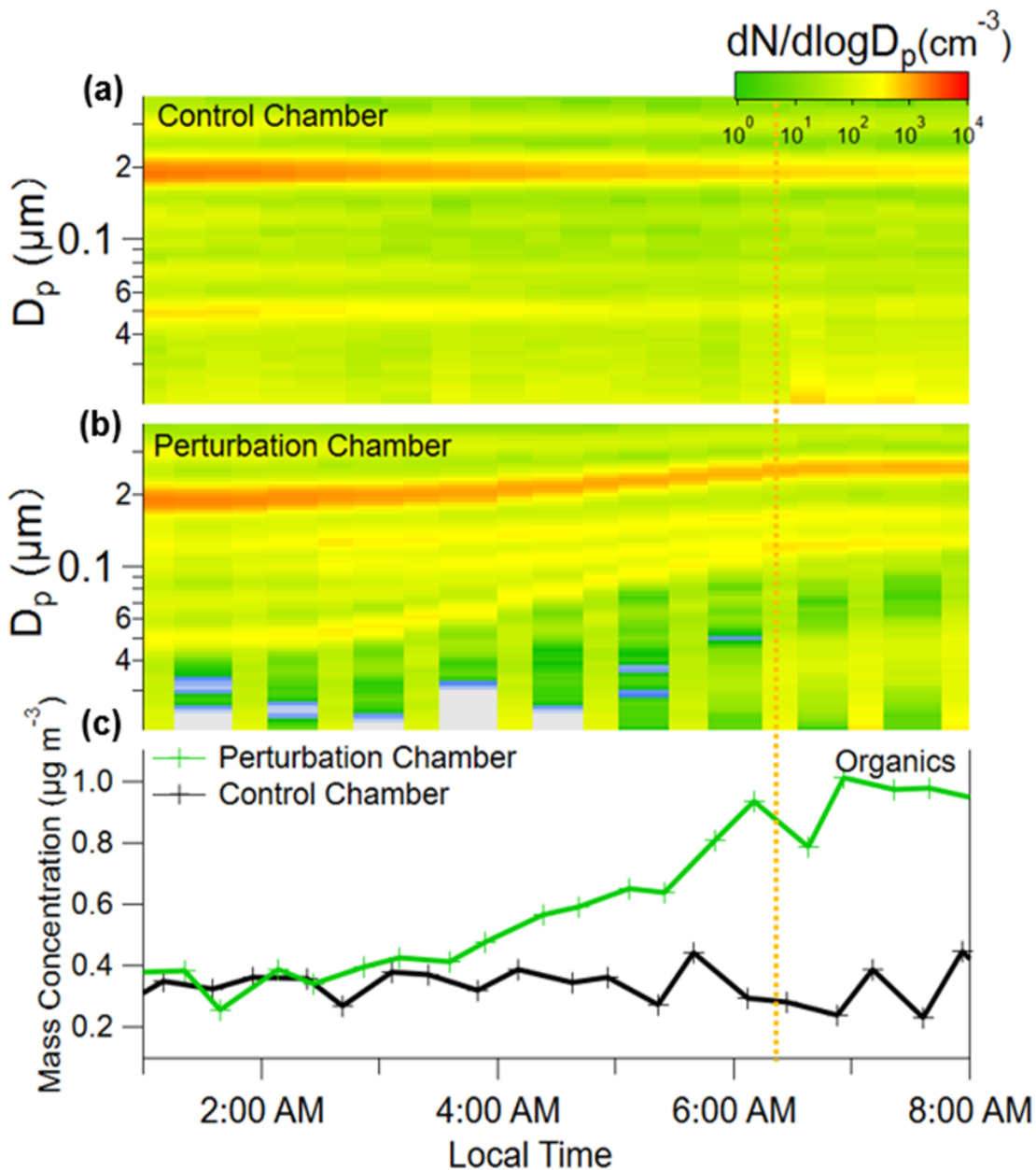


Figure 3.10. Time series of particle size distributions in the control chamber (a) and perturbation chamber (b) and mass concentration of organic aerosol in both chambers (c) during the perturbation experiment on April 5, 2022 in Riverside in which alpha-pinene was added to the ambient air pulled through one of the two chambers. The orange dotted line indicates the time of sunrise. The perturbation began at 11:00 pm on April 4, 2022, and continued for 15 h.

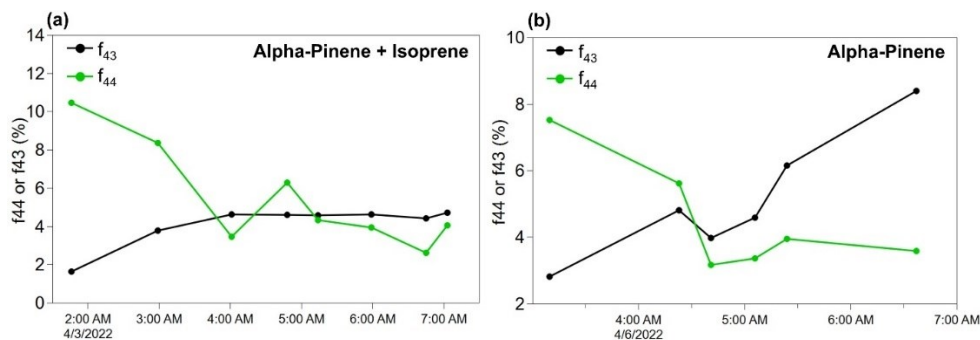


Figure 3.11. Times series of the signal fraction of  $m/z=44$  and  $m/z=43$  in the total organic signal measured by mAMS in the alpha-pinene + isoprene experiment (a) and alpha-pinene-only experiment (b).

Toluene was used as a surrogate for anthropogenic VOCs. Similar to the experiments that examined the impact of adding BVOC(s), 5 ppb was added to the perturbation chamber in an experiment conducted in Riverside on April 6, 2022, with the results shown in Figure 3.12. New particle formation and the growth of small seed particles were observed in the perturbation chamber, though minimal change in the size of the larger particles present in the chamber was observed. The mass concentration of organic aerosol was enhanced by  $0.4 \mu\text{g m}^{-3}$  in the perturbation chamber, while that of other aerosol chemical components was unchanged. No SOA formation enhancement was observed during the nighttime portion of the experiment, which contrasts with what was observed for the BVOCs and is explained by the minimal reactivity of toluene with  $\text{NO}_3$  radicals and  $\text{O}_3$  that are the dominant nighttime oxidants.

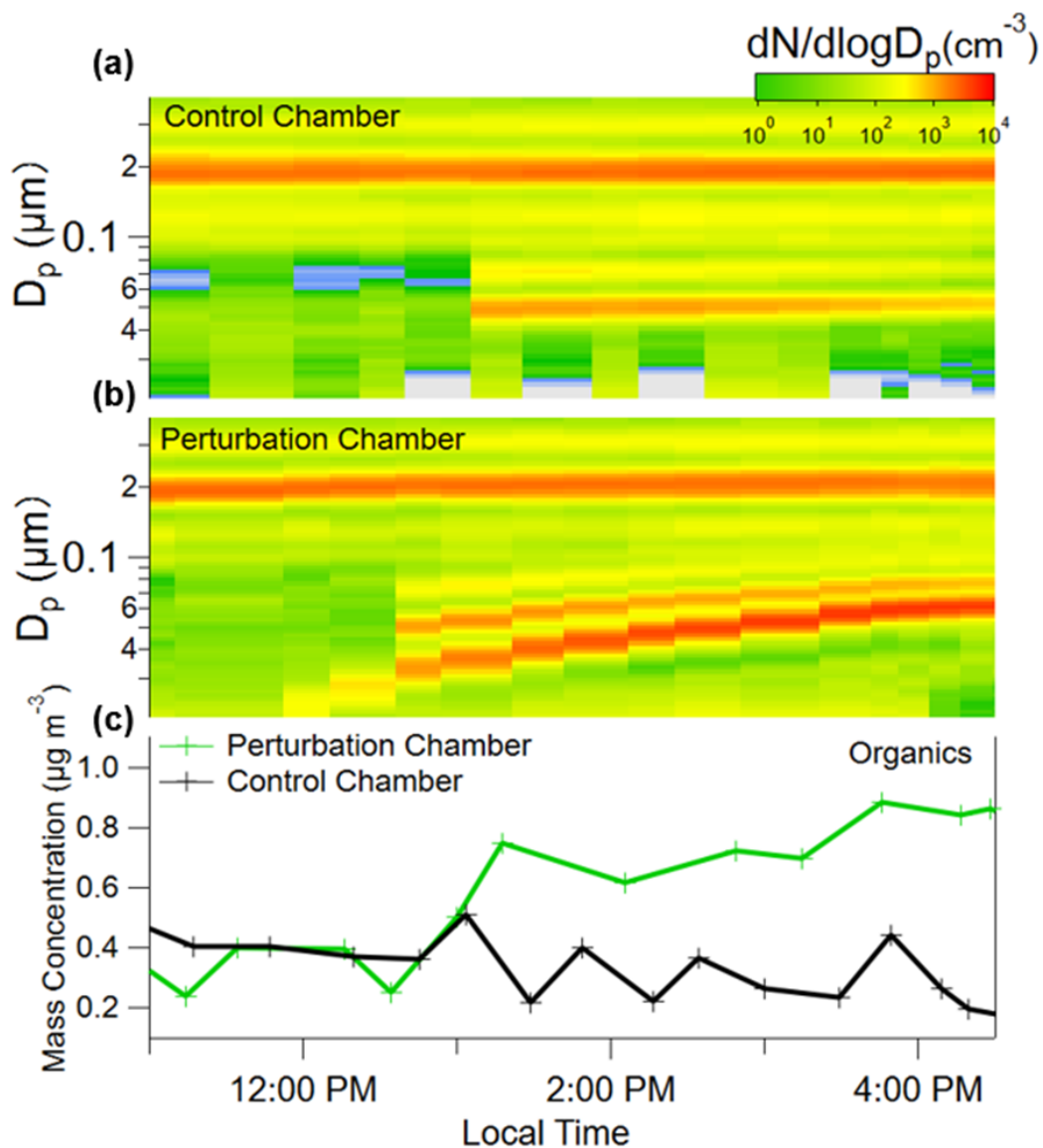


Figure 3.12. Time series of particle size distributions in the control chamber (a) and perturbation chamber (b) and mass concentration of organic aerosol in both chambers (c) during the perturbation experiment on April 6, 2022 in Riverside in which toluene was added to the ambient air pulled through one of the two chambers. The perturbation began at 11:30 am and continued for 10 h.

### 3.3.2 NO<sub>x</sub> Addition Experiments

NO<sub>2</sub> perturbation experiments were conducted at all three field sites. During the Riverside (Oct) campaign, no significant growth of seed particles or formation of new particles was observed with addition of 5 ppb to the perturbation chamber (Figure 3.13). AMS measurements revealed no enhancement in nitrate concentration or other species. While addition of NO<sub>2</sub> is expected to result in increased production of nitric acid, formation of particulate nitrate can be limited by the concentration of

ammonia or another gas-phase base. Aerosol formation potential may also depend on the concentration and speciation of VOCs because of their influence on the  $\text{NO}_2$  oxidation process through impacts on production of OH and  $\text{O}_3$ . In regions with limited ammonia, an increase in  $\text{NO}_2$  does not necessarily lead to enhanced secondary aerosol formation. Additionally, higher NO concentration can sometimes reduce SOA yield as products of reactions of  $\text{RO}_2$  radicals with NO are often more volatile than those from reaction with  $\text{HO}_2$  or  $\text{RO}_2$  radicals (Ng et al., 2007; Sarrafzadeh et al., 2016).

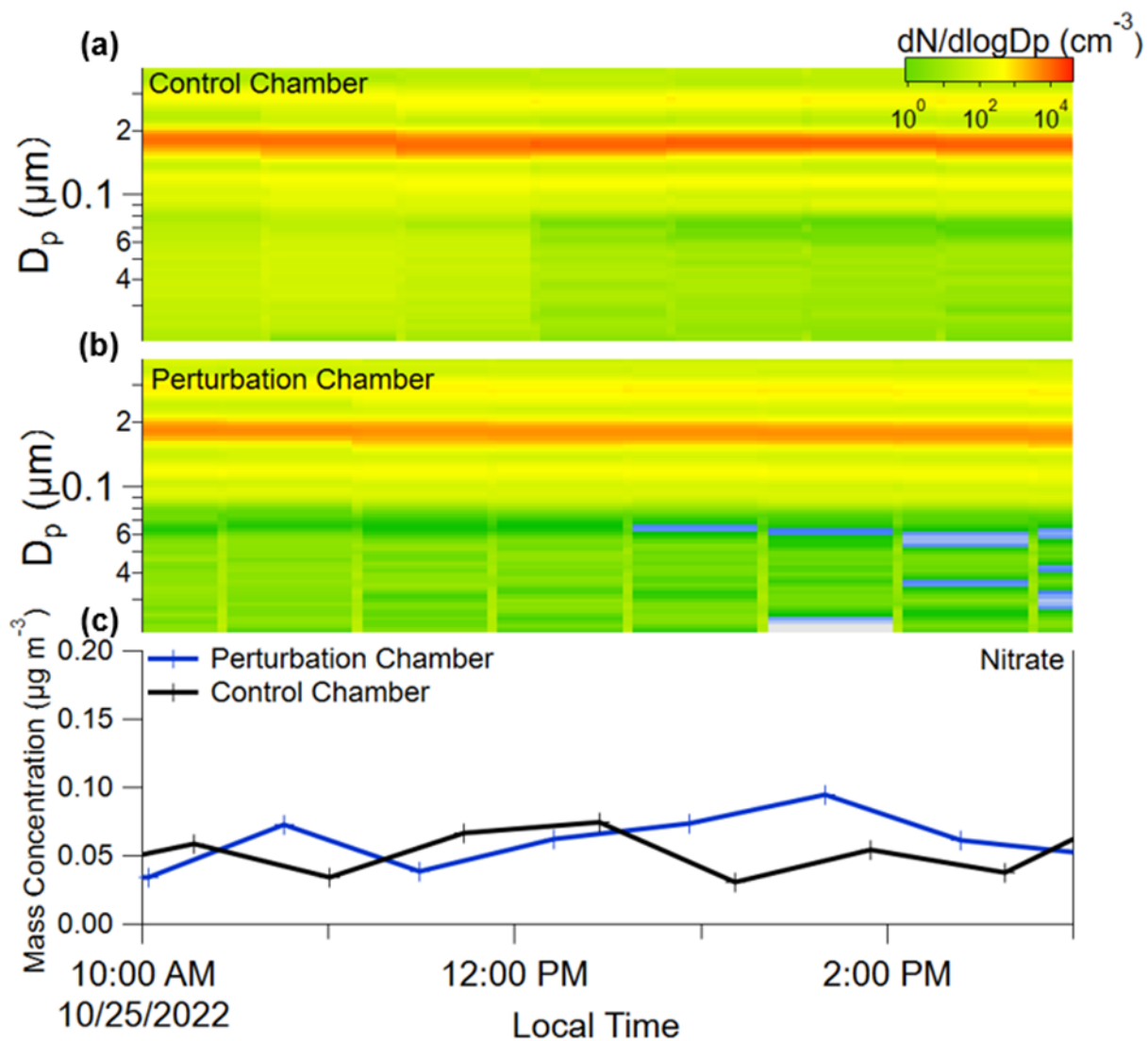


Figure 3.13. Time series of particle size distributions in the control chamber (a) and perturbation chamber (b) and nitrate mass concentration for both chambers (c) during the perturbation experiment on October 25, 2022 in Riverside in which  $\text{NO}_2$  was added to the ambient air pulled through one of the two chambers. The perturbation began at 9:00 am and continued for 22 h.

NO<sub>2</sub> perturbation experiments in Wilmington yielded similar results over two experimental days (Figure 3.14). Despite NO<sub>2</sub> injection initiation at 10:00 am on both days, nitrate aerosol concentrations in the perturbation chamber remained comparable to that in the control chamber. These results suggest that Wilmington, like Riverside, is ammonia-limited, and that elevated NO<sub>2</sub> alone does not lead to enhanced secondary aerosol formation.

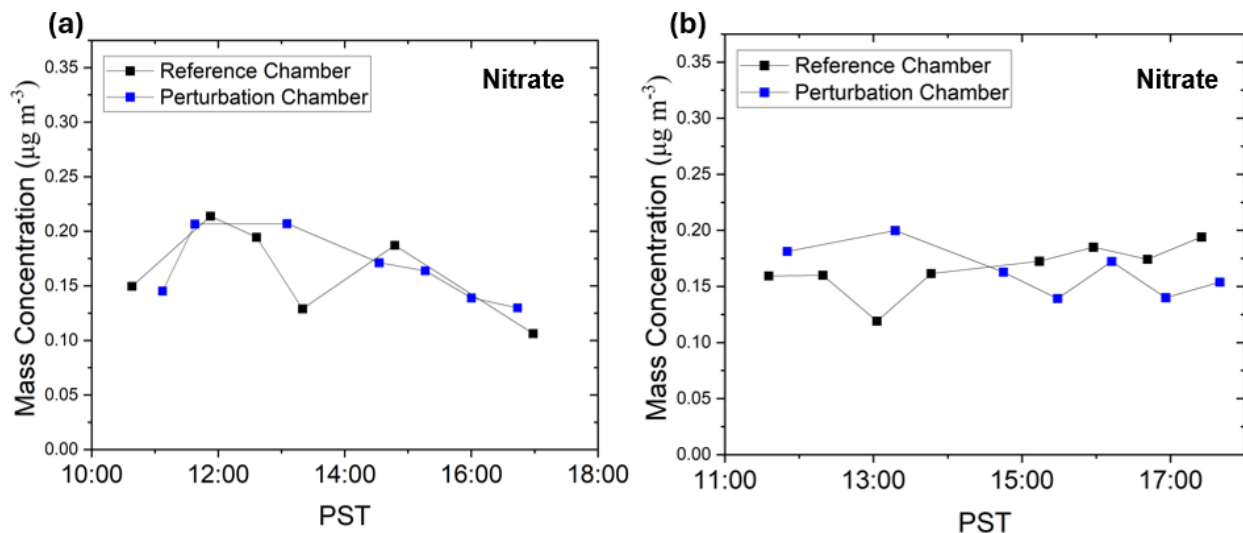


Figure 3.14. Aerosol mass concentrations of nitrate in both chambers during NO<sub>2</sub> perturbation experiments in Wilmington on (a) March 20, 2023 and (b) March 24, 2023. Both perturbations began at 10:00 am and continued for approximately 24 h.

Ten days of NO<sub>2</sub> perturbation experiments were conducted in Bakersfield. Most experiments were carried out continuously throughout the day, except for those with specific time ranges noted in Table 3.2. Nitrate aerosol concentration in the perturbation chamber exceeded that in the control on just one of the experiment days, with the concentration in the perturbation chamber 0.8  $\mu\text{g m}^{-3}$  above that in the control during the late afternoon and until midnight (Figure 3.15). The limited frequency of detectable enhancements (1 out of 10 days) suggests temporal variability in ammonia availability or potential nitrate volatilization before measurement.

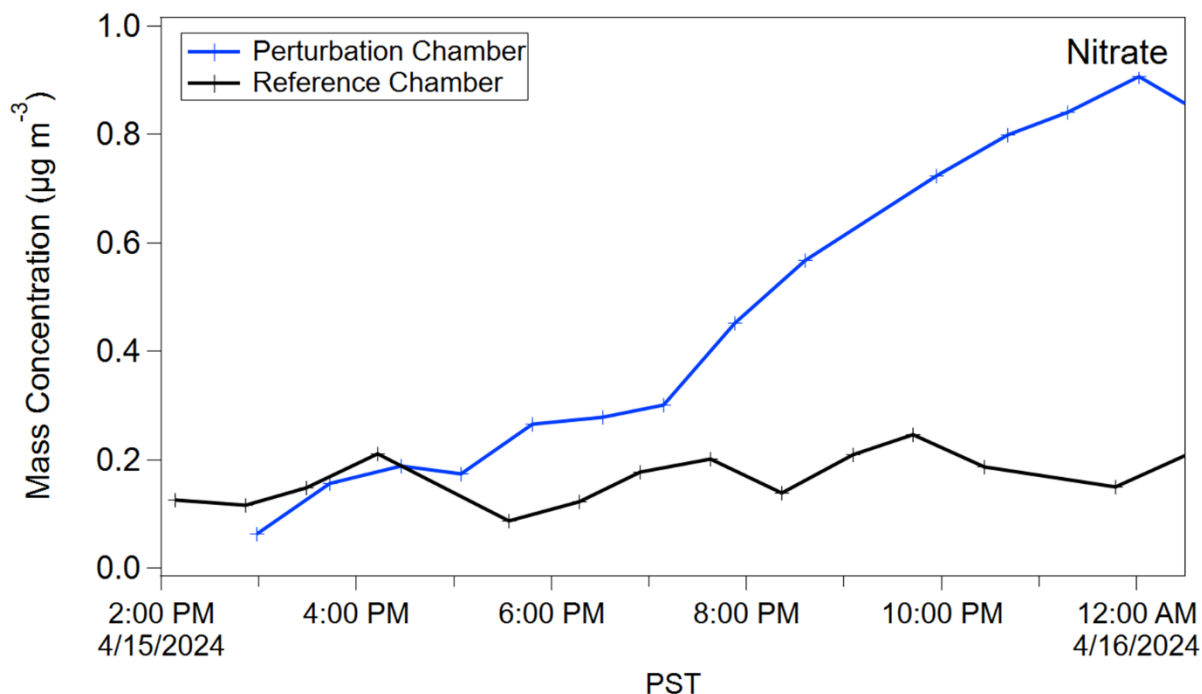


Figure 3.15. Mass concentrations of nitrate aerosol in both chambers during NO<sub>2</sub> perturbation experiments in Bakersfield on April 15, 2024. The perturbations were applied continuously from April 15 to April 16, 2024.

### 3.3.3 NH<sub>3</sub> Addition Experiments

NH<sub>3</sub> perturbation experiments were also conducted at all three sites. In Riverside, NH<sub>3</sub> perturbations resulted in the growth of seed particles and new particle formation, indicating enhanced aerosol production (Figure 3.16). This is consistent with findings from studies in the Los Angeles area, which is identified as an NH<sub>3</sub>-sensitive regime (Dang et al., 2024). In the early stage of the experiments, nitrate concentration increased, suggesting contribution of ammonium nitrate to particle growth. After approximately two hours, nitrate aerosol levels stabilized while organic aerosol concentration rose, coinciding with new particle formation. These findings align with previous research showing delayed organic acid reaction with NH<sub>3</sub> even under background NO<sub>x</sub> concentration, attributed to initial nitric acid formation from NO<sub>x</sub> photooxidation (Hao et al., 2020).

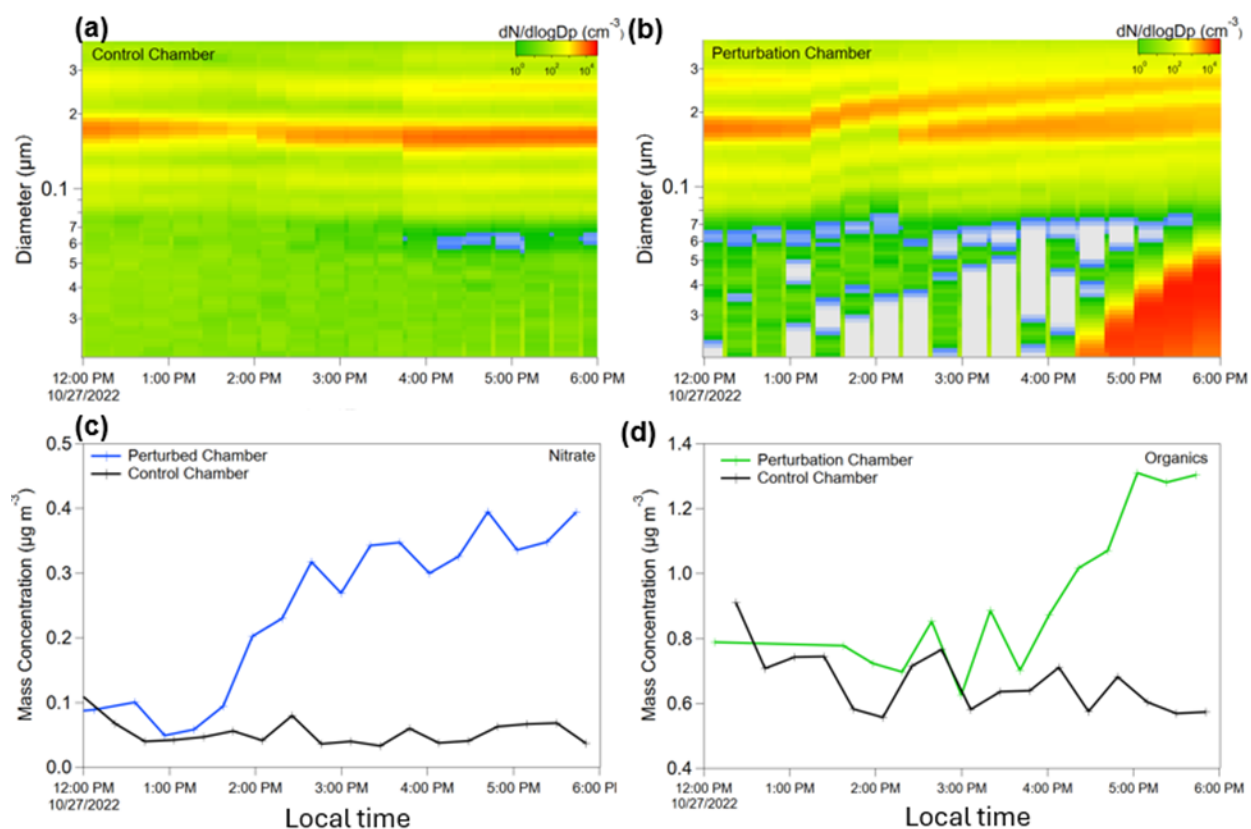


Figure 3.16. Time series of particle size distributions in the control chamber (a) and perturbation chamber (b) and mass concentration of organic aerosol in both chambers (c) during the perturbation experiment on October 27, 2022 in Riverside in which ammonia was added to the ambient air pulled through one of the two chambers. The perturbation began at 11:00 am and continued for 10 h.

We observed that the rise in organic aerosol concentration coincided with an increase in  $f_{44}$  (Figure 3.17). As previously noted,  $f_{44}$  indicates highly oxidized  $\text{CO}_2^+$  fragments resulting from decarboxylation.  $\text{CO}_2^+$  is not only a reliable marker for oxygenated organic aerosol but also closely linked with the formation of organic mono- and di-acids, as demonstrated in both laboratory and field measurements. The concurrent increases in organic substances and  $\text{CO}_2^+$  fragments suggest reaction between organic acids and ammonia.

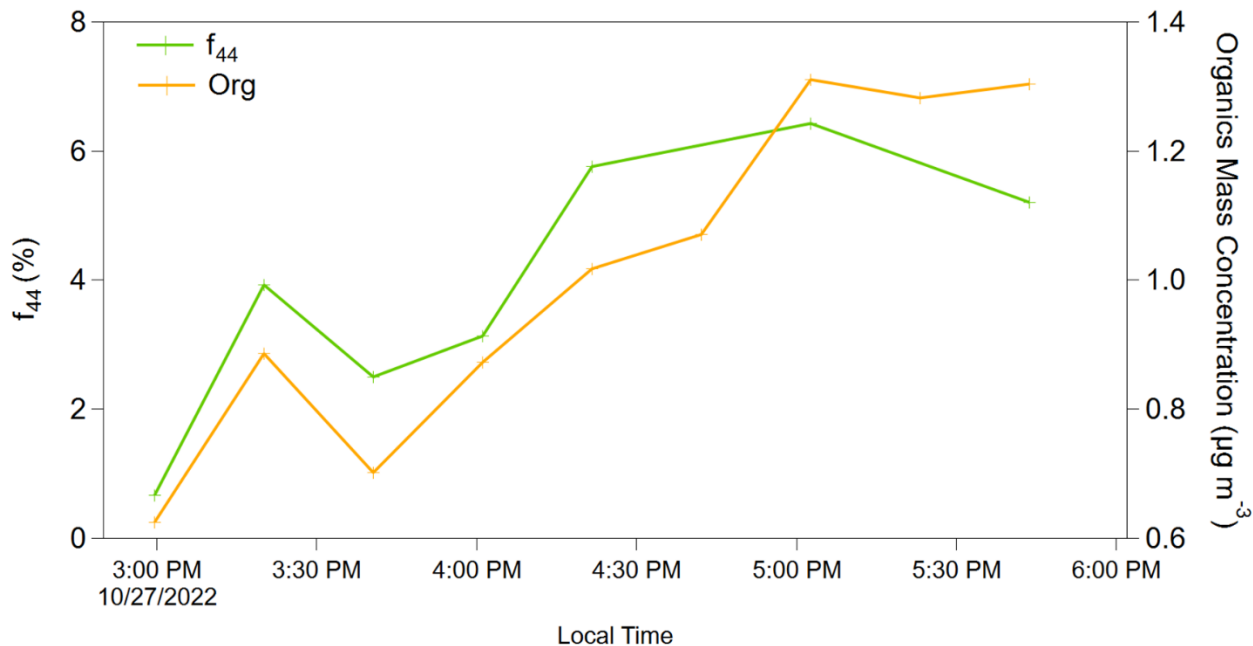


Figure 3.17. Time series of signal fraction of  $m/z=44$  and mass concentration of organics in the perturbation chamber.

Ammonia perturbation experiments in Wilmington were limited due to chamber contamination and troubleshooting. On March 28, 2023, the sole successful  $\text{NH}_3$  perturbation experiment resulted in nitrate aerosol concentration enhancement of  $0.68 \mu\text{g m}^{-3}$  (Figure 3.18). In Bakersfield, six days of  $\text{NH}_3$  perturbation experiments were conducted, with modest nitrate aerosol enhancement observed during two nighttime periods (April 18 and April 20, 2024; Figure 3.19). On those nights, nitrate aerosol concentrations in the perturbation chamber increased by  $0.10 \mu\text{g m}^{-3}$  on April 18 and  $0.18 \mu\text{g m}^{-3}$  on April 20 relative to the control chamber, while organic concentrations showed no measurable differences. The enhancement of nitrate without a corresponding increase in organic aerosol suggests that for the environmental conditions at the time,  $\text{NH}_3$  perturbations primarily enhanced inorganic aerosol formation rather than organic aerosol, which is different from what was observed in Riverside. Additionally, the magnitude of nitrate enhancement was lower than observed in previous campaigns despite larger  $\text{NH}_3$  perturbations. Ammonium nitrate aerosol formation is largely insensitive to ammonia in emissions-rich agricultural regions such as the Central Valley. That nitrate PM concentration increased in the perturbation chamber suggests air reaching the site was only modestly impacted by agricultural emissions. For the prevailing easterly winds shown in Figure 3.4, this may be explained by the limited fetch upwind of the site that is agricultural, as is evident in the satellite image of the region shown in Figure 2.1. The ammonia sensitivity is also broadly consistent with a pair of characteristics of the ambient  $\text{PM}_{10}$  shown in Figure 3.8: i) nitrate was only 10% of  $\text{PM}_{10}$  during the study, with about half of that being organic nitrates, while it was 42% of  $\text{PM}_{2.5}$  for the Bakersfield CSN site from 2015 To 2019 (Figure 2.2) and ii) ammonium was only 3% of  $\text{PM}_{10}$  while sulfate was 17%, suggesting the aerosol was acidic and any free gas-phase ammonia would be lost to reactive uptake.

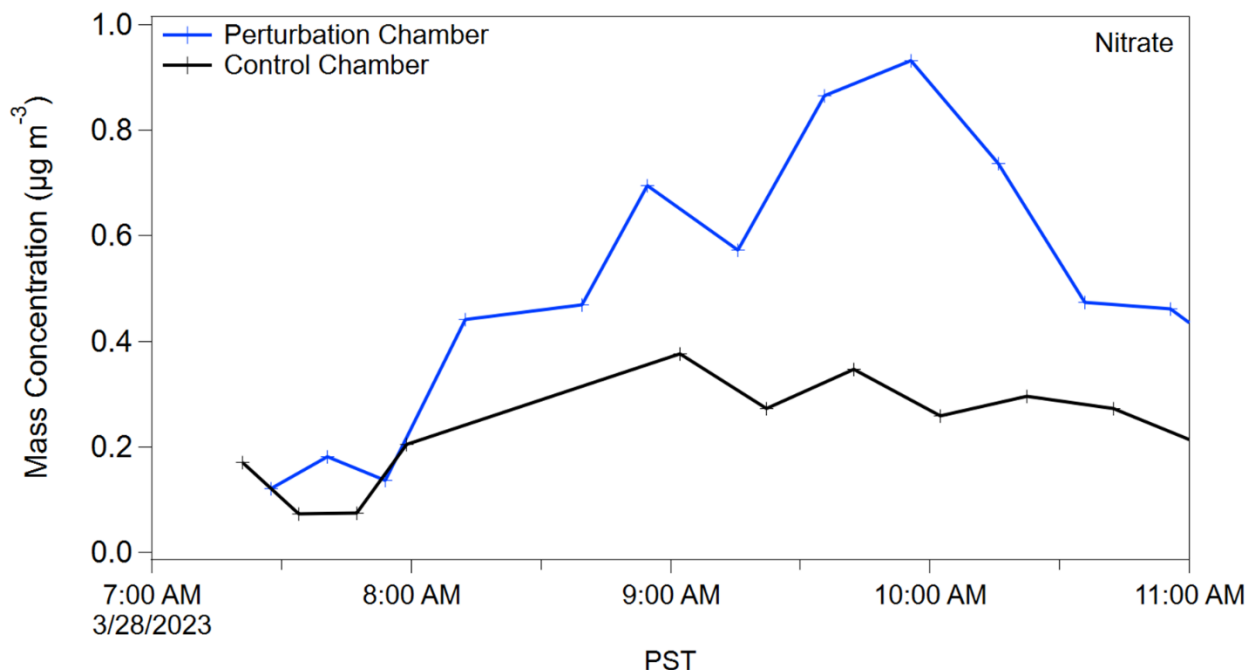


Figure 3.18. Mass concentration of nitrate aerosol in both chambers during NH<sub>3</sub> perturbation experiments in Wilmington on March 28, 2023. The perturbation began at 7:30 am and continued for 8 h.

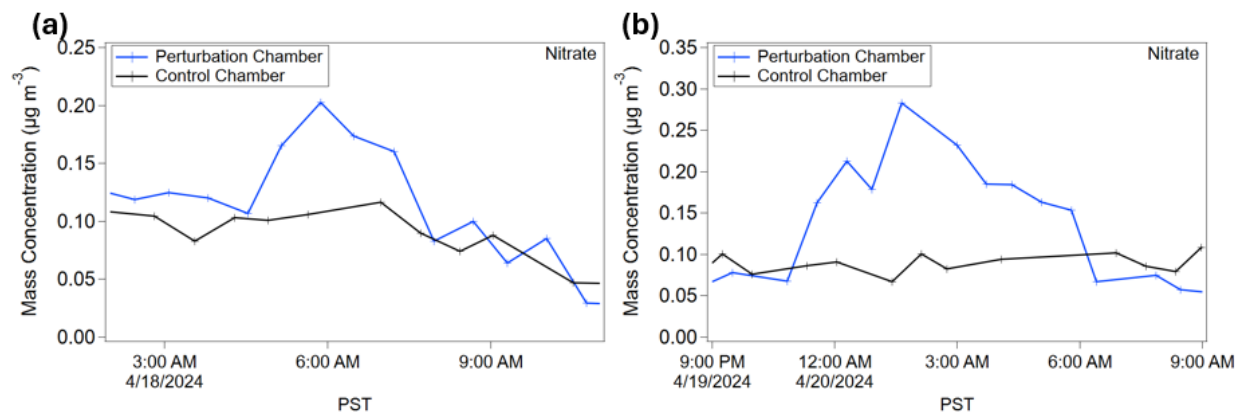


Figure 3.19. Mass concentration of nitrate aerosol in both chambers during NH<sub>3</sub> perturbation experiments in Bakersfield on (a) April 18, 2024, and (b) April 20, 2024. The perturbations were applied continuously from April 17 to April 20, 2024.

### 3.3.4 Summary of Perturbation Experiments Results

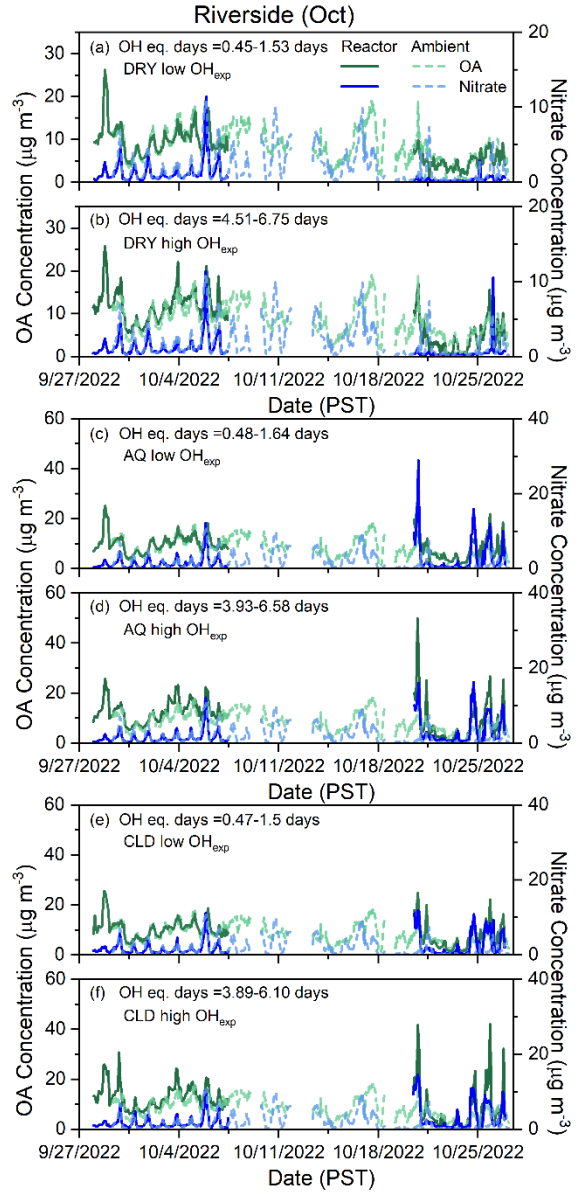
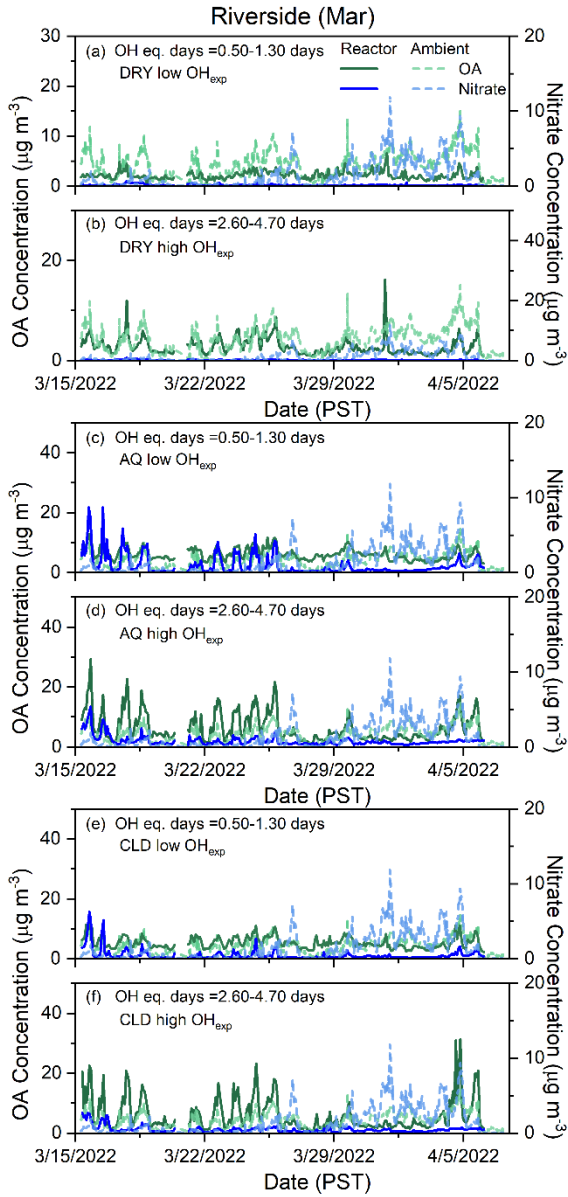
During VOC perturbation experiments, distinct behaviors in aerosol growth and composition were observed. The addition of the biogenic VOCs alpha-pinene and isoprene, particularly under nighttime conditions, favored aerosol formation and growth. The experiments highlighted the inhibitory effect of isoprene on alpha-pinene-induced SOA formation, suggesting a complex interaction between different types of VOCs. On the other hand, the introduction of toluene, a representative anthropogenic VOC, led to new particle formation and demonstrated the importance of VOC type on the resulting aerosol.

The NO<sub>2</sub> perturbation experiments revealed different outcomes across the studies sites, highlighting the influence of local environmental conditions on aerosol formation. In the ammonia-limited environments of Riverside and Wilmington, NO<sub>2</sub> perturbations had no impact on aerosol concentration, suggesting that NH<sub>3</sub> availability, not NO<sub>x</sub>, controlled nitrate formation during those experiments. However, at Bakersfield site, NO<sub>2</sub> perturbations triggered nitrate aerosol formation on one of ten experiments, presumably when sufficient NH<sub>3</sub> was available.

NH<sub>3</sub> perturbation increased aerosol production across all sites. In Riverside and Wilmington, NH<sub>3</sub> injections contributed to immediate and substantial particle growth and new particle formation, characterized by an increase in nitrate aerosol concentration followed by an increase in organic aerosol. These results highlight the critical role of ammonia in enhancing aerosol formation in NO<sub>x</sub>-rich environments, as well as the contribution of organics to ammonium-related reactions. In Bakersfield, NH<sub>3</sub> perturbations had more variable response, with no observed impact for four of the six perturbation experiments and with modest inorganic nitrate formation without a corresponding enhancement in organic aerosol during the other two.

### 3.4 Secondary Aerosol Formation in the APPA Reactor

Figure 3.20 presents the time series of organic and nitrate mass concentrations measured in both ambient air and in ambient air processed through the APPA reactor during the four field campaigns. During the Riverside (Oct) campaign, a significant leak was identified in the tubing between the APPA reactor outlet and the AMS inlet that affected measurements between September 28 and October 7, 2022. In addition, the reactor experienced frequent operational interruptions between October 8 and October 20, 2022. As a result, only data from the final week (October 21–27, 2022) are included in the analysis for that campaign. Elevated organic mass concentrations in air processed through the reactor relative to ambient levels were frequently observed across all campaigns, particularly under high OH exposure and when liquid water was present on the seed particles. For example, in Bakersfield (Apr), as shown in Figure 3.20 (d, f), the green line representing reactor OA frequently peaks higher than the green dashed line representing ambient OA at corresponding times. However, during certain periods, reactor OA concentrations were lower than ambient levels, particularly for dry seed aerosol experiment with low OH<sub>exp</sub>. As described in Section 2.3.5, the concentration in reactor-processed air can be less than that in ambient air because ambient particles are removed upstream of the reactor and only secondary aerosol is present in what is measured at the outlet. Higher ambient than secondary concentration can indicate that most gas-phase precursors have already reacted and their products partitioned into the particle phase, leaving limited precursor gases available for oxidation within the reactor. When comparing nitrate concentrations between the reactor and ambient air, Riverside (Mar) and Bakersfield (Apr) generally exhibited similar or lower concentrations in the reactor than in the ambient environment, whereas Riverside (Oct) and Wilmington (Mar) showed higher concentrations in the reactor relative to ambient, particularly under aqueous seed aerosol and cloud droplets conditions with higher water content. The OA enhancements highlight the potential for substantial secondary aerosol formation, which may significantly contribute to ambient PM<sub>2.5</sub> levels. Sulfate concentration is not reported because the background level associated with the injected seed particles is comparatively high, resulting in excessive uncertainty when subtracting it to calculate the amount formed in the reactor.



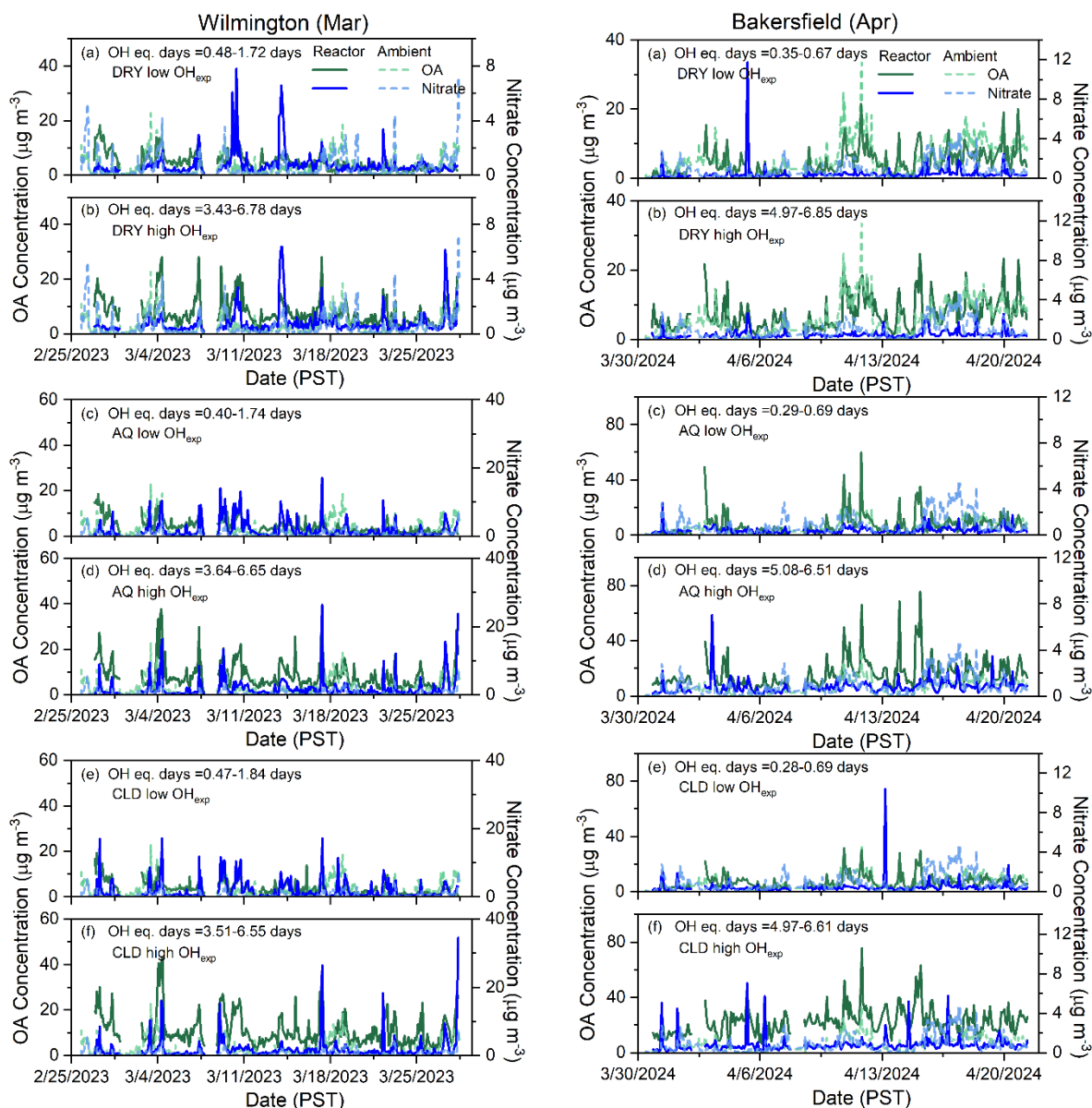


Figure 3.20. Time series of organic and nitrate mass concentrations measured in the reactor and ambient air under six experimental conditions: (a) dry seed aerosol at low OH exposure (DRY low  $\text{OH}_{\text{exp}}$ ), (b) dry seed aerosol at high OH exposure (DRY high  $\text{OH}_{\text{exp}}$ ), (c) aqueous seed aerosol at low OH exposure (AQ low  $\text{OH}_{\text{exp}}$ ), (d) aqueous seed aerosol at high OH exposure (AQ high  $\text{OH}_{\text{exp}}$ ), (e) cloud droplets at low OH exposure (CLD low  $\text{OH}_{\text{exp}}$ ), and (f) cloud droplets at high OH exposure (CLD high  $\text{OH}_{\text{exp}}$ ). Data are presented for all four campaigns: Riverside (Mar) (top left), Riverside (Oct) (top right), Wilmington (Mar) (bottom left), and Bakersfield (Apr) (bottom right).

Tables 3.3 and 3.4 summarize the estimated OH exposures and corresponding equivalent photochemical ages under low and high oxidation conditions at each RH level for each campaign. OH exposure was estimated using the KinSim chemical kinetics simulator (Peng and Jimenez, 2019), which incorporates the 254 nm UV intensity profile and ozone photolysis loss as model inputs. Under low OH exposure, the

corresponding photochemical ages were 0.25–0.38, 0.45–1.64, 0.40–1.84, and 0.28–0.69 days for Riverside (Mar), Riverside (Oct), Wilmington (Mar), and Bakersfield (Apr), respectively. Under high OH exposure, the photochemical ages increased to 1.40–2.30, 3.89–6.75, 3.43–6.78, and 4.97–6.85 days for the same sites, respectively.

Table 3.3. Estimated OH exposure (molecules  $\text{cm}^{-3} \text{s}^{-1}$ ) under different conditions across the four field campaigns.

OH exposure (molec $\text{cm}^{-3} \text{s}$ )	Riverside (Mar) (2022)	Riverside (Oct) (2022)	Wilmington (Mar) (2023)	Bakersfield (Apr) (2024)
Dry seed, low $\text{OH}_{\text{exp}}$	$(3.20\text{--}4.90) \times 10^{10}$	$(5.80\text{--}19.9) \times 10^{10}$	$(6.19\text{--}22.3) \times 10^{10}$	$(4.53\text{--}8.65) \times 10^{10}$
Dry seed, high $\text{OH}_{\text{exp}}$	$(1.60\text{--}2.90) \times 10^{11}$	$(5.84\text{--}8.75) \times 10^{11}$	$(4.45\text{--}8.79) \times 10^{11}$	$(6.44\text{--}8.88) \times 10^{11}$
Aqueous seed, low $\text{OH}_{\text{exp}}$	$(3.20\text{--}4.90) \times 10^{10}$	$(6.20\text{--}21.3) \times 10^{10}$	$(5.13\text{--}22.6) \times 10^{10}$	$(3.71\text{--}8.91) \times 10^{10}$
Aqueous seed, high $\text{OH}_{\text{exp}}$	$(1.60\text{--}2.90) \times 10^{11}$	$(5.09\text{--}8.53) \times 10^{11}$	$(4.72\text{--}8.61) \times 10^{11}$	$(6.59\text{--}8.44) \times 10^{11}$
Cloud droplets, low $\text{OH}_{\text{exp}}$	$(3.20\text{--}4.90) \times 10^{10}$	$(6.07\text{--}19.4) \times 10^{10}$	$(6.06\text{--}23.9) \times 10^{10}$	$(3.66\text{--}8.99) \times 10^{10}$
Cloud droplets, high $\text{OH}_{\text{exp}}$	$(1.60\text{--}2.90) \times 10^{11}$	$(5.04\text{--}7.90) \times 10^{11}$	$(4.55\text{--}8.49) \times 10^{11}$	$(6.44\text{--}8.57) \times 10^{11}$

Table 3.4. Estimated equivalent photochemical age (days) under different conditions across four field campaigns, assuming the average atmospheric OH is  $1.5 \times 10^6 \text{ cm}^{-3}$ .

Equivalent photochemical age (days)	Riverside (Mar) (2022)	Riverside (Oct) (2022)	Wilmington (Mar) (2023)	Bakersfield (Apr) (2024)
Dry seed, low $\text{OH}_{\text{exp}}$	0.25 to 0.38	0.45 to 1.53	0.48 to 1.72	0.35 to 0.67
Dry seed, high $\text{OH}_{\text{exp}}$	1.30 to 2.30	4.51 to 6.75	3.43 to 6.78	4.97 to 6.85
Aqueous seed, low $\text{OH}_{\text{exp}}$	0.25 to 0.38	0.48 to 1.64	0.40 to 1.74	0.29 to 0.69
Aqueous seed, high $\text{OH}_{\text{exp}}$	1.30 to 2.30	3.93 to 6.58	3.64 to 6.65	5.08 to 6.51
Cloud droplets, low $\text{OH}_{\text{exp}}$	0.25 to 0.38	0.47 to 1.50	0.47 to 1.84	0.28 to 0.69
Cloud droplets, high $\text{OH}_{\text{exp}}$	1.30 to 2.30	3.89 to 6.10	3.51 to 6.55	4.97 to 6.61

### 3.4.1 Organic and Nitrate Aerosol Enhancements

Figure 3.21 presents the average concentrations of secondary organic and nitrate aerosol, measured by the mAMS, under various seed aerosol water content and OH exposure conditions for each campaign. The liquid water content was varied as the RH was stepped between 40%, 85%, and 100% to create environments in the reactor with dry seed aerosol, aqueous seed aerosol, and cloud droplets, respectively. For each RH condition, the OH exposure varied between low and high levels, resulting in the six experimental conditions: dry seed aerosol at low OH exposure (DRY low  $\text{OH}_{\text{exp}}$ ), dry seed aerosol at high OH exposure (DRY high  $\text{OH}_{\text{exp}}$ ), aqueous seed aerosol at low OH exposure (AQ low  $\text{OH}_{\text{exp}}$ ), aqueous seed aerosol at high OH exposure (AQ high  $\text{OH}_{\text{exp}}$ ), cloud droplets at low OH exposure (CLD low  $\text{OH}_{\text{exp}}$ ), and cloud droplets at high OH exposure (CLD high  $\text{OH}_{\text{exp}}$ ). Organic and nitrate aerosol concentrations

measured by the mAMS in ambient air and in the air processed through the APPA are summarized in Tables 3.5 and 3.6.

When comparing secondary organic aerosol and nitrate aerosol concentrations across the six reactor conditions, the influence of water content and OH exposure varied among sites. During the Riverside (Mar and Oct) campaigns, water content was the dominant factor, with both SOA and nitrate concentrations significantly enhanced under AQ and CLD conditions at both low and high OH exposures relative to DRY. Previous studies similarly demonstrate the importance of aerosol liquid water in secondary aerosol formation. For example, Chen et al. (2021) showed that elevated aerosol water content promotes nitrate oxidation, partitioning, and nocturnal  $\text{N}_2\text{O}_5$  hydrolysis, leading to enhanced nitrate formation. Meng et al. (2024) reported that elevated aerosol liquid water enhances multiphase processing and is associated with increased secondary organic aerosol formation during haze events. These findings highlight the significant contribution of aqueous-phase chemistry to secondary aerosol production, a pathway that remains poorly constrained in current models.

The relatively small difference in secondary aerosol enhancement between AQ and CLD conditions likely reflects equilibrium limitations rather than kinetic constraints. First, SOA formation may be limited by the availability of reactive precursors in the ambient air. Second, most water-soluble oxidation intermediates are expected to have already partitioned into the aqueous phase once sufficient aerosol liquid water is present. Finally, further dilution in cloud droplets does not substantially shift gas-aqueous equilibrium toward additional organic uptake, as partitioning may already approach saturation under AQ.

In Wilmington (Mar), OH exposure exerted the strongest influence on SOA formation, while nitrate concentrations, similar to Riverside, increased markedly with water content. SOA levels under high OH exposure (3.43–6.78 days) were consistently higher than those under low OH exposure (0.40–1.84 days) across all three RH conditions (DRY, AQ, and CLD), whereas nitrate concentrations were substantially higher under AQ and CLD conditions compared to DRY. This dependence of SOA on OH exposure is consistent with Palm et al. (2016), who reported that net SOA production in the Los Angeles region peaks at intermediate photochemical ages ( $\sim 0.8$ –6 days), followed by net OA loss at more advanced aging due to fragmentation. For Bakersfield (Apr), both OH exposure and water content played important roles, as SOA and nitrate concentrations were elevated under AQ high  $\text{OH}_{\text{exp}}$  and CLD high  $\text{OH}_{\text{exp}}$  conditions.

Across all campaigns, organic and nitrate concentrations were generally higher in reactor-processed air than that in ambient air, with the magnitude of enhancement varying by OH exposure level, water content level, and site. Organic aerosol concentrations showed the most significant increase under aqueous seed and cloud droplet conditions at high OH exposure. These results demonstrate the significant influence of water content and oxidative aging on secondary aerosol formation, as well as regional variety in precursor availability and photochemical reactivity in the atmosphere.

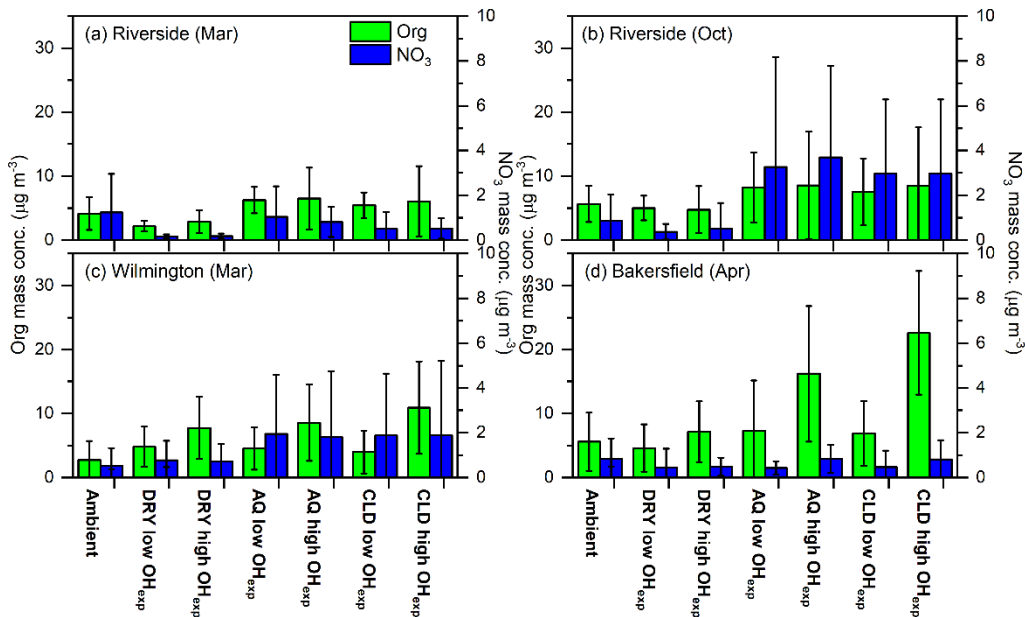


Figure 3.21. Average mass concentration of nitrate and organic aerosol in ambient air and from the OFR for different conditions. (a) Riverside (Mar), (b) Riverside (Oct), (c) Wilmington (Mar), (d) Bakersfield (Apr).

Table 3.5. Average, median, maximum, and standard deviation of organic aerosol concentrations ( $\mu\text{g m}^{-3}$ ) at the three sites during March/April campaigns under different conditions.

<b>Organics</b>			
Ambient	Measurement site		
Statistics	<b>Riverside (2022)</b>	<b>Wilmington (2023)</b>	<b>Bakersfield (2024)</b>
Average	4.18	2.75	5.59
Median	4.06	1.67	4.33
Max	15.07	17.32	31.59
SD	2.58	2.97	4.56
Dry seed, low OH <sub>exp</sub>	Measurement site		
Statistics	<b>Riverside (2022)</b>	<b>Wilmington (2023)</b>	<b>Bakersfield (2024)</b>
Average	2.20	4.83	4.60
Median	2.03	4.09	3.67
Max	6.62	18.38	21.52
SD	0.80	3.13	3.71
Dry seed, high OH <sub>exp</sub>	Measurement site		
Statistics	<b>Riverside (2022)</b>	<b>Wilmington (2023)</b>	<b>Bakersfield (2024)</b>
Average	2.88	7.75	7.15
Median	2.39	6.49	5.71
Max	16.17	28.14	24.72

SD	1.79	4.86	4.76
Aqueous seed, low OH <sub>exp</sub>	Measurement site		
Statistics	<b>Riverside (2022)</b>	<b>Wilmington (2023)</b>	<b>Bakersfield (2024)</b>
Average	6.26	4.55	7.29
Median	5.85	3.58	5.05
Max	12.88	18.64	59.89
SD	2.05	3.32	7.86
Aqueous seed, high OH <sub>exp</sub>	Measurement site		
Statistics	<b>Riverside (2022)</b>	<b>Wilmington (2023)</b>	<b>Bakersfield (2024)</b>
Average	6.50	8.59	16.20
Median	4.50	6.74	13.18
Max	29.41	37.76	75.40
SD	4.83	6.00	10.60
Cloud droplets, low OH <sub>exp</sub>	Measurement site		
Statistics	<b>Riverside (2022)</b>	<b>Wilmington (2023)</b>	<b>Bakersfield (2024)</b>
Average	5.45	3.98	6.90
Median	4.96	3.12	5.79
Max	11.64	19.72	31.67
SD	1.98	3.32	5.05
Cloud droplets, high OH <sub>exp</sub>	Measurement site		
Statistics	<b>Riverside (2022)</b>	<b>Wilmington (2023)</b>	<b>Bakersfield (2024)</b>
Average	6.07	10.90	22.59
Median	3.65	8.62	21.99
Max	31.31	42.87	75.34
SD	5.49	7.20	9.65

Table 3.6. Average, median, maximum, and standard deviation of nitrate aerosol concentrations ( $\mu\text{g m}^{-3}$ ) at the three sites during March/April campaigns under different conditions.

<b>Nitrate</b>			
Ambient	Measurement site		
Statistics	<b>Riverside (2022)</b>	<b>Wilmington (2023)</b>	<b>Bakersfield (2024)</b>
Average	1.24	0.51	0.84
Median	0.48	0.17	0.53
Max	11.82	6.76	4.56
SD	1.72	0.80	0.91
Dry seed, low OH <sub>exp</sub>	Measurement site		
Statistics	<b>Riverside (2022)</b>	<b>Wilmington (2023)</b>	<b>Bakersfield (2024)</b>
Average	0.17	0.77	0.46
Median	0.13	0.55	0.33
Max	0.73	7.82	11.72
SD	0.10	0.88	0.83

Dry seed, high OH <sub>exp</sub> Statistics	Measurement site		
	<b>Riverside (2022)</b>	<b>Wilmington (2023)</b>	<b>Bakersfield (2024)</b>
Average	0.18	0.73	0.49
Median	0.15	0.54	0.39
Max	1.01	6.38	2.68
SD	0.12	0.77	0.40
Aqueous seed, low OH <sub>exp</sub> Statistics	Measurement site		
	<b>Riverside (2022)</b>	<b>Wilmington (2023)</b>	<b>Bakersfield (2024)</b>
Average	1.04	1.95	0.43
Median	0.45	0.79	0.36
Max	8.74	17.06	2.80
SD	1.36	2.64	0.30
Aqueous seed, high OH <sub>exp</sub> Statistics	Measurement site		
	<b>Riverside (2022)</b>	<b>Wilmington (2023)</b>	<b>Bakersfield (2024)</b>
Average	0.82	1.82	0.83
Median	0.63	0.90	0.72
Max	5.40	26.42	7.06
SD	0.67	2.93	0.63
Cloud droplets, low OH <sub>exp</sub> Statistics	Measurement site		
	<b>Riverside (2022)</b>	<b>Wilmington (2023)</b>	<b>Bakersfield (2024)</b>
Average	0.52	1.89	0.48
Median	0.28	0.64	0.36
Max	6.29	17.16	10.40
SD	0.74	2.75	0.73
Cloud droplets, high OH <sub>exp</sub> Statistics	Measurement site		
	<b>Riverside (2022)</b>	<b>Wilmington (2023)</b>	<b>Bakersfield (2024)</b>
Average	0.52	1.89	0.82
Median	0.40	0.95	0.67
Max	2.72	34.61	7.02
SD	0.45	3.33	0.86

### 3.4.2 Relative Organic Aerosol Enhancements

Figure 3.22 presents the relative organic aerosol (OA) enhancement ( $ER_{OA} = \text{reactor OA} / \text{DRY low OH}_{exp} \text{ OA}$ ) for three selected 8-hour intervals: 2:00–10:00 AM, 10:00 AM–6:00 PM, and 6:00 PM–2:00 AM. These intervals were chosen to capture periods of relative stability in concentrations that span rush hour activity and the diurnal variability in atmospheric gas concentrations. Relative OA enhancement was evaluated for five experimental conditions - DRY high OH<sub>exp</sub>, AQ low and high OH<sub>exp</sub>, and CLD low and high OH<sub>exp</sub> - against the DRY low OH<sub>exp</sub> baseline.

For both the Riverside (Mar) and (Oct) campaigns, water content played a predominant role in  $ER_{OA}$ . During the Riverside (Mar) campaign, elevated  $ER_{OA}$  values were observed during the first and third intervals under AQ and CLD conditions, with averages ranging from 2.51–3.07 and 2.28–3.04,

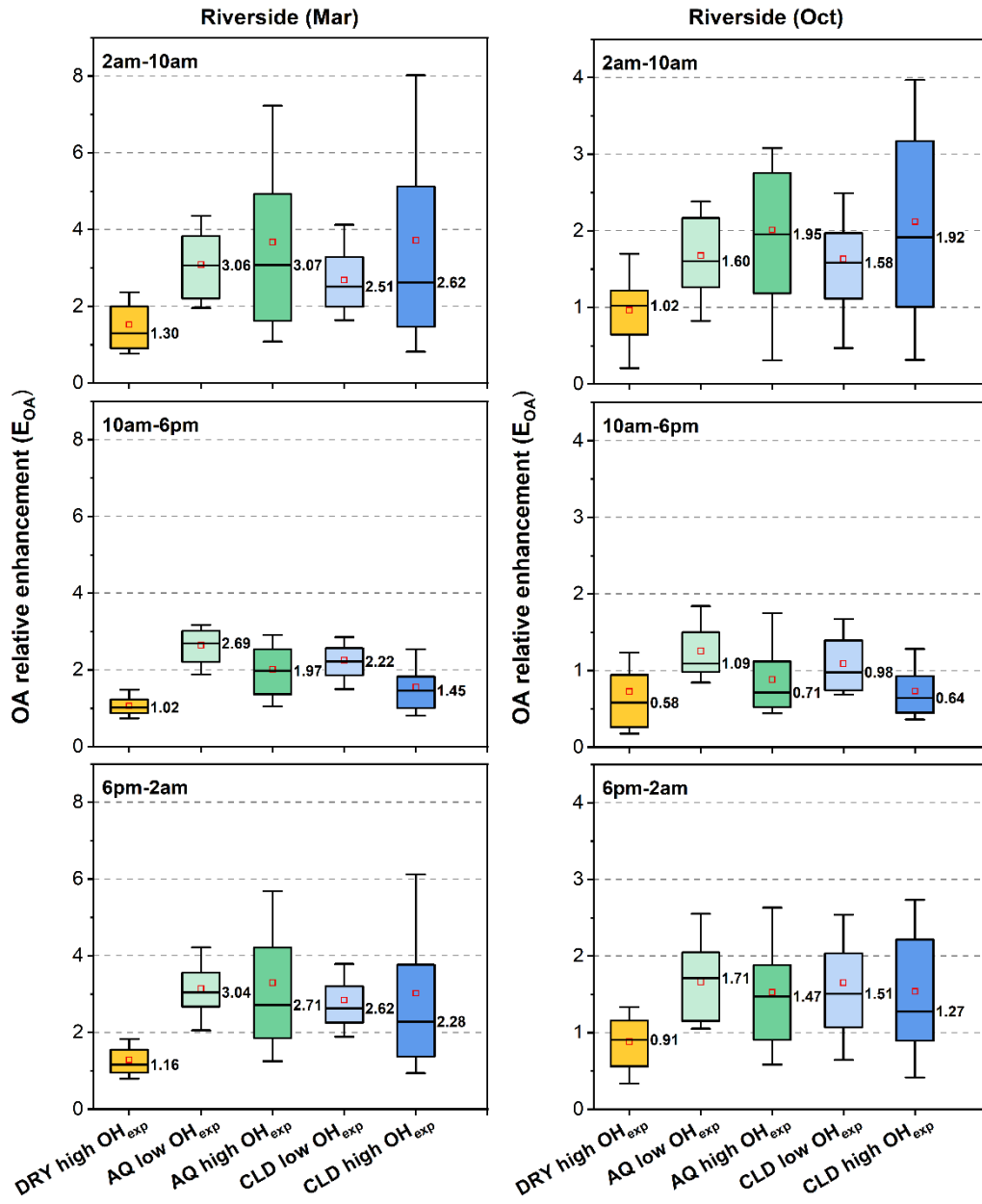
respectively. However, the second interval exhibited lower average enhancements (1.45–2.69). A similar pattern was observed during the Riverside (Oct) campaign, with average  $ER_{OA}$  under AQ and CLD conditions of 1.58–1.95 (first interval), 0.64–1.09 (second), and 1.27–1.71 (third). Notably, data availability for this campaign was limited to the final week (October 21–27, 2022). Therefore, the results may not be representative.

Across both Riverside campaigns, the second 8-hour interval exhibits the lowest  $ER_{OA}$ . This reduction is likely driven by depletion of reactive atmospheric precursor gases under elevated ambient OH levels. Enhanced daytime vertical mixing further dilutes precursor concentrations, limiting their availability for further oxidation in the APPA reactor. Additionally, average  $ER_{OA}$  during the second interval is significantly lower under high  $OH_{exp}$  than under low  $OH_{exp}$ . A possible explanation is that with low precursor concentrations, higher OH concentrations within the reactor promotes multigenerational oxidation, shifting the dominant chemistry from functionalization toward fragmentation. The associated increase in product volatility favors evaporation, resulting in net OA loss rather than additional SOA formation.

For the Wilmington (Mar) campaign, OH exposure was the dominant factor influencing the relative OA enhancement. For the first 8-hour interval, average  $ER_{OA}$  values were 1.80 (DRY high  $OH_{exp}$ ), 0.86 (AQ low  $OH_{exp}$ ), 2.10 (AQ high  $OH_{exp}$ ), 0.72 (CLD low  $OH_{exp}$ ), and 2.54 (CLD high  $OH_{exp}$ ). For the second and third intervals in the five conditions, the enhancements were 1.30, 0.90, 1.55, 0.68, and 1.82; and 1.63, 0.85, 1.70, 0.67, and 2.23, respectively.

In Bakersfield, both OH exposure and water content contributed significantly to the relative OA enhancement. Under AQ high  $OH_{exp}$ ,  $ER_{OA}$  increased to 3.89, 3.42, and 3.92 for the first, second, and third intervals, respectively. Even higher enhancements were observed under CLD high  $OH_{exp}$ , reaching 5.83, 4.91, and 5.15 for the corresponding periods.

The distinct  $ER_{OA}$  sensitivities across the three sites reflect localized SOA formation regimes driven by differences in precursor composition and atmospheric processing. In Riverside,  $ER_{OA}$  is primarily controlled by aerosol water content, as air masses are typically photochemically aged and enriched in oxygenated VOCs and semi- and intermediate-VOCs (S/IVOCs) transported downwind from the Los Angeles basin. Under these conditions, additional gas-phase oxidation alone is often insufficient to substantially increase SOA mass, and multiphase processing dominates. In contrast,  $ER_{OA}$  in Wilmington is mainly governed by OH exposure, reflecting efficient gas-phase oxidation of relatively fresh urban and industrial emissions. Bakersfield displays an intermediate regime, in which both OH exposure and water content contribute substantially to  $ER_{OA}$ , indicative of combined influences from biogenic emissions, anthropogenic sources, and multiphase processing. Overall, our findings are consistent with other OFR field studies conducted in both urban and forest environments, which also report enhanced nighttime SOA formation (Ortega et al., 2016; Palm et al., 2016; Xu et al., 2022; Zhang et al., 2024). In particular, greater OA enhancements during the first and third intervals suggest significant SOA formation potential during nighttime hours, though it is important to note that measures of aerosol formation from OH oxidation are less relevant at nighttime due to the low concentration in ambient air. Site-specific differences in precursor levels and meteorological conditions likely contribute to the variability in OA enhancement observed across the three study locations.



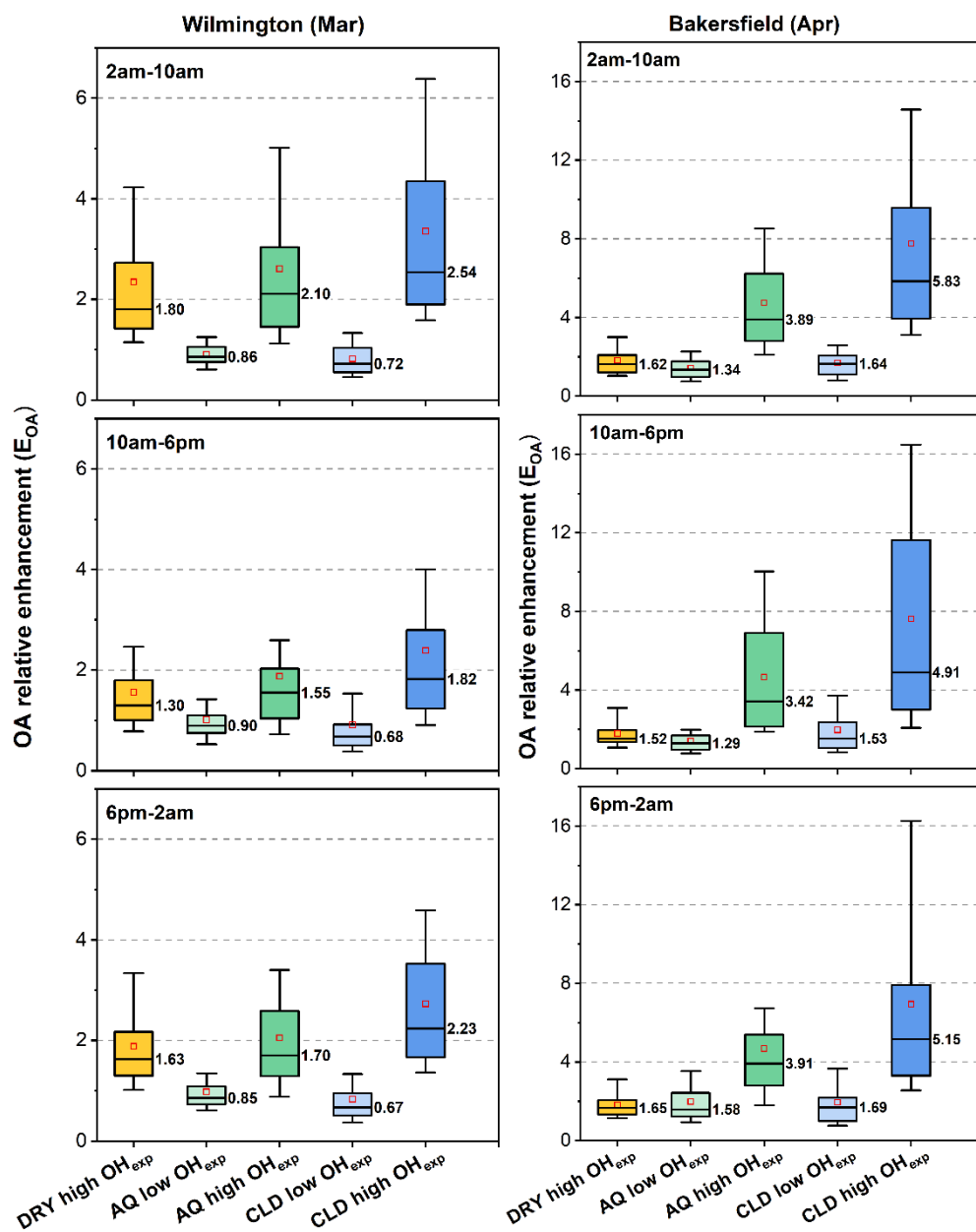


Figure 3.22. Secondary aerosol enhancement at different reactor conditions relative to that at DRY low OH exp for the first 8h interval (2am-10 am), second 8h interval (10 am-6 pm), and third 8h interval (6 pm-2 am). Box and whisker plots with the average value (dot) and the 10<sup>th</sup>, 25<sup>th</sup>, 50<sup>th</sup> (median), 75<sup>th</sup>, and 90<sup>th</sup> percentiles. Data are presented for the four campaigns: Riverside (Mar) (top left), Riverside (Oct) (top right), Wilmington (Mar) (bottom left), and Bakersfield (Apr) (bottom right).

### 3.4.3 Diel Trends

Figure 3.23 presents the diel variation in OA mass concentrations under different reactor conditions as well as that of the ambient aerosol. Diel profiles of selected gas-phase species and PM<sub>2.5</sub> are also shown. Hourly average data across the four field campaigns are compared.

The SOA diel patterns (Figure 3.23a–f) exhibited distinct temporal and site-specific characteristics. Under DRY low  $\text{OH}_{\text{exp}}$  (a, c, and e), SOA formation remained relatively constant throughout the day, whereas variability was higher under high  $\text{OH}_{\text{exp}}$  conditions (b, d, f), with the magnitude greatest for AQ and CLD at Bakersfield. At Bakersfield (green line of Figure 3.23f), SOA concentrations increased during the early morning (04:00–08:00 PST) due to nighttime precursor accumulation and a shallow boundary layer, followed by an afternoon decline from boundary layer deepening and atmospheric precursor depletion. A second evening peak (19:00–20:00 PST) was observed in both ambient and all reactor conditions, suggesting a dominant influence on local precursor emissions. This behavior is likely driven by elevated monoterpene emissions during the local citrus blooming period that spanned the duration of the campaign. Previous work (Fares et al., 2012) reported that monoterpene concentrations exhibited pronounced diel patterns and were substantially enhanced during blooming, consistent with the late-evening SOA peak observed here.

In contrast, secondary aerosol measurements from Riverside (Mar and Oct), and Wilmington (Mar) (Figure 3.23 d, f) showed less diel variability, with peaks generally aligned with morning traffic emissions (06:00–10:00 PST) and subsequent afternoon declines, stabilizing in the early evening. Ambient OA (Figure 3.23g) displayed a broadly similar pattern to that of SOA formed in the reactor but with generally lower amplitude, with slight morning enhancements, reflecting local emission patterns and boundary layer dynamics. This reduced ambient response indicates that a substantial fraction of SOA formation potential is not fully reflected in ambient OA and may contribute to elevated  $\text{PM}_{2.5}$  following further atmospheric processing and cloud processing. Consistent with the reactor results, ambient OA in Riverside and Wilmington also lacks a pronounced early-evening SOA production regime, suggesting weaker evening biogenic VOC emissions and a more anthropogenically dominated precursor mixture that limits nighttime secondary aerosol formation.

Gas-phase species followed characteristic source- and meteorology-driven diel cycles. Mean concentrations of  $\text{NO}$ ,  $\text{NO}_x$ , and  $\text{CO}$  (Figures 3.23h–j) exhibited sharp morning peaks (06:00–08:00 PST) from traffic emissions, followed by a gradual decrease in the afternoon. Ambient  $\text{PM}_{2.5}$  (Figure 3.23k) concentrations increased in the morning and again in the evening, while  $\text{O}_3$  (Figure 3.23l) shows a strong afternoon peak (~14:00–16:00 PST).

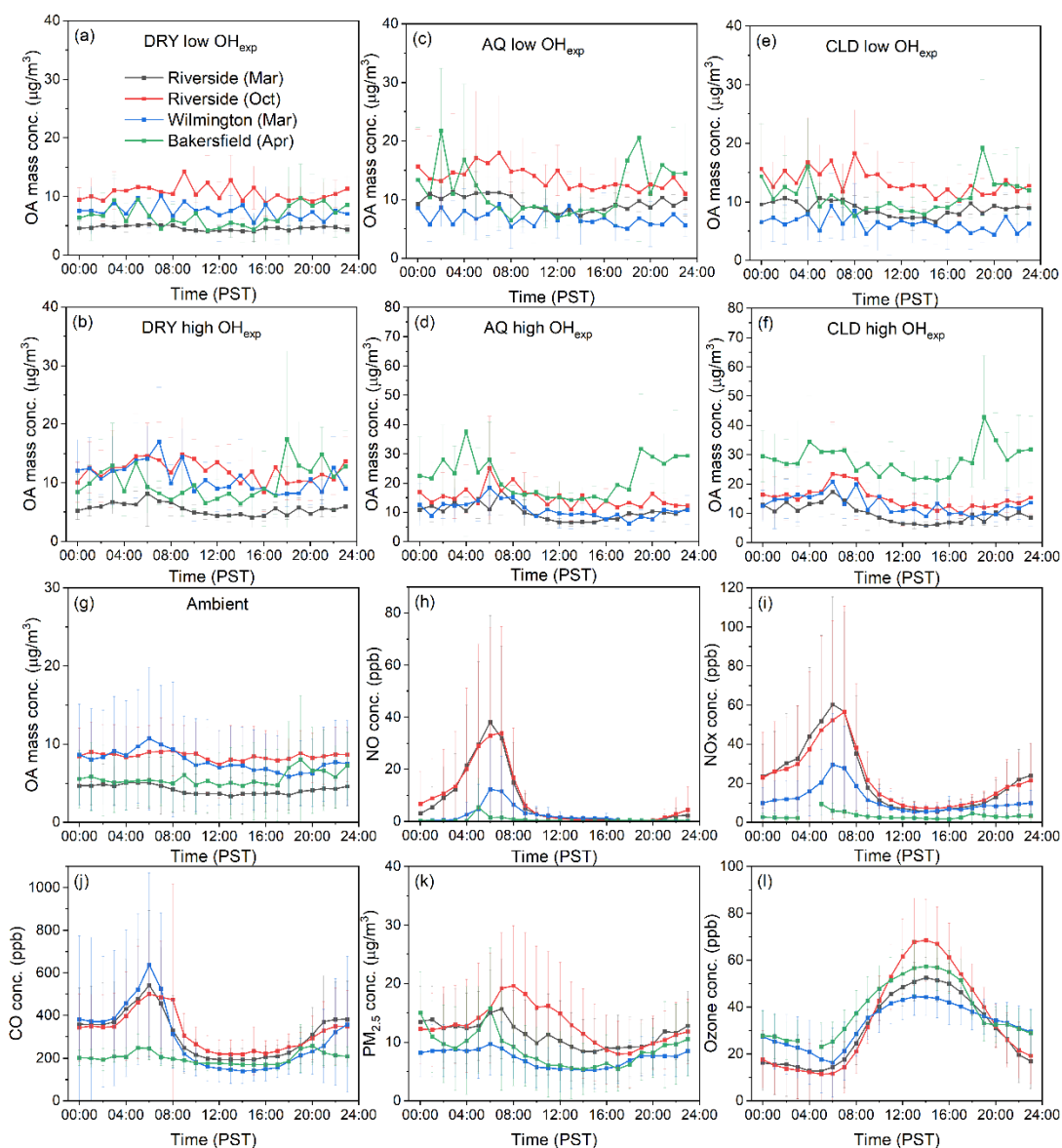


Figure 3.23. Diurnal profiles of SOA concentrations ( $\mu\text{g m}^{-3}$ ) under each experimental condition: (a) DRY low  $\text{OH}_{\text{exp}}$ , (b) DRY high  $\text{OH}_{\text{exp}}$ , (c) AQ low  $\text{OH}_{\text{exp}}$ , (d) AQ high  $\text{OH}_{\text{exp}}$ , (e) CLD low  $\text{OH}_{\text{exp}}$ , (f) CLD high  $\text{OH}_{\text{exp}}$ , and (g) ambient. Panels (h–l) show the diurnal variation of key ambient gas- and particle-phase species: (h) NO (ppb), (i)  $\text{NO}_x$  (ppb), (j) CO (ppb), (k)  $\text{PM}_{2.5}$  ( $\mu\text{g m}^{-3}$ ), and (l)  $\text{O}_3$  (ppb).

### 3.4.4 Organic Aerosol Evolution

Figures 3.24–3.27 present the time series of  $f_{44}$  (middle) and  $f_{43}$  (top) for ambient and reactor conditions, along with box-and-whisker plots (bottom) summarizing their distributions under each reactor condition.  $f_{44}$  is the fractional contribution of  $\text{CO}_2^+$  at  $m/z$  44, while  $f_{43}$  is the  $\text{C}_2\text{H}_3\text{O}^+$  fraction at  $m/z$  43. In the previous work (Ng et al., 2011; Ortega et al., 2016; W. Xu et al., 2022),  $f_{44}$  is typically associated with more oxidized organic aerosol (OA), whereas  $f_{43}$  is linked to freshly formed OA. In the Riverside campaigns,  $f_{43}$  decreased markedly and  $f_{44}$  increased during experiments with aqueous seed aerosol and

cloud droplets relative to dry seed aerosol experiments, indicating more oxidized OA formation at higher water content and aqueous-phase processing plays a critical role in OA compositions. Sareen et al. (2016, 2017) demonstrated that gas-phase oxidation produces water-soluble organic gases, such as isoprene epoxydiol, glyoxal, and methylglyoxal, which further undergo aqueous-phase reactions in wet aerosols, clouds, and fog. These processes lead to the formation of aqueous secondary organic aerosol that is substantially more oxidized than SOA formed exclusively through gas-phase pathways. Feng et al. (2022) provided field evidence showing that highly oxidized OA exhibits a strong correlation with elevated aerosol water content (AWC), further underscoring the importance of aqueous-phase chemistry in OA aging and evolution.

Similar trends were observed when comparing high- to low-OH exposure conditions, with higher OH exposure resulting in increased  $f_{44}$  and decreased  $f_{43}$ . Ng et al. (2010) reported that more aged, low-volatility oxygenated organic aerosol (LV-OOA) exhibits enhanced  $f_{44}$  and suppressed  $f_{43}$  relative to semi-volatile oxygenated aerosol (SV-OOA). It's supported by time-resolved measurements in Riverside that reveal a progressive shift in OA composition from SV-OOA toward LV-OOA with increasing photochemical aging. This observed trend is consistent with previous studies (Ortega et al., 2013, Pfaffenberger et al. 2013, Hersey et al. 2011). This composition shift reflects multigenerational oxidation, which enhances the abundance of highly oxygenated functional groups, such as carboxylic acids, manifested by increased contributions at  $m/z$  44 and LV-OOA formation.

In Wilmington,  $f_{44}$  remained consistently higher and  $f_{43}$  lower under high-OH exposure, while water content exerted a minimal influence on either parameter. In Bakersfield, both increased OH exposure and elevated water content promoted more oxidized OA formation, with the most considerable enhancement in  $f_{44}$  observed under higher RH and high OH exposure conditions. These site-dependent differences indicate that the dominant drivers of OA oxidation state depend strongly on regional meteorology, aerosol composition, and precursor variability. In nitrate-rich inland regions such as Riverside, elevated aerosol liquid water promotes aqueous-phase processing, leading to higher  $f_{44}$  and lower  $f_{43}$ . In contrast, at the coastal Wilmington site, precursors may be largely pre-processed under humid conditions in the atmosphere prior to sampling, leaving gas-phase OH oxidation as the primary driver of OA evolution in the reactor. In transitional regions such as Bakersfield, aqueous- and gas-phase oxidation pathways act together to shape OA composition.

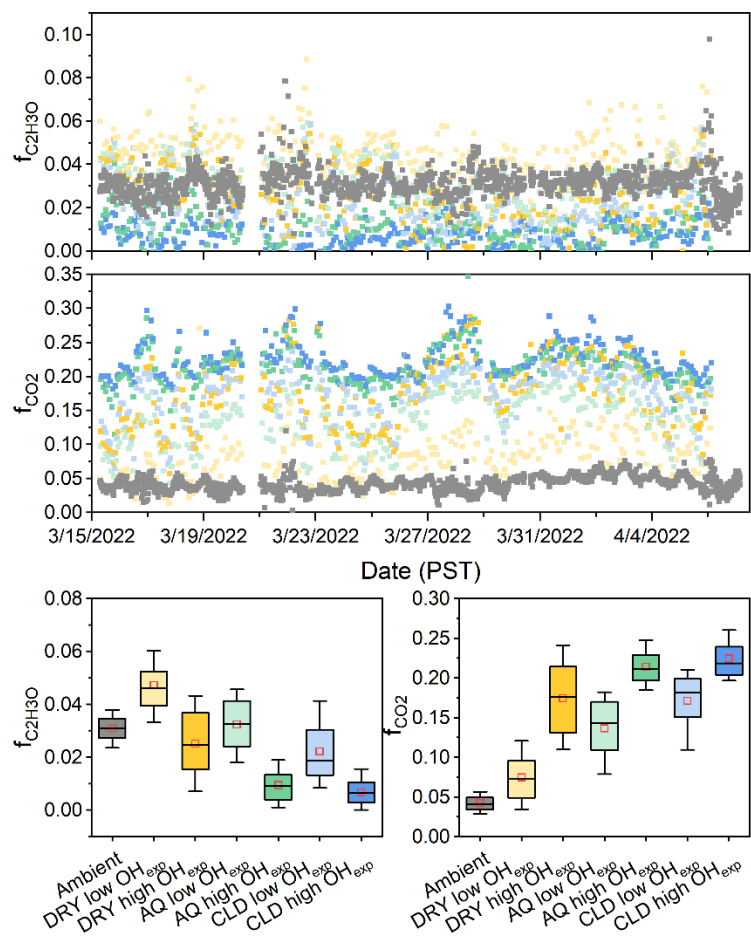


Figure 3.24. Time series and statistical distributions of f43 ( $f_{C_2H_3O}$ ), and f44 ( $f_{CO_2}$ ) for Riverside (Mar). Box and whisker plots with the average value (dot) and the 10th, 25th, 50th (median), 75th, and 90th percentiles. The ambient condition is shown in grey, while the six reactor conditions (DRY low and high  $OH_{exp}$ , AQ low and high  $OH_{exp}$ , and CLD low and high  $OH_{exp}$ ) are color-coded as light yellow, yellow, light green, green, light blue, and blue, respectively. The same color scheme is used for both scatter and box plots.

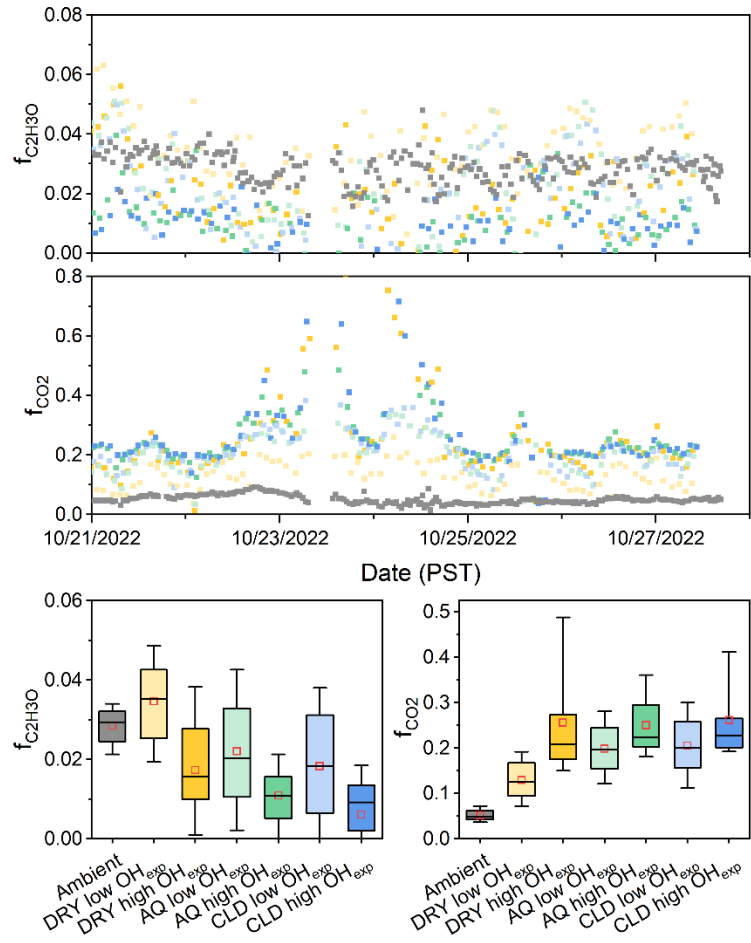


Figure 3.25. Time series and statistical distributions of f43 ( $f_{C_2H_3O}$ ), and f44 ( $f_{CO_2}$ ) for Riverside (Oct). Box and whisker plots with the average value (dot) and the 10th, 25th, 50th (median), 75th, and 90th percentiles.

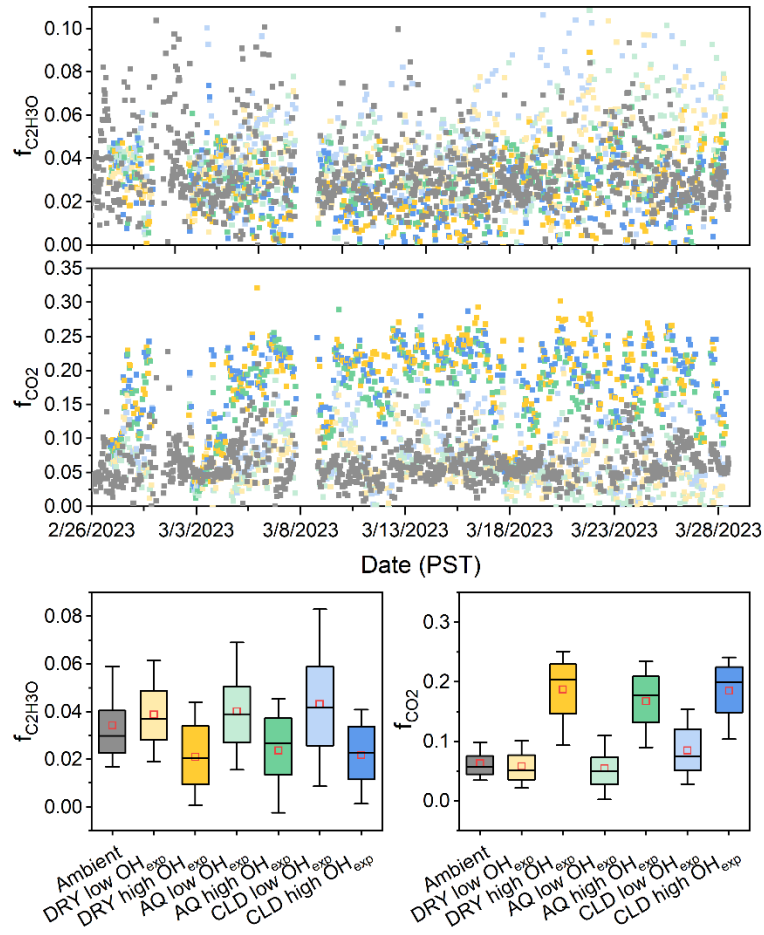


Figure 3.26. Time series and statistical distributions of f43 ( $f_{C_2H_3O}$ ), and f44 ( $f_{CO_2}$ ) for Wilmington (Mar). Box and whisker plots with the average value (dot) and the 10th, 25th, 50th (median), 75th, and 90th percentiles.

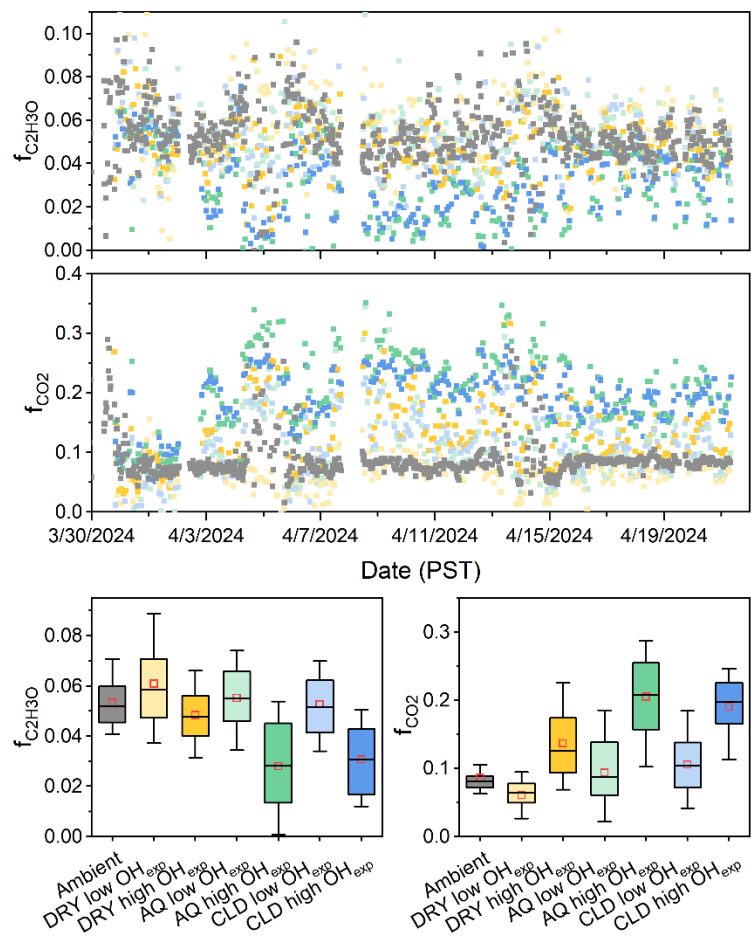


Figure 3.27. Time series and statistical distributions of f43 ( $f_{C_2H_3O}$ ), and f44 ( $f_{CO_2}$ ) for Bakersfield (Apr). Box and whisker plots with the average value (dot) and the 10th, 25th, 50th (median), 75th, and 90th percentiles.

### 3.4.5 Summary and Implications

APPA reactor measurements across the four field campaigns show that secondary aerosol formation is strongly regulated by extent of photochemical processing and aerosol water content, with clear site-dependent behavior driven by differences in precursor composition and atmospheric processing. Secondary organic aerosol and nitrate concentrations formed in the reactor were generally highest under high OH exposure and elevated relative humidity. Secondary aerosol formation in Riverside was most sensitive to liquid water content in the particles accompanying the precursor gases from sampled ambient air, that in Wilmington was most sensitive to OH exposure, and that in Bakersfield was comparably sensitive to water content and OH exposure. In addition to mass enhancement, reactor processing led to aerosol evolution toward more oxidized compositions under both higher water content and higher OH exposure, evidenced by increased  $f_{44}$  and decreased  $f_{43}$ . These trends indicate

multigenerational oxidation and aqueous-phase processing, promoting the formation of low-volatility, highly oxygenated organic aerosol.

From a policy perspective, these findings highlight the need for air quality strategies and chemical transport models to account for multiphase oxidation pathways. This effect is particularly important in inland and downwind regions where transported, oxygenated VOCs and humid conditions potentially amplify secondary PM<sub>2.5</sub> formation. Additionally, the strong regional contrasts highlight the need for location-specific mitigation approaches, with controls on fresh reactive emissions most effective near source regions (e.g., Wilmington) and strategies addressing transported, oxygenated precursors and multiphase processing more relevant downwind (e.g., Riverside).

## 4.1 Source Apportionment of Ambient Organic Aerosol through PMF

### 4.1.1 PMF Methodology

Given the large contribution of OA to NR-PM1 mass (Figures 4.1-4.4), additional analysis was carried out to characterize different types of OA and their sources using positive matrix factorization (PMF) (Paatero and Tapper, 1994; Ulbrich et al., 2009). The ambient OA unit-mass resolution mass spectra from each campaign along with their corresponding error matrices, were used in an Igor-based toolkit (v. 3.0) for PMF analysis (Ulbrich et al., 2009) and different number of solution sets (up to at least 8 factors) were investigated. Consistent with common practices in PMF, the data with signal to noise ratio between 0.2-2 were down-weighted by a factor of 2 while bad data, defined as any data with signal to noise less than 0.2, were removed from the analysis. Furthermore, data from fragments whose signals are somehow related to each other in the interpretation of mAMS mass spectra (i.e., m/z 16,17, 18, 28, and 44) were considered weak and down-weighted by a factor of 2. PMF results were examined for similarity/difference between the mass spectra and time series of the factors within one solution set. The number of factors (or sources) was selected to minimize  $Q/Q_{exp}$  as long as the factors were not split (i.e., resulting in highly similar time series of factor mass spectra profile). Although variations due to different  $f_{peak}$  and seed values were also explored, the final set of solutions correspond to  $f_{peak}=0$  and  $seed=0$ . To assess stability of the selected final solutions, 100 bootstrap runs were also carried out. The correlation coefficient ( $r$ ) between the base- PMF factor profiles and the average bootstrapped solutions was greater than 0.97 for all factors except factor 3 of PMF results in Bakersfield (Apr) (where the highest  $r$  was 0.87), suggesting the overall robustness of the selected final solution factors.

Typically, correlations among the resolved factors and external parameters are used to finalize the selection of the solution and to assign specific sources/formation processes to each factor. Here, we relied on knowledge from previous investigations of OA sources, lab-based mass spectral characteristics of different OA types, expected diurnal trends in different sources, correlations with the AMS-based measurements of nitrate and sulfate, and correlations with eBC (when available), CO, NO<sub>x</sub>, and ozone by CARB or the South Coast Air Quality Management District (Table 4.1). It is worth noting that since most of the auxiliary gas measurements were not made at the same site, less than ideal correlations are expected in these comparisons.

#### 4.1.2 Results and Discussion

The measured ambient OA was attributed to 4-6 sources in each campaign, summary of which are provided in Figures 4.1-4.4. The fresh, hydrocarbon-like OA (HOA) factors are identified based on the dominance of ion fragments at  $m/z$  41, 43, 55, 57, 69, 71, etc. that is a common hydrocarbon fragmentation pattern upon electron-impact ionization (McLafferty and Turecek, 1993a; Zhang et al., 2005). The mass spectra of the HOA factors are highly similar ( $r^2 > 0.89$ ) among all sites. The diurnal profile of this factor at all sites suggests strong association with vehicular traffic emissions, especially during morning rush hours. Variable levels of correlations were observed between HOA and CO ( $r^2 = 0.15-0.65$ ), eBC ( $r^2 = 0.32-0.57$ ), and NO<sub>x</sub> ( $r^2 = 0.03-0.59$ ). The lower correlation coefficients between HOA and the auxiliary gases is likely due to lack of co-location between the aerosol and gas measurements. It is interesting to note that during Wilmington (Mar), the contribution of the HOA factor did not decrease as quickly as at the other campaigns after the morning rush hour. This may be due to the proximity of the sampling site during Wilmington (Mar) to the Ports of Los Angeles and Long Beach and influence of port-related traffic beyond the typical morning rush hours.

The fresh biomass burning OA (BBOA) factor has a similar fragmentation pattern to the HOA factors with the exception of having contributions at  $m/z$  60 and  $m/z$  73 which are associated with combustion of sugars (Cubison et al., 2011; Zhang et al., 2011). The diurnal profiles of this factor were very similar during Riverside (Mar), Riverside (Oct), and Wilmington (Mar) with a peak in its fractional contribution in late afternoon until midnight. Its correlation coefficient was highest with CO, nitrate or sulfate (depending on the campaign) (Table 4.1). Sources of BBOA could be longer-range transported BBOA or local sources from residential biomass burning. A fresh BBOA factor was not identified as a source of OA during Bakersfield (Apr).

The cooking OA (COA) factor profile is also very similar to that of HOA and BBOA (minus the strong contribution from  $m/z$  60 and 73), but with a higher contribution of  $m/z$  55 instead of  $m/z$  57 (Allan et al., 2010; Mohr et al., 2012, 2009; Vasilakopoulou et al., 2023). Unlike observations at major cities with close proximities of the measurement sites to restaurants with peak emissions during meal times (e.g., Allan et al., 2010, (Hayes et al., 2013)), there isn't a significant variation in the diurnal profiles of COA in Riverside or Wilmington.

The oxygenated OA (OOA) factors are characterized by a strong signal at  $m/z$  28 (CO<sup>+</sup>) and  $m/z$  44 (CO<sub>2</sub><sup>+</sup>) (Ng et al., 2010; Zhang et al., 2007). During Riverside (Mar) and Riverside (Oct), the OOA could further be classified into More Oxidized OOA (MO-OOA) and Less Oxidized OOA (LO-OOA), based on the relative contribution from  $m/z$  43 (Zhang et al., 2011, 2019). Compared to MO-OOA, LO-OOA has a relatively higher contribution at  $m/z$  43, suggesting some contribution of less oxygenated fragments. Diurnal profiles of OOA showed significant increase in its fractional contribution in early- to mid-afternoon, consistent with its link to photochemical processes. The OOA factors showed highest correlations with sulfate and/or nitrate (Table 4.1).

Except for Riverside (Mar), additional unique factors were also resolved. A unique factor was identified during Riverside (Oct) and Bakersfield (Apr) with its mass spectra being similar to what has been observed in the laboratory from nitrate oxidation of biogenic volatile organic compounds (BVOCs), with a very high signal at  $m/z$  43 and much lower signal at  $m/z$  29 and 44 (He et al., 2021), and negligible signal at other ions. During Riverside (Oct), the mass concentration of this factor, named biogenic SOA (BSOA) peaked in the early morning hours while its fractional contribution was high throughout the day

except for the morning and afternoon rush hours, suggesting both daytime and nighttime formation of it. During Bakersfield (Apr), both the mass concentration and fractional contribution of this factor was high after sunset. Given recent work on the importance of BVOCs in Southern California during warmer months of the year (Pfannerstill et al., 2024) as well as the close proximity of the sampling site during Bakersfield (Apr) in Bakersfield to citrus fields, it is not surprising to have a measurable (25% in Riverside (Oct) and 31% in Bakersfield (Apr)) contribution from BSOA at these locations. Presence of a nighttime biogenic factor during Bakersfield (Apr) is also consistent with previous aerosol studies in Bakersfield during CalNex (Liu et al., 2012). The BSOA factor in both campaigns was best correlated with sulfate, consistent with its secondary nature. Although we are not able to differentiate the sulfate signal detected by mAMS to organic and inorganic portions, previous studies have observed formation of organosulfates from oxidation of BVOCs (Hettiyadura et al., 2019; Wang et al., 2022; Zhang et al., 2012).

Overall, secondary sources of OA dominated the OA composition at all sites. Considering the contributions of OOA and BSOA factors, overall, 48-65% of OA during these campaigns are secondary in nature, with the highest fraction observed in Bakersfield (Apr). In Bakersfield (Apr), 34% of OA was attributed to OOA and 31% to BSOA (Figure 4.4).

In Wilmington (Mar), a factor with a unique fragmentation pattern was consistently observed (Figure 4.3). Its concentration throughout the day remained more or less unchanged while its fractional contribution peaked in the early afternoon. Given the dominance of ions at  $m/z$  29, 31, and 45, which are common for primary alcohols (McLafferty and Turecek, 1993b), we attribute this factor to marine sources. There could also be some contribution from S- containing fragments (i.e.,  $\text{CHS}^+$ ) at  $m/z$  45, originating from marine dimethyl sulfide oxidation (Saarikoski et al., 2019) or a compound related to unique emissions from local industrial activities.

As mentioned above, in Bakersfield (Apr), we could not identify a source related to fresh biomass burning since none of the factors showed enhancement in  $m/z$  60 and 73. However, a factor rich in  $m/z$  44 as well as  $m/z$  41, 51, 55, 65, 67, 79, and 81 was resolved that has signatures of both aged and primary organic aerosols, hence called aged POA (Figure 4.4). The absolute concentration of this factor increased after sunset while its fractional contribution was relatively constant throughout the day. Given the higher correlation of this factor with sulfate and eBC, we speculate the source to be combustion related though the exact source (aged cooking or biomass burning or other solid fuel burning) remains unclear.

Table 3.7. Correlation coefficient of scatter plots between PMF factors and external variables during Riverside (Mar) (a), Riverside (Oct) (b), Wilmington (Mar) (c) and Bakersfield (Apr) (d).

a) Riverside (Mar)

r <sup>2</sup>	F1 MO-OOA	F2 LO-OOA	F3 BBOA	F4 HOA	F5 COA
CO	0.03	0.25	0.29	<b>0.65</b>	<b>0.53</b>
NO <sub>x</sub>	<0.01	0.08	0.11	<b>0.57</b>	0.28
O <sub>3</sub>	0.023	0.05	0.07	0.34	0.17
NO <sub>3</sub> <sup>-</sup>	<b>0.60</b>	<b>0.42</b>	<b>0.32</b>	0.08	0.06
SO <sub>4</sub> <sup>2-</sup>	<b>0.70</b>	<b>0.45</b>	<b>0.42</b>	0.05	0.05

b) Riverside (Oct)

r <sup>2</sup>	F1 LO-OOA	F2 MO-OOA	F3 BBOA	F4 BSOA	F5 COA	F6 HOA
CO	0.04	<0.01	0.11	0.07	0.24	<b>0.40</b>
NO <sub>x</sub>	<0.01	<0.01	0.04	<0.01	0.24	<b>0.59</b>
O <sub>3</sub>	0.01	0.23	<0.01	<0.01	0.03	0.19
NO <sub>3</sub> <sup>-</sup>	0.20	0.05	0.07	0.10	0.05	0.05
SO <sub>4</sub> <sup>2-</sup>	<b>0.50</b>	<b>0.37</b>	<b>0.30</b>	<b>0.39</b>	<0.01	<0.01
eBC	0.12	0.10	0.23	0.17	<b>0.38</b>	<b>0.57</b>

c) Wilmington (Mar)

r <sup>2</sup>	F1 Marine	F2 OOA	F3 COA+BBOA	F4 HOA
CO	0.27	<b>0.42</b>	0.30	0.35
NO <sub>x</sub>	0.20	0.34	0.23	0.32
O <sub>3</sub>	0.05	0.16	0.14	0.20
NO <sub>3</sub> <sup>-</sup>	<b>0.38</b>	<b>0.53</b>	<b>0.36</b>	<b>0.41</b>
SO <sub>4</sub> <sup>2-</sup>	0.23	0.18	0.06	0.06

d) Bakersfield (Apr)

r <sup>2</sup>	F1 OOA	F2 BSOA	F3 Aged POA	F4 HOA
CO	0.20	0.30	0.23	0.15
NO <sub>x</sub>	0.02	0.04	0.03	0.03
O <sub>3</sub>	0.09	0.01	0.05	0.09
NO <sub>3</sub> <sup>-</sup>	0.27	0.18	0.20	0.13
SO <sub>4</sub> <sup>2-</sup>	<b>0.66</b>	<b>0.41</b>	<b>0.48</b>	<b>0.36</b>
eBC	0.30	0.23	0.27	<b>0.32</b>

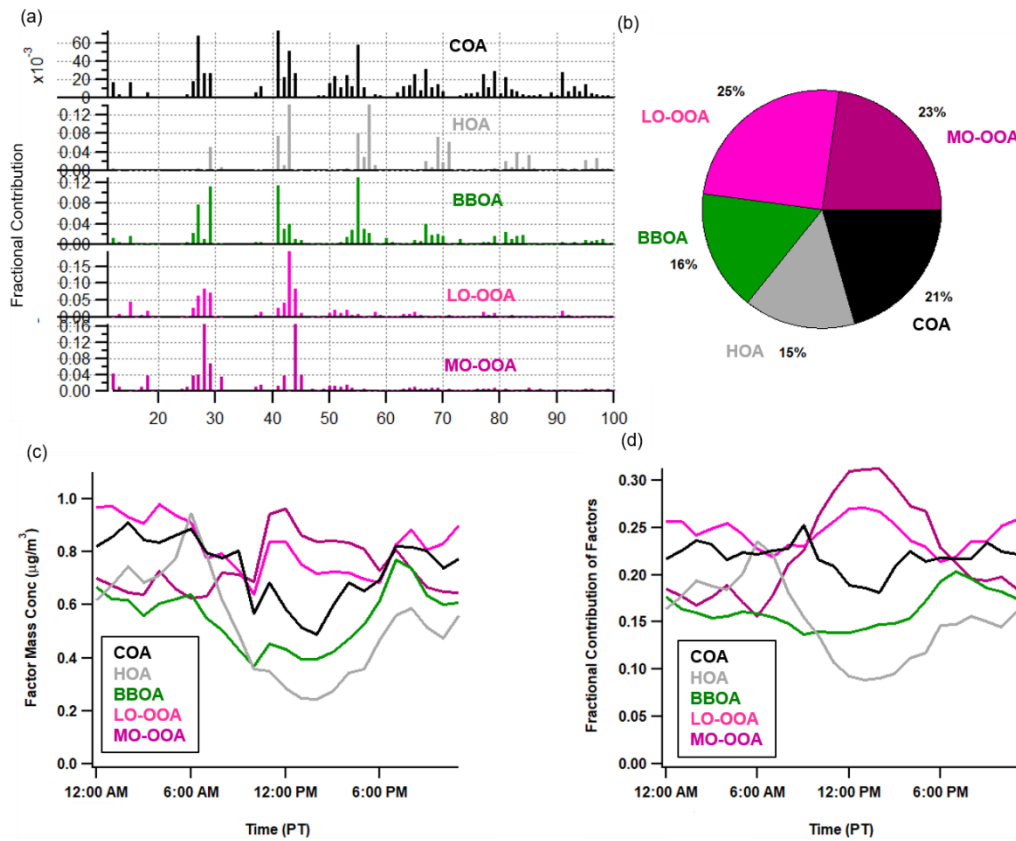


Figure 3.28. Summary of ambient OA PMF results for Riverside (Mar): (a) Mass spectral profiles of the resolved factors; (b) Average contributions of each PMF factor; (c) Diurnal profiles of the average mass concentration of each factor; (d) Diurnal profiles of the fractional contribution of each factor.

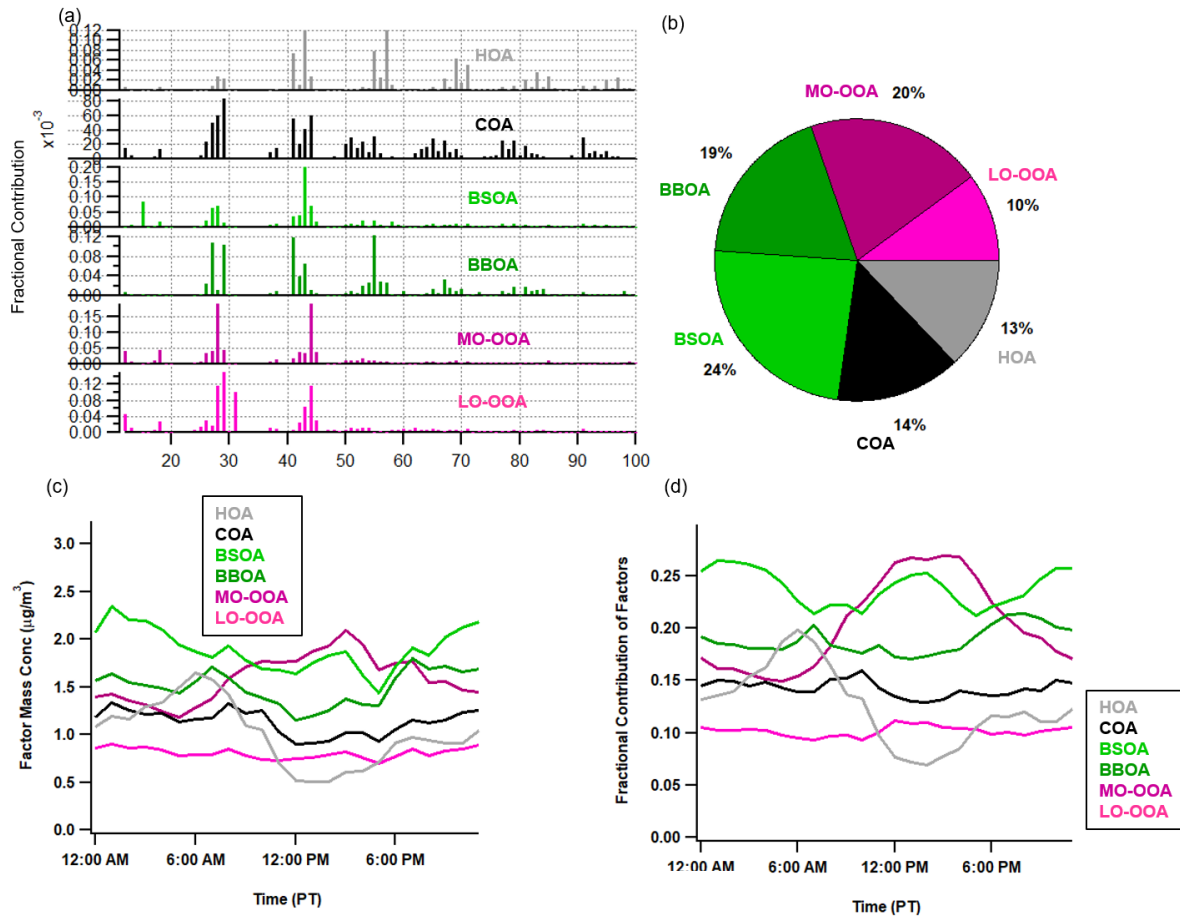


Figure 3.29. Summary of ambient OA PMF results for Riverside (Oct): (a) Mass spectral profiles of the resolved factors; (b) Average contributions of each PMF factor; (c) Diurnal profiles of the average mass concentration of each factor; (d) Diurnal profiles of the fractional contribution of each factor.

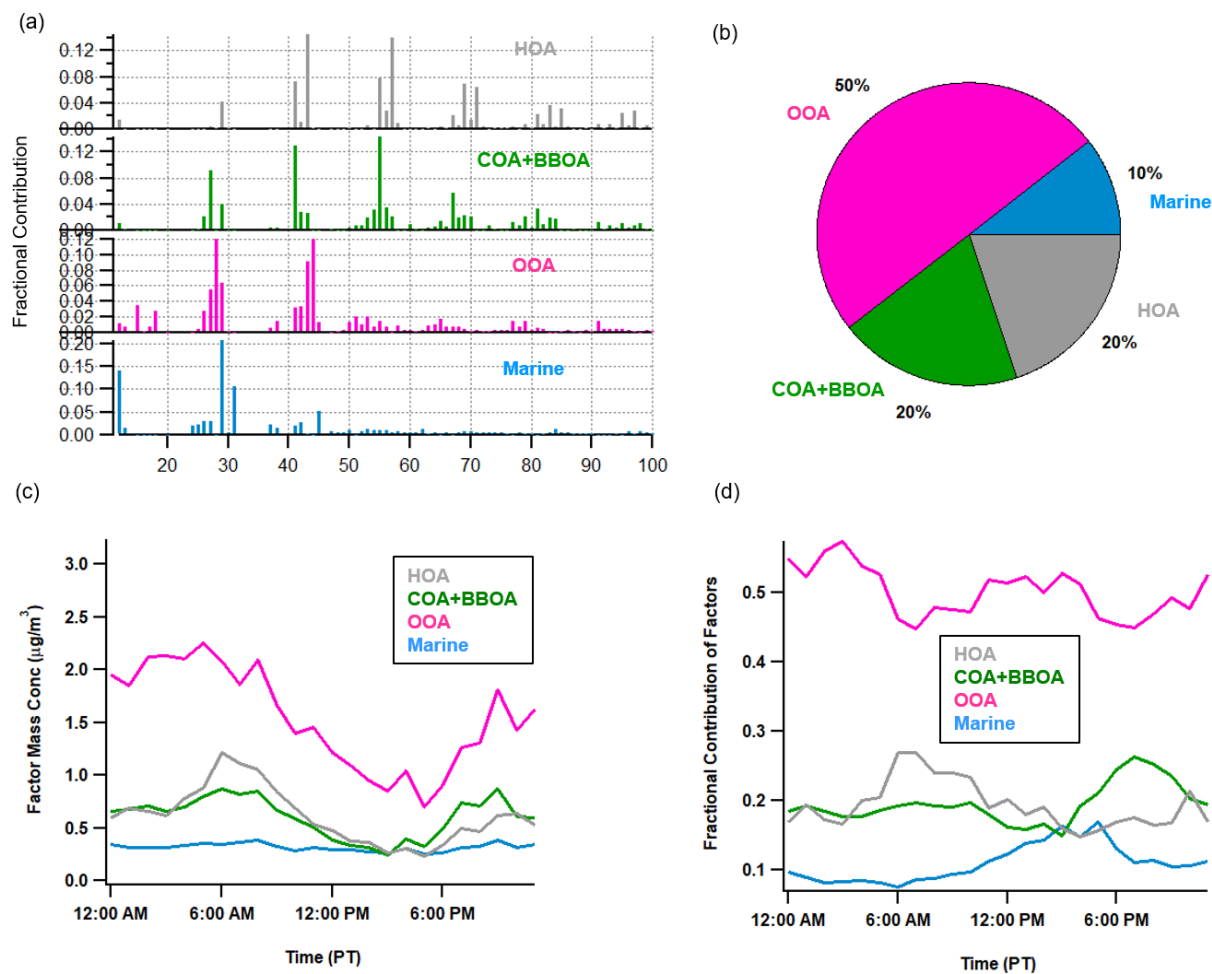


Figure 3.30. Summary of ambient OA PMF results for Wilmington (Mar): (a) Mass spectral profiles of the resolved factors; (b) Average contributions of each PMF factor; (c) Diurnal profiles of the average mass concentration of each factor; (d) Diurnal profiles of the fractional contribution of each factor.

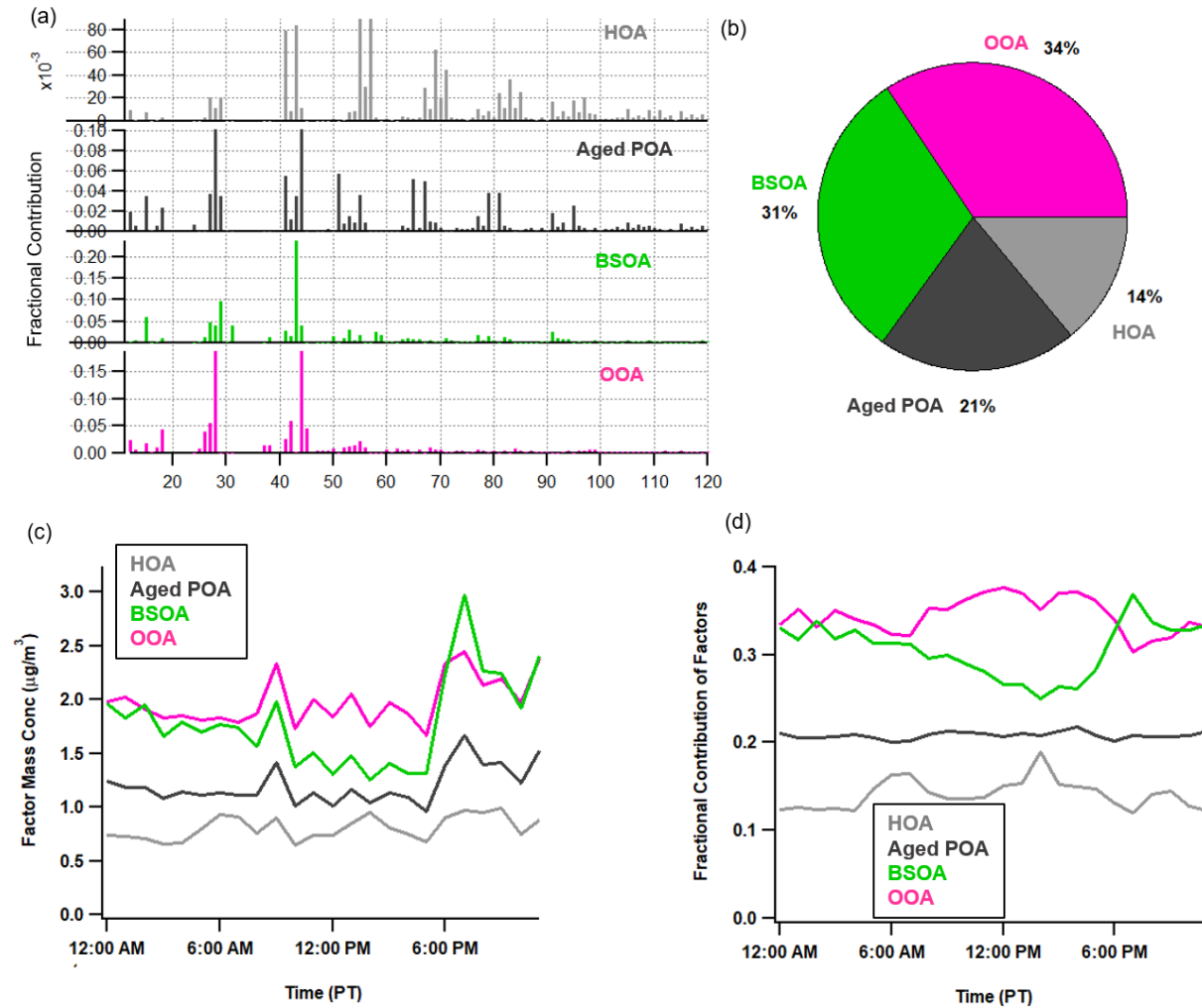


Figure 3.31. Summary of ambient OA PMF results for Bakersfield (Apr): (a) Mass spectral profiles of the resolved factors; (b) Average contributions of each PMF factor; (c) Diurnal profiles of the average mass concentration of each factor; (d) Diurnal profiles of the fractional contribution of each factor.

## 4.2. Generalized Additive Modeling (GAM)

### 4.2.1 Training Data

The training data are processed to investigate trends and short-term fluctuations separately. Trends are computed first as rolling 24-hour means, then diurnal cycles are calculated from the trends as the average of each hour of the day over the full data set. The denoised training data are the sum of trends and diurnal cycles. Detrended data are defined as the difference between the unprocessed data and the denoised data.

#### 4.2.2 Model Description

The models for each campaign and training set (i.e., the denoised and short-term fluctuations) are initialized as GAMs that predict OA trained against the covariates detailed in Table 4.2. We model OA because it is the major particulate species that exhibits the most complex behavior. The covariates are chosen as the widest pool of predictors for which we have collocated data coincident with AMS measurements.

Covariate	Description	Units	Data source
$\text{NH}_4^+$	Particulate ammonium	$\mu\text{g m}^3$	AMS (ambient)
$\text{SO}_4^{2-}$	Particulate sulfate	$\mu\text{g m}^3$	AMS (ambient)
$\text{NO}_3^-$	Particulate nitrate	$\mu\text{g m}^3$	AMS (ambient)
Cl <sup>-</sup>	Particulate chloride	$\mu\text{g m}^3$	AMS (ambient)
$\text{NO}_x$	Nitrogen oxides	ppm	ARB ambient monitor
CO	Carbon monoxide	ppm	ARB ambient monitor
$\text{O}_3$	Ozone	ppm	ARB ambient monitor
TEMP	Temperature	$^\circ\text{C}$	Nearby airport monitor
RH	Relative humidity	%	Nearby airport monitor
WS	Wind speed	$\text{m s}^{-1}$	Nearby airport monitor
WD	Wind direction	$^\circ$	Nearby airport monitor
$f_{43}$	m/z 43 mass fraction	Fraction (unitless)	AMS (ambient)
$f_{44}$	m/z 44 mass fraction	Fraction (unitless)	AMS (ambient)

Analysis of variance (ANOVA) is calculated for the initial model, then the covariate with the smallest  $F$  statistic (i.e., the least significant covariate) is dropped, and the model retrained. We repeat this process until dropping a covariate decreases the model  $R^2$  by 0.01 or more in a single iteration.

After denoising or detrending as described in Section 4.2.1, the training distributions become markedly less skewed. We therefore train GAMs assuming Gaussian distributions with identity link functions instead of the log-link Gamma distributions used in Task 1. Model performance is summarized in Table 4.3 with  $R^2$  defined as in Equation 1.8. As in section 4.2.1, the denoised data are the sum of rolling 24-hour trends and diurnal cycles while the detrended data are the difference between the unprocessed hourly data and the denoised data. Models are trained separately for the denoised and detrended data sets.

Table 3.83. Model performance measured as  $R^2$  for each campaign and training set.

Campaign	Denoised $R^2$	Detrended $R^2$
Riverside (Mar)	0.96	0.80
Riverside (Oct)	0.88	0.50
Wilmington (Mar)	0.91	0.66
Bakersfield (Apr)	0.91	0.42

#### 4.2.3 Marginal Effects

Because of the identity link used here, marginal effects are more directly obtained than in Task 1. They are simply the spline fit for each covariate, without the need for transformation. Because we have smaller

sets of covariates after variable selection, we present more than the most influential two marginal effects we showed in Task 1. This helps to contextualize the hourly models in more detail given the richer dynamics at this time scale.

#### 4.2.4 Riverside (Mar)

Focusing on rolling 24-hour trends and diurnal periodicity, ambient OA during this campaign is most parsimoniously characterized by  $\text{NO}_3^-$ ,  $\text{NO}_x$ , CO,  $\text{O}_3$ , and  $\text{SO}_4^{2-}$  (Figure 4.5). Because CO and  $\text{NO}_x$  are strongly correlated ( $r = 0.94$ ), they are likely related to mobile sources, which is further supported by their diurnal profiles that follow standard traffic patterns. This explains the positive associations of the marginal effects for CO (Figure 4.6), which is co-emitted with tailpipe POA and SOA precursors. This also helps explain the significance of  $\text{O}_3$  and the positive associations of its marginal effects (Figure 4.6), as ozonolysis of mobile source SOA precursors like alkanes can enhance OA through OOA formation (Zhang et al., 2014). From PMF we see that OOA makes up nearly half of OA by mass, on average, during this campaign.

$\text{SO}_4^{2-}$ , which likely comes from upwind sources (Mysliwiec and Kleeman, 2002), also displays positive associations in its marginal effects (Figure 4.6). This could be due to co-transport of upwind OA or acidic  $\text{SO}_4^{2-}$  seed particles catalyzing SOA formation (Gao et al., 2004; Jang et al., 2002), possibly a mix of both. The marginal effects of  $\text{NO}_3^-$  (Figure 4.6) are likely because most  $\text{NO}_3^-$  is organic, 67% on average.

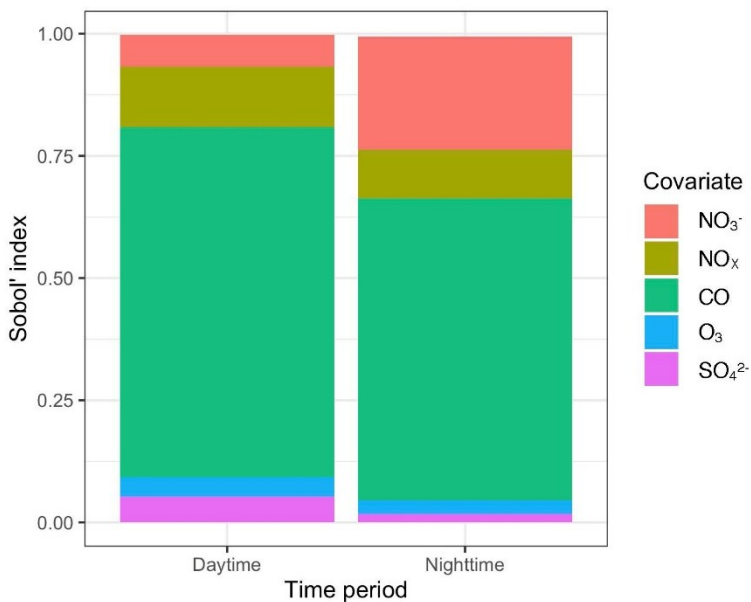


Figure 3.32. Sensitivity analysis for the Riverside (Mar) denoised model.

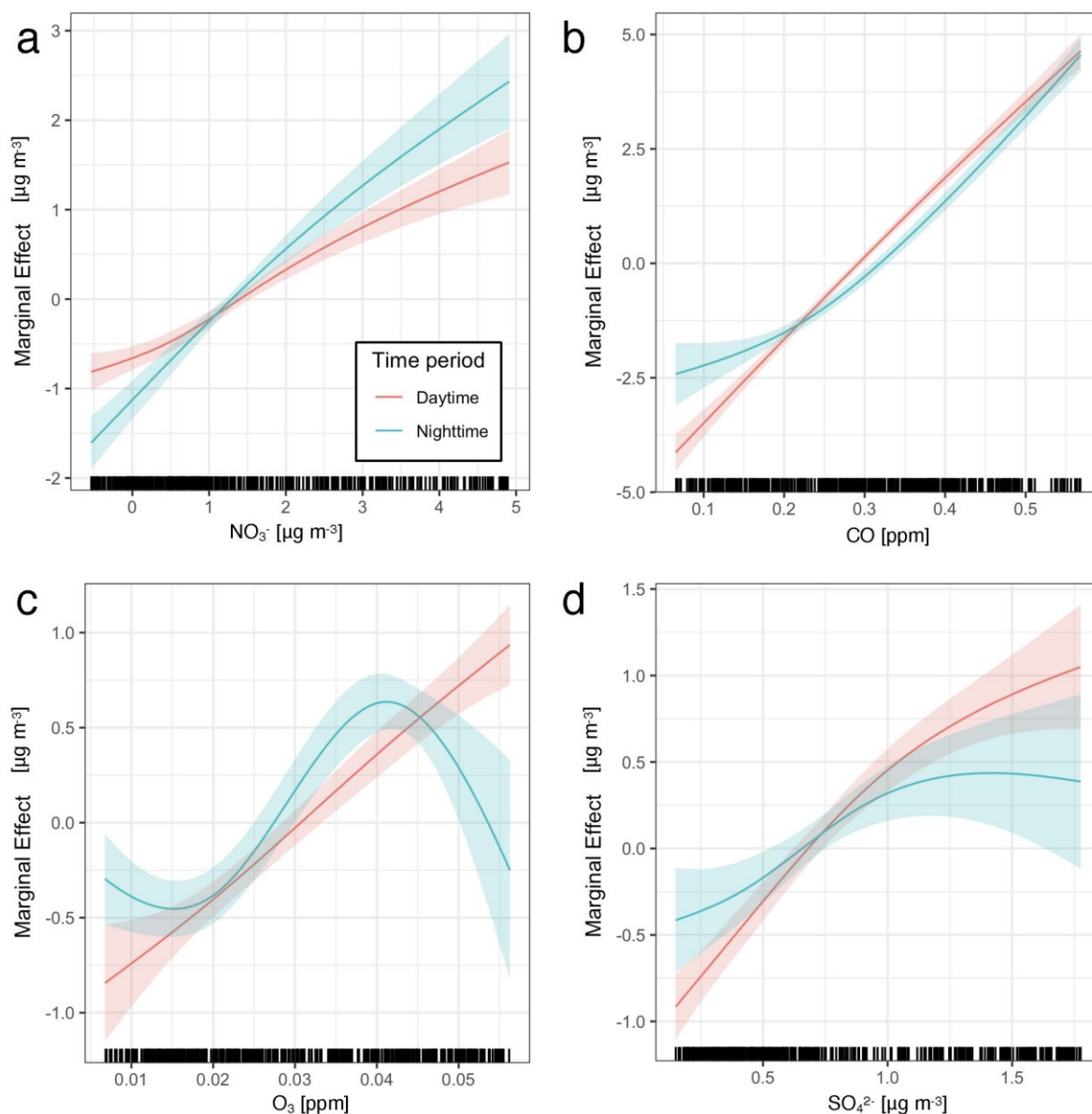


Figure 3.33. Marginal effects of (a)  $\text{NO}_3^-$ , (b) CO, (c)  $\text{O}_3$ , and (d)  $\text{SO}_4^{2-}$  for the Riverside (Mar) denoised model with 95% confidence intervals shaded.

To investigate short-term fluctuations, we remove the rolling 24-hour and diurnal signals. Immediately, we see that these fluctuations require a wider set of covariates to balance explanatory power with parsimony. As before,  $\text{SO}_4^{2-}$ ,  $\text{NO}_3^-$ ,  $\text{NO}_x$ , CO, and  $\text{O}_3$  all contribute significant explanatory power, but now the mass fractions of m/z 43 and m/z 44 are included (Figure 4.7). The covariates common to both models are explained by the same logic, while  $f_{43}$  and  $f_{44}$  shed additional light on the chemistry taking place. We see  $f_{43}$  display a positive association with its nighttime marginal effect and no effect during the day. This indicates that the  $f_{43}$  effect we see is not related to m/z 43 associated with HOA, as HOA is related to mobile emissions and would therefore confer daytime importance, but may instead be related to

LO-OOA, which also has a strong  $m/z$  43 peak in its mass spectrum. This is indicative of particle aging, which also explains why  $f_{44}$  has significant explanatory power, since the  $m/z$  44 peak is also present in LO-OOA and is especially strong in MO-OOA. The negative association we see for the marginal effects of  $f_{44}$  are likely because OOA is anticorrelated with OA, attaining its maximum in the afternoon between rush hours.

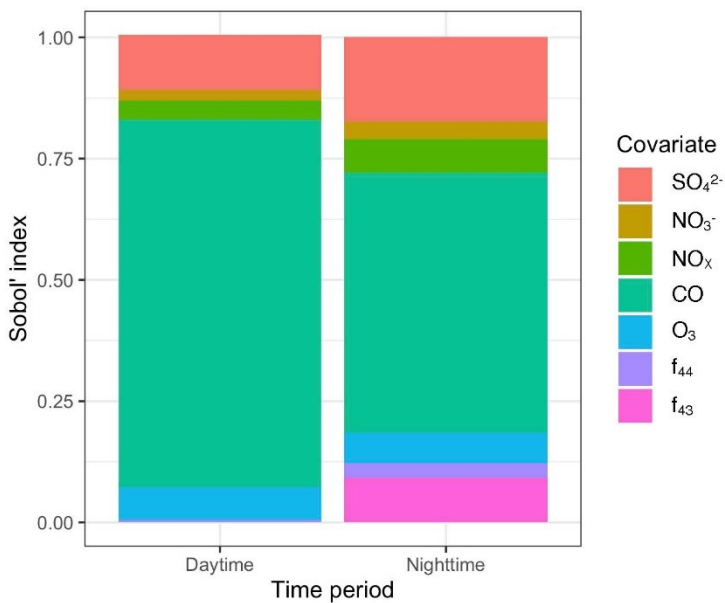


Figure 3.34. Sensitivity analysis for the Riverside (Mar) detrended model.

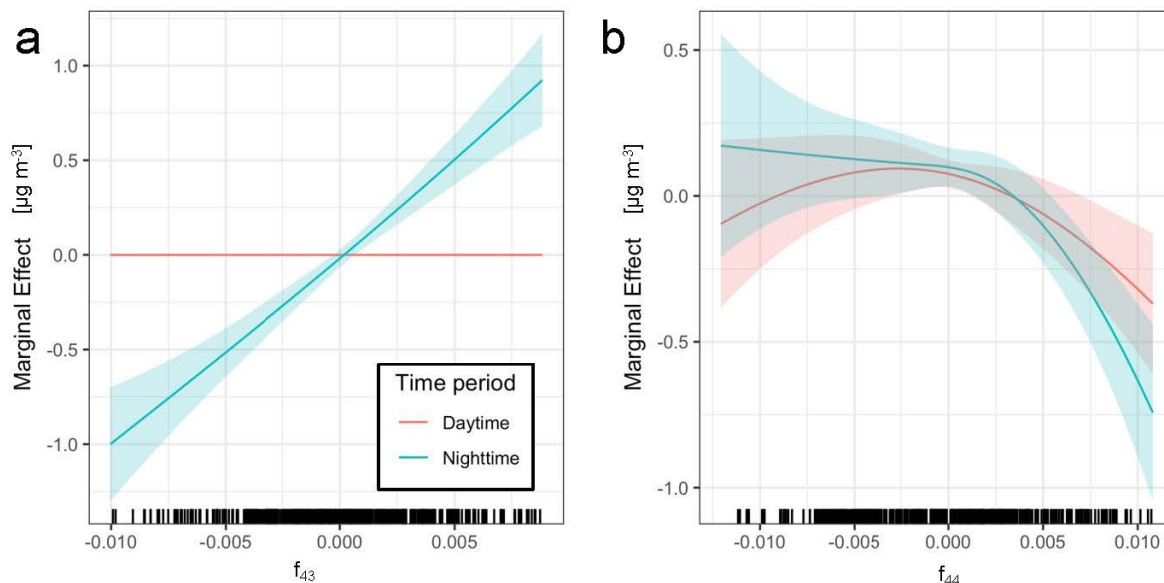


Figure 3.35. Marginal effects of (a)  $f_{43}$  and (b)  $f_{44}$  for the Riverside (Mar) detrended model with 95% confidence intervals shaded. Note: negative covariate values due to detrending.

#### 4.2.5 Riverside (Oct)

Like during Riverside (Mar),  $\text{SO}_4^{2-}$  and CO contribute explanatory power to the model trained on rolling 24-hour trends and diurnal periodicity, but unlike that campaign, meteorological covariates (wind speed, wind direction, and RH) provide additional explanatory power; we also see  $f_{43}$  selected (Figure 4.9).  $\text{SO}_4^{2-}$ , CO, and  $f_{43}$  all display positive associations in their marginal effects (Figure 4.10).  $\text{SO}_4^{2-}$  is likely due to a mixture of inflow and acid-catalyzed SOA formation (Gao et al. 2004; Jang et al. 2002; Mysliwiec and Kleeman 2002). Although  $\text{NO}_x$  was not a statistically significant explanatory covariate, CO is still strongly correlated with it ( $r = 0.85$ ), indicating mobile sources for CO. HOA is also strongly influenced by mobile sources and its strong  $m/z$  43 peak helps explain the positive association in the marginal effects for  $f_{43}$ , but BSOA is also characterized by a strong mass spectrum peak at  $m/z$  43 and constitutes a larger fraction of OA mass throughout the campaign. This suggests that high OA loadings are associated with high BSOA and/or HOA mass fractions.

RH displays a negative daytime association and a concave down nighttime association in its marginal effects (Figure 4.10). This is likely because RH and OA are anticorrelated, with OA higher during the day than overnight and the inverse for RH. Wind speed displays a positive association in its marginal effects (Figure 4.11), indicating the importance of transport as high wind speeds would display a negative association if ventilation were the only role they played. The marginal effects of wind speed indicate that westerly to east-north-easterly winds suppress OA while southerly to westerly winds enhance OA, with westerly winds, as the predominant wind direction, producing no effect relative to the mean.

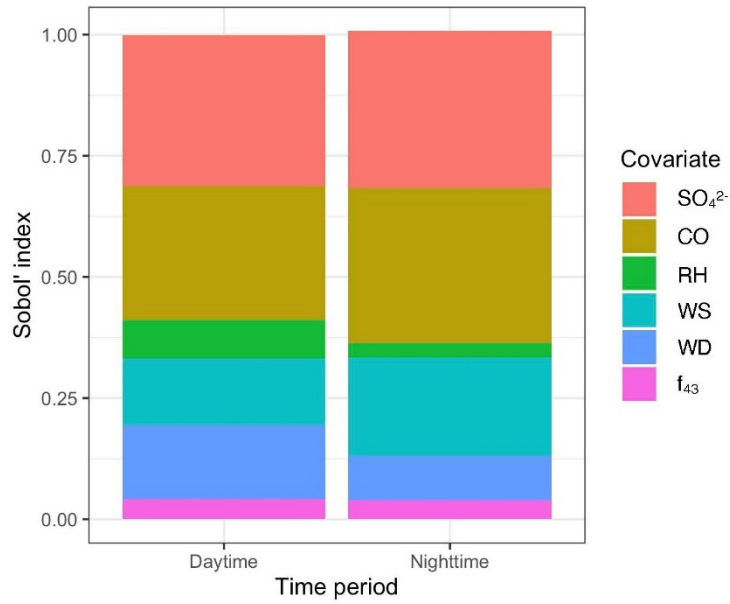


Figure 3.36. Sensitivity analysis for the Riverside (Oct) denoised model.

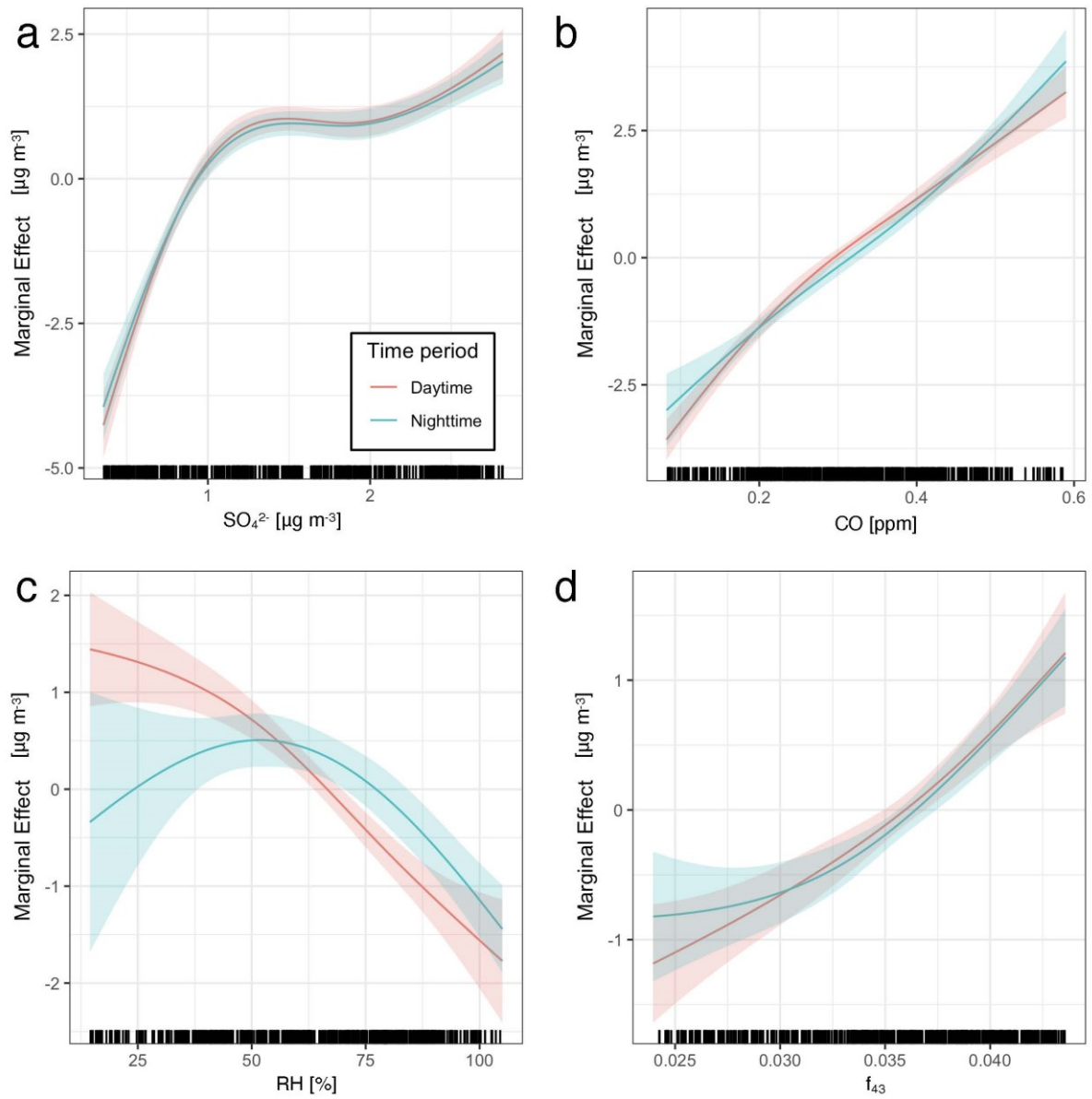


Figure 3.37. Marginal effects of (a)  $\text{SO}_4^{2-}$ , (b) CO, (c) RH, and (d)  $f_{43}$  for the Riverside (Oct) denoised model with 95% confidence intervals shaded.

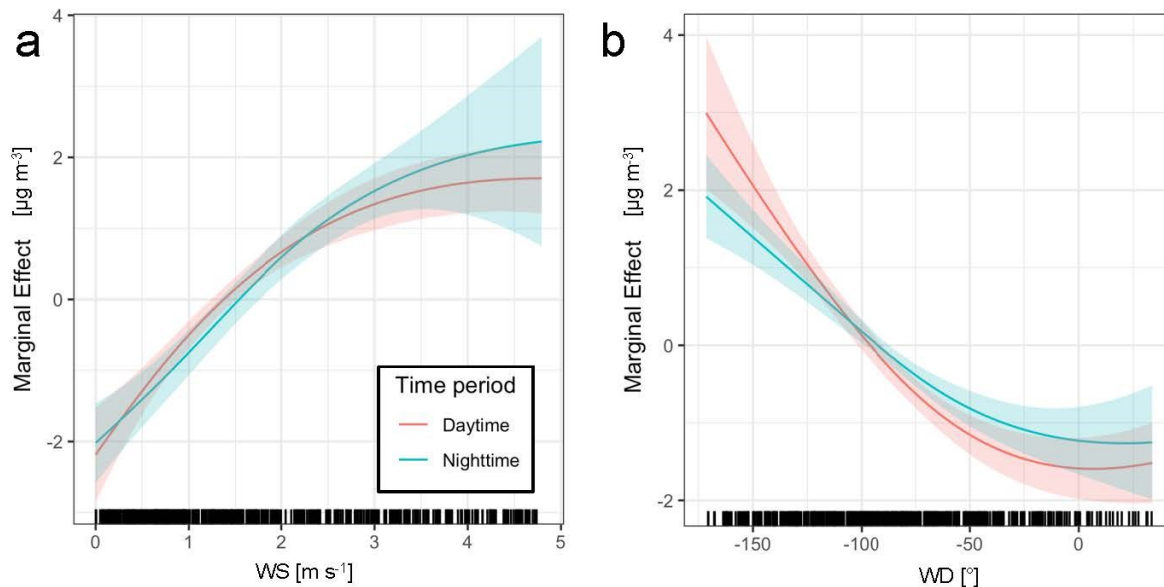


Figure 3.38. Marginal effects of (a) wind speed and (b) wind direction for the Riverside (Oct) denoised model with 95% confidence intervals shaded.

The covariates at our disposal for this campaign are insufficient to adequately explain short-term fluctuations ( $R^2 = 0.50$ ), so we focus on the preceding analysis of rolling 24-hour and diurnal trends.

#### 4.2.6 Wilmington (Mar)

As in the Riverside campaigns, OA in Wilmington during this campaign is best characterized by a covariate set that includes  $\text{NO}_3^-$  and CO. Alongside  $\text{O}_3$  and  $f_{43}$ , which were also important in the Riverside campaigns, temperature appears as a significant explanatory variable. With the exception of  $f_{43}$ , each selected covariate displays positive associations in its marginal effects (Figures 4.12-4.13).  $\text{NO}_3^-$ , as before, is due to the large fraction of  $\text{NO}_3^-$  that is organic (0.67), while CO is a tracer for mobile POA and SOA precursor emissions and  $\text{O}_3$  is a tracer for photochemical activity and OA oxidation through ozonolysis. Temperature most likely displays positive associations in its marginal effects because it is a proxy for insolation, which drives photochemical activity that enhances ozonolysis and thus SOA. In contrast, the marginal effects for  $f_{43}$  display negative associations. This is most likely because  $f_{43}$  anticorrelates with OA, since the mass fractions for HOA and OOA, which have substantial  $m/z$  43 peaks, grow when total OA decreases.

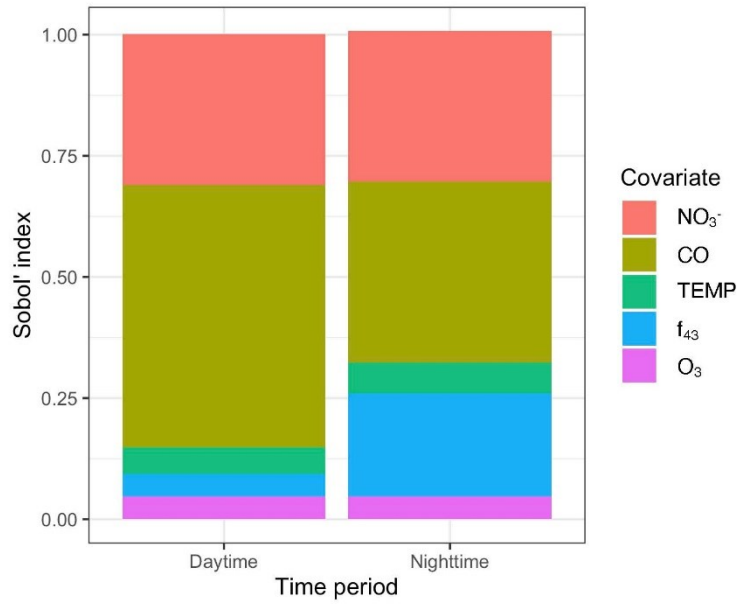


Figure 3.39. Sensitivity analysis for the Wilmington (Mar) denoised model.

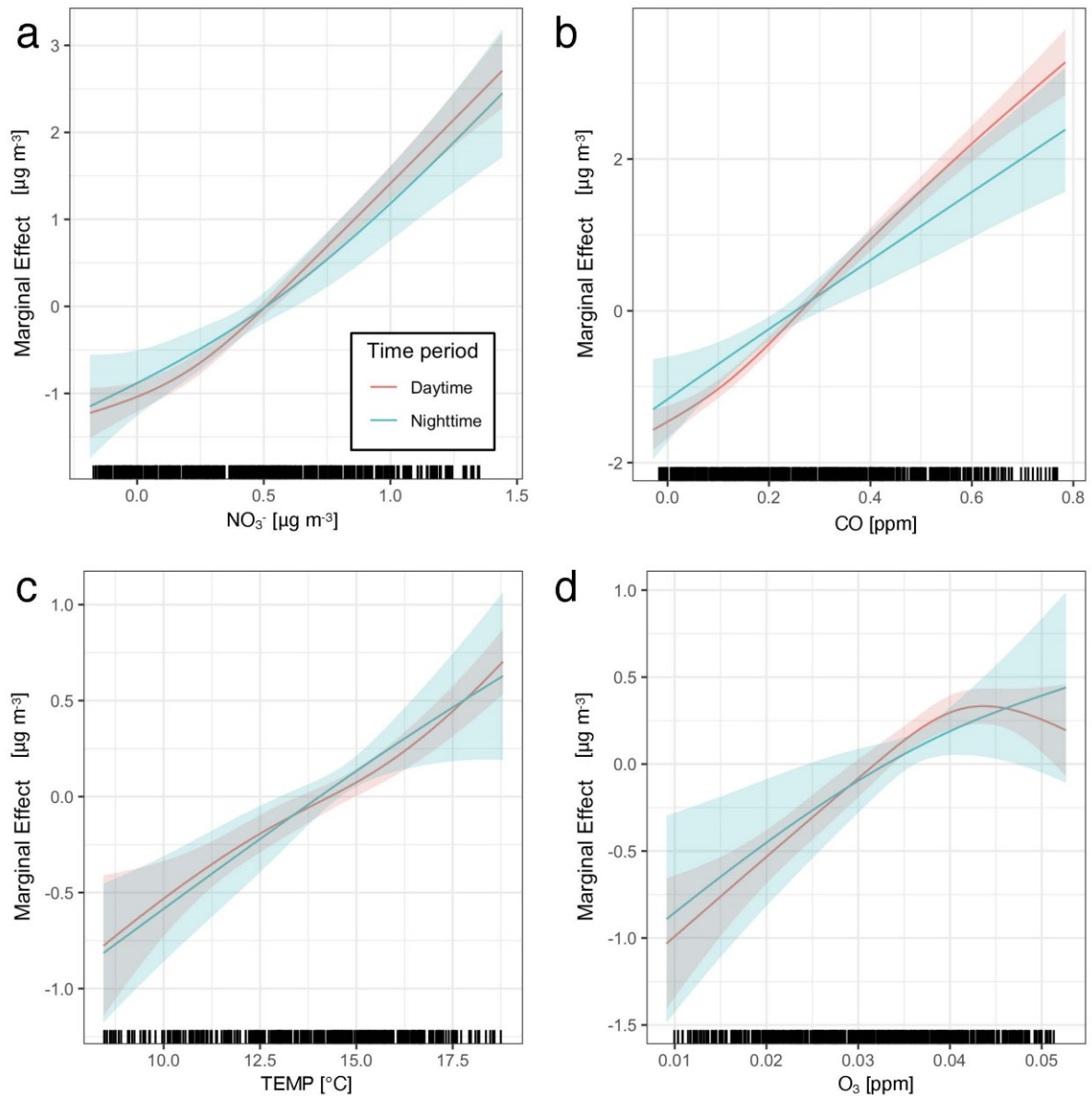


Figure 3.40. Marginal effects of (a)  $\text{NO}_3^-$ , (b) CO, (c) temperature, and (d)  $\text{O}_3$  for the Wilmington (Mar) denoised model with 95% confidence intervals shaded.

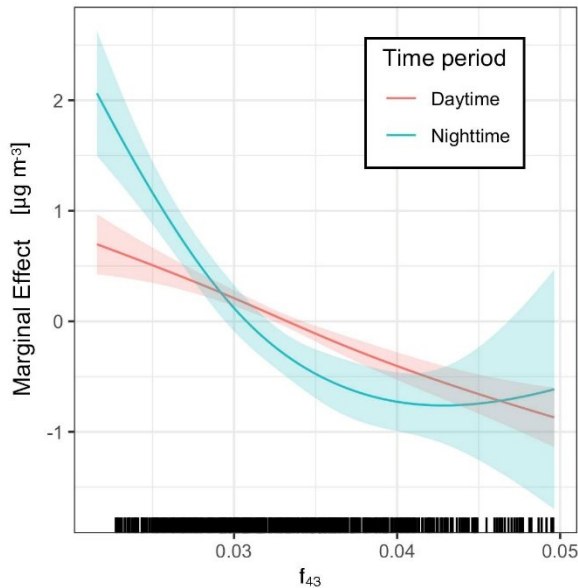


Figure 3.41. Marginal effects of  $f_{43}$  for the Wilmington (Mar) denoised model with 95% confidence intervals shaded.

As in Riverside in March, short-term fluctuations are not as well explained by our data, but most of the variance ( $R^2 = 0.66$ ) is accounted for, this time by  $\text{SO}_4^{2-}$ ,  $\text{NO}_3^-$ ,  $\text{Cl}^-$ ,  $\text{CO}$ ,  $\text{O}_3$ ,  $f_{44}$ , and wind direction (Figure 4.14). The relative importances of  $\text{NO}_3^-$  and  $\text{CO}$  flip compared to the denoised model, with  $\text{NO}_3^-$  now more important than  $\text{CO}$ , perhaps suggesting secondary  $\text{NO}_3^-$  processes are more important than mobile source POA and SOA precursors for short-term fluctuations. The inclusion of  $\text{Cl}^-$  is indicative of fresh sea salt influence, which together with its marginal effects (Figure 4.15) suggests  $\text{Cl}^-$  is acting to enhance OA. This can be explained by the mechanisms described by Cai and Griffin (2003) or Laskin et al. (2012), which describe how organic coatings on sea salt particles can enhance VOC uptake and therefore OA mass. The importance of wind direction corroborates this, as onshore versus offshore winds would modulate the influence of  $\text{Cl}^-$ . Since  $\text{SO}_4^{2-}$  in the Los Angeles basin is largely marine  $\text{SO}_4^{2-}$  (Mysliwiec and Kleeman 2002), wind direction modulates the influence of  $\text{SO}_4^{2-}$  in the same way.  $\text{SO}_4^{2-}$  itself, in this case, likely exerts its influence through acid-catalyzed SOA formation rather than co-transport as is the case in Riverside, since the main species that would be co-transported into Wilmington with  $\text{SO}_4^{2-}$  is  $\text{Cl}^-$  from sea salt aerosol rather than upwind OA, although there could feasibly be some amount of marine OA co-transported with  $\text{SO}_4^{2-}$ .  $\text{O}_3$  only displays a significant marginal effect during the daytime and exhibits a plateau before a positive association forms at higher  $\text{O}_3$  concentrations. Because  $f_{44}$  displays negative associations in its marginal effects, the positive association of  $\text{O}_3$  is less likely to be related to SOA formation through ozonolysis since this would form more OOA with  $m/z$  44 peaks and thus produce positive associations for  $f_{44}$  marginal effects. Instead, given the simultaneous importance of  $\text{Cl}^-$  and  $\text{NO}_3^-$ , the  $\text{O}_3$  marginal effect may be related to gas-phase chlorine-organic reactions.  $\text{Cl}^-$  displacement by  $\text{NO}_3^-$  generates  $\text{Cl}$  gas that can react with organic gases to generate alkyl and alkylperoxy radicals that form  $\text{O}_3$  in the presence of  $\text{NO}_x$  (Finlayson-Pitts, 2003). In this scenario, as  $\text{Cl}^-$  and  $\text{NO}_3^-$

form Cl gas, concentrations of organic radicals increase. These radicals produce  $\text{NO}_2$  that reacts with VOCs to form  $\text{O}_3$  and can continue reacting to form SOA. In this way,  $\text{O}_3$  becomes positively associated with OA.

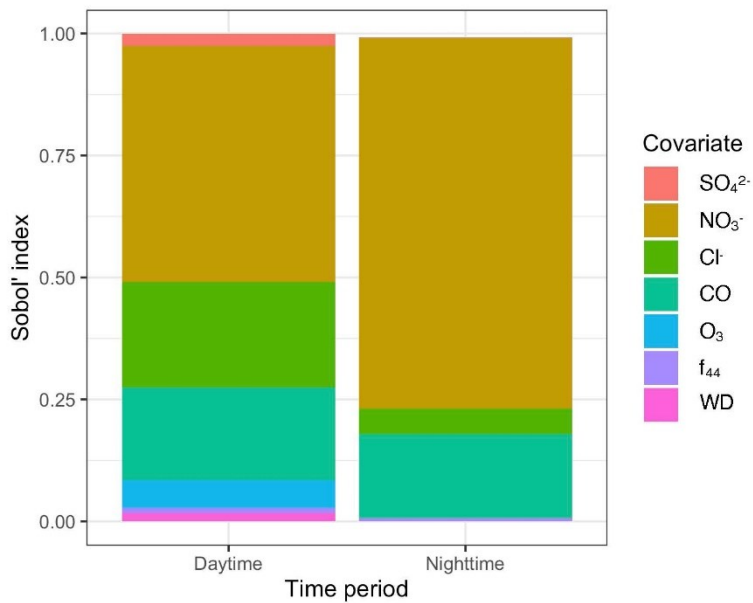


Figure 3.42. Sensitivity analysis for the Wilmington (Mar) detrended model.

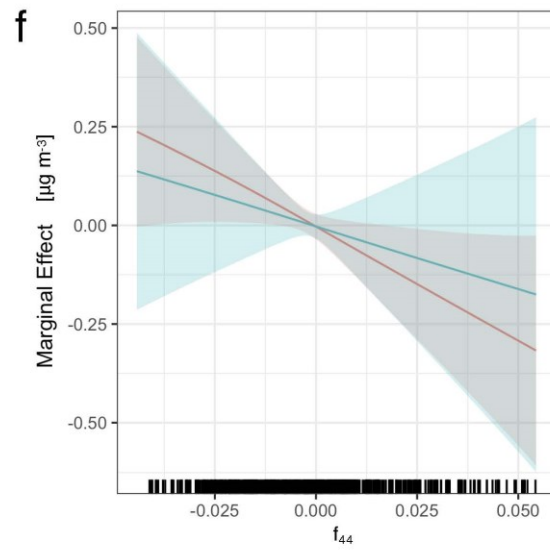
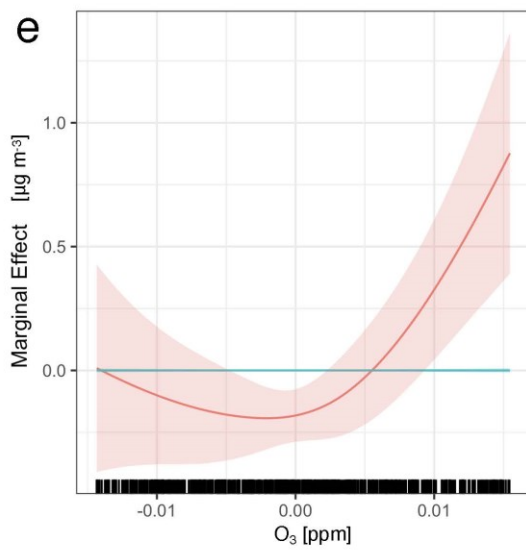
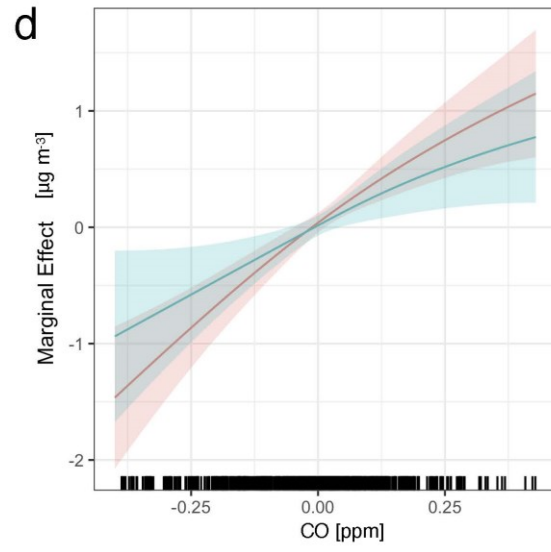
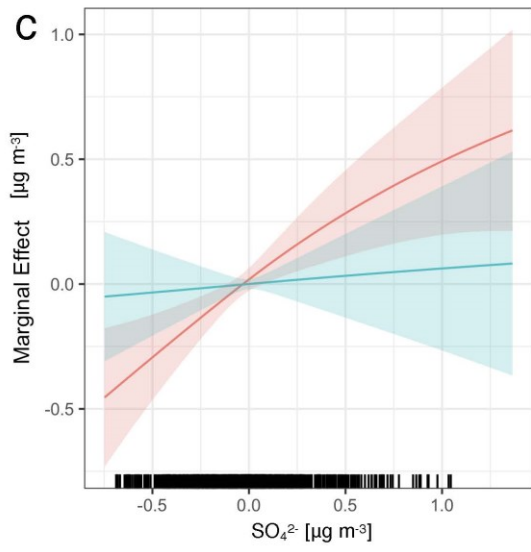
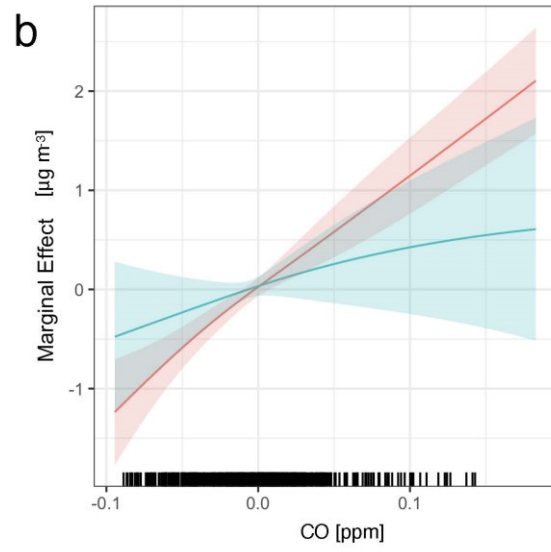
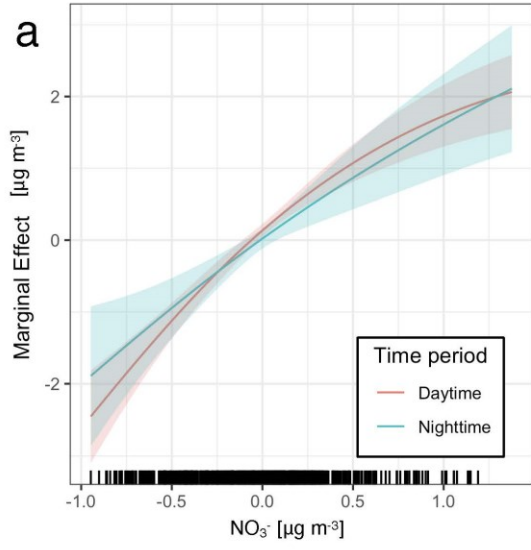


Figure 3.43. Marginal effects of (a)  $\text{NO}_3^-$ , (b)  $\text{Cl}^-$ , (c)  $\text{SO}_4^{2-}$ , (d)  $\text{CO}$ , (e)  $\text{O}_3$ , and (f)  $f_{44}$  for the Wilmington (Mar) detrended model with 95% confidence intervals shaded. Note: negative covariate values due to detrending.

#### 4.2.7 Bakersfield (Apr)

In this campaign, as in the others, Figure 4.17 shows that  $\text{NO}_3^-$ ,  $\text{SO}_4^{2-}$ , and  $\text{CO}$  are selected for their explanatory power, but although this is not the first campaign to include temperature as a significant covariate, OA sensitivity to temperature is greater than in Wilmington (Mar). In contrast to Riverside and Wilmington, where roughly two-thirds of  $\text{NO}_3^-$  was organic during Riverside (Mar) through Wilmington (Mar), only 49% of  $\text{NO}_3^-$  is organic in Bakersfield during this campaign. The positive associations in the marginal effects of both  $\text{NO}_3^-$  and  $\text{SO}_4^{2-}$  (Figure 4.18) may be related. Rollins et al. (2013) find that the nitrate functional group alone accounted for 4.8% of OA mass during the 2010 CalNex campaign and that isoprene and monoterpene oxidation in the presence of acidic  $\text{SO}_4^{2-}$  seed formed nitrooxy organosulfates. The correlation between  $\text{NO}_3^-$  and  $\text{SO}_4^{2-}$  ( $r = 0.60$ ) supports this, and could conceivably be higher between specifically organic nitrate and organic sulfate, but organic and inorganic sulfate is indistinguishable by AMS (Farmer et al., 2010).

The diurnal profile of  $\text{CO}$  shows strong rush hour peaks, as does  $\text{NO}_x$ , suggesting  $\text{CO}$  is a tracer for mobile source POA and SOA precursors, which explains the positive associations in its marginal effects (Figure 4.18). The importance of  $\text{Cl}^-$  is surprising since it accounts for just 1% of total AMS mass on average during the campaign. It is not immediately clear why  $\text{Cl}^-$  exhibits explanatory power for OA during this campaign. One possible explanation is related to biomass burning, but biomass burning aerosol is not identified by PMF as a major component of OA during this campaign. Mechanistically, wildland and agricultural fires can release potassium chloride ( $\text{KCl}$ ), then  $\text{NO}_3^-$  and  $\text{SO}_4^{2-}$  can deplete  $\text{Cl}^-$  by displacing it from  $\text{K}^+$  and forcing it into gas-phase chlorine species (Schlosser et al., 2017). This would explain the negative associations in the marginal effects of  $\text{Cl}^-$  (Figure 4.18), since biomass burning would enhance OA as  $\text{NO}_3^-$  and  $\text{SO}_4^{2-}$  deplete  $\text{Cl}^-$ .

Temperature displays positive associations in its marginal effects (Figure 4.18). Physically, higher temperatures generally reduce OA mass by enhancing VOC evaporation out of the particle phase. This discrepancy suggests an indirect relationship with temperature that overrides the importance of evaporation. This is explained by the temperature dependence of emissions of BVOCs like isoprene (Tingey et al., 1979). Since BVOC emissions increase with temperature and PMF shows that BSOA makes up a large fraction of OA during this campaign, the positive associations in the marginal effects of temperature is likely related to BSOA formation. Wind direction, ranging from  $-100^\circ$  to  $+100^\circ$  from north in our data, suggests that westerly winds (near  $-90^\circ$ ) reduce OA while easterly winds (near  $+90^\circ$ ) enhance OA. This is surprising since the actual measurement site is located east of Bakersfield, leading to the expectation that westerly winds would bring polluted air from the city. One possible explanation is that the Bena Landfill lies due east of the measurement site, which may also help explain the role of chloride since landfills are significant chlorine emitters as well as VOC emitters (Bannan et al., 2019).

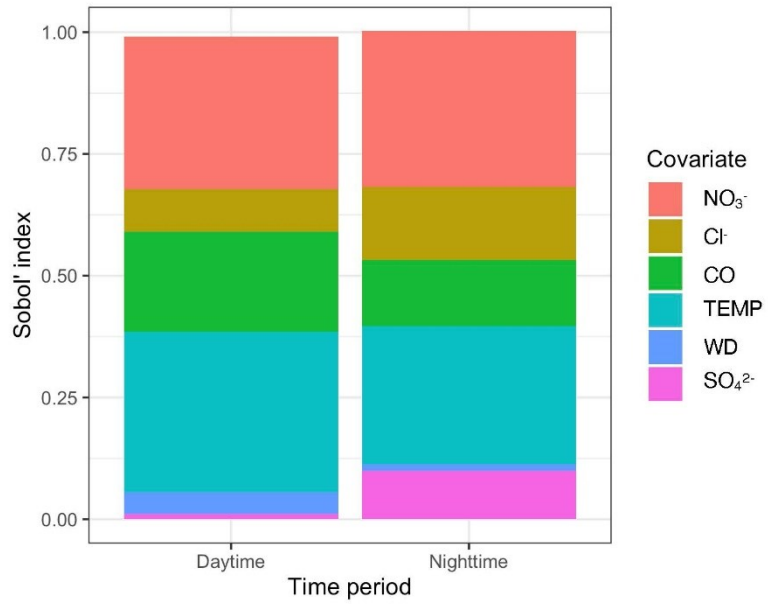


Figure 3.44. Figure 4.17. Sensitivity analysis for the Bakersfield (Apr) denoised model.

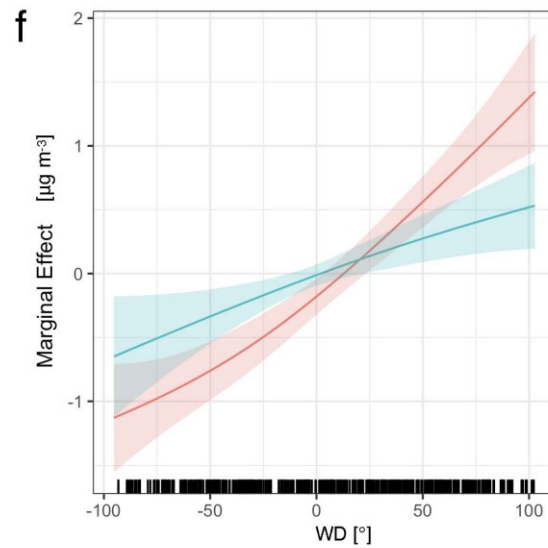
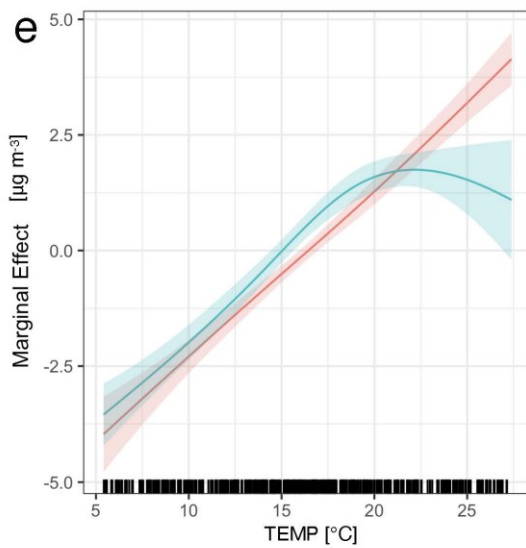
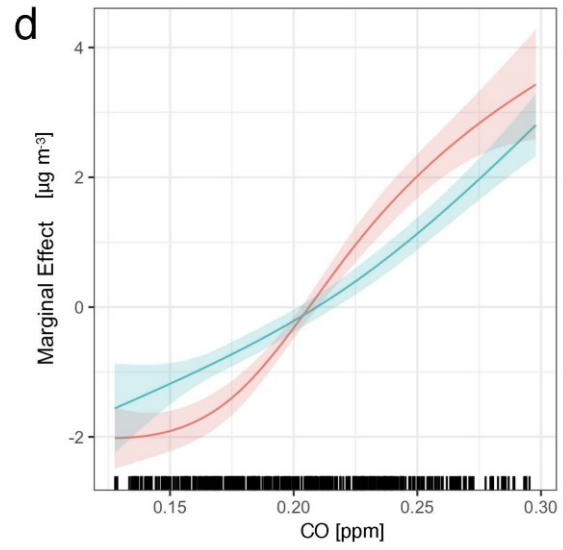
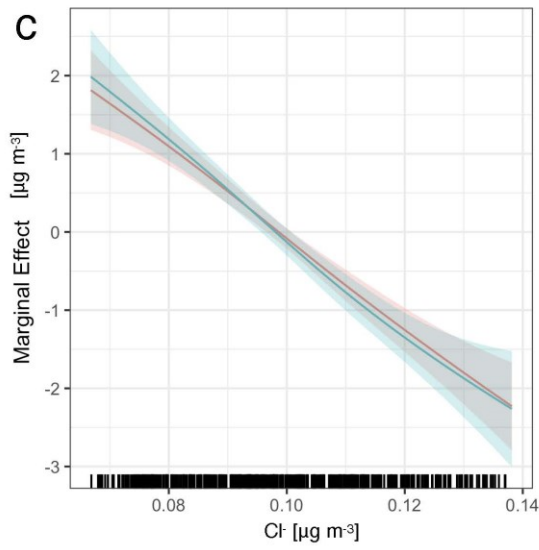
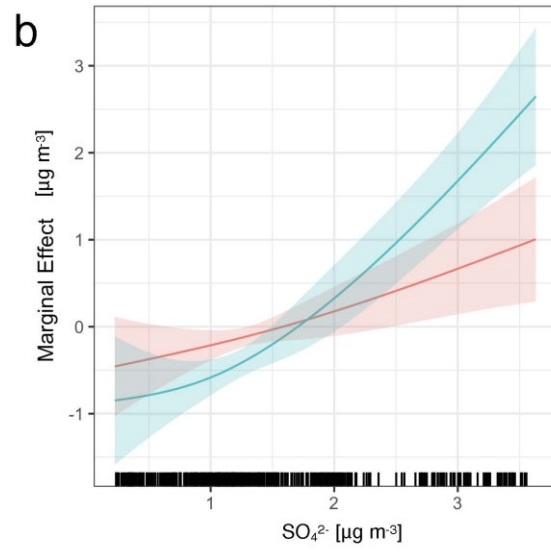
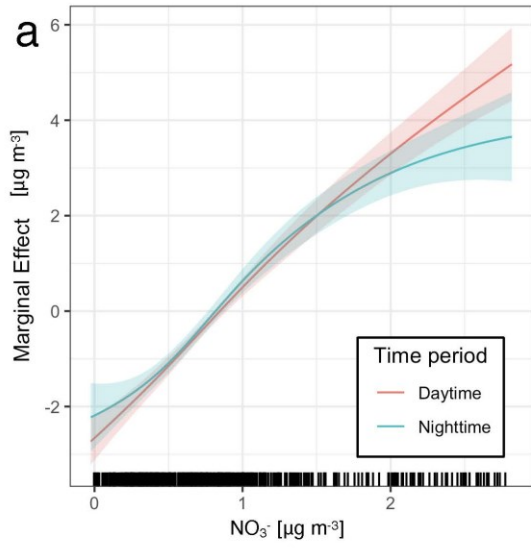


Figure 3.45. Marginal effects of (a)  $\text{NO}_3^-$ , (b)  $\text{SO}_4^{2-}$ , (c)  $\text{Cl}^-$ , (d)  $\text{CO}$ , (e) temperature, and (f) wind direction for the Bakersfield (Apr) denoised model with 95% confidence intervals shaded.

As in Riverside in October, our data for this campaign do not adequately explain short-term fluctuations ( $R^2 = 0.42$ ), so we focus on the preceding analysis of rolling 24-hour and diurnal trends.

#### 4.2.8 Summary

Generalized additive modeling combined with sensitivity analysis elucidates the relationships between OA covariates and their relative importances for driving OA levels. Marginal effects derived from GAMs enable predicting the individual impacts of changes in individual covariates, while sensitivity analysis allows for the ranking of covariates by the strength of their influence on OA variability. Together, these results help us understand the formation regimes of OA in California, which can help inform how to target controllable covariates for efficient OA reductions.

By contextualizing marginal effects within the literature, this analysis helps attribute marginal effects to physical mechanisms or infer likely correlations where marginal effects do not admit physical explanations. This furthers our understanding of OA regimes by revealing where interactions between covariates confound OA behavior, highlighting the nontrivial nature of OA.

In Riverside in March, OA is most strongly associated with covariates related to mobile emissions, like  $\text{CO}$  and secondary  $\text{NO}_3^-$ . In October, Riverside sees a stronger influence from upwind sources relative to March, but mobile emissions still contribute substantial explanatory power for OA behavior. This suggests the importance of reducing mobile emissions to address POA contributions to overall OA in Riverside, while the influence of OOA implies that controlling SOA formation may also alleviate overall OA levels. Our results show that OA in Riverside is associated with  $\text{SO}_4^{2-}$ , suggesting the role of acid-catalyzed SOA formation. This implies reducing anthropogenic sulfur emissions upwind of Riverside may support OA reductions in Riverside, although not all upwind sulfur is anthropogenic. Conclusions are similar for Wilmington in March, with the additional point that  $\text{O}_3$  shows an association with OA such that  $\text{O}_3$  controls may have the co-benefit of alleviating OA levels there. For OA in Bakersfield, there remains a strong association with covariates related to mobile emissions, but there is also a stronger biogenic influence. Additionally, the unusual influence of  $\text{Cl}^-$  in conjunction with the influence of wind direction may suggest the importance of upwind landfill emissions. Together, these observations suggest that mobile emissions may alleviate OA in Bakersfield like in Riverside and Wilmington, but also that additional site-specific control strategies that regulate specific point sources may support OA reductions. These results imply the importance of targeted measurement and monitoring to reveal and disentangle the unique local conditions that vary across California. OA responds with varying strength to the same covariates at different locations, with some locations sensitive to covariates that exert little influential elsewhere, like  $\text{SO}_4^{2-}$  in Riverside and Bakersfield versus Wilmington, or  $\text{Cl}^-$  in Bakersfield versus Riverside and Wilmington.

With hourly time resolution, this Task's generalized additive modeling resolves features that Task 1 could not. Temporal disaggregation into separate night and day model fits sheds light on how OA can behave differently between nighttime and daytime. Denoising to separate trends and diurnal cycles from short-term fluctuations facilitates robust model fits that characterize general OA behavior well, while short-term

fluctuations are in some cases reasonably well characterized and in others not well characterized. This reflects the importance of rich, high-resolution data sets for capturing the complex dynamics of OA.

## References

- 40 CFR 58.12 -- Operating schedules. [WWW Document], n.d. URL <https://www.ecfr.gov/current/title-40/chapter-I/subchapter-C/part-58/subpart-B/section-58.12> (accessed 8.16.22).
- Ackermann-Liebrich, U., Leuenberger, P., Schwartz, J., Schindler, C., Monn, C., Bolognini, G., Bongard, J.P., Brändli, O., Domenighetti, G., Elsasser, S., Grize, L., Karrer, W., Keller, R., Keller-Wossidlo, H., Künzli, N., Martin, B.W., Medici, T.C., Perruchoud, A.P., Schöni, M.H., Tschopp, J.M., Villiger, B., Wüthrich, B., Zellweger, J.P., Zemp, E., 1997. Lung function and long term exposure to air pollutants in Switzerland. Study on Air Pollution and Lung Diseases in Adults (SAPALDIA) Team. *Am J Respir Crit Care Med* 155, 122–129. <https://doi.org/10.1164/ajrccm.155.1.9001300>
- Aldrin, M., Haff, I., 2005. Generalised additive modelling of air pollution, traffic volume and meteorology. *Atmospheric Environment* 39, 2145–2155. <https://doi.org/10.1016/j.atmosenv.2004.12.020>
- Alduchov, O.A., Eskridge, R.E., 1997. Improved Magnus` form approximation of saturation vapor pressure (No. DOE/ER/61011--T6, 548871). <https://doi.org/10.2172/548871>
- Allan, J.D., A.E.Delia, Coe, H., Bower, K.N., Alfarra, M.R., Jimenez, J.L., Middlebrook, A.M., Drewnick, F., Onasch, T.B., Canagaratna, M.R., Jayne, J.T., Worsnop, D.R., 2004. A generalized method for the extraction of chemically resolved mass spectra from aerodyne aerosol mass spectrometer data. *J. Aerosol Science* 35, 909–922.
- Allan, J.D., Jimenez, J.L., Coe, H., Bower, K.N., Williams, P.I., Worsnop, D.R., 2003. Quantitative sampling using an Aerodyne Aerosol Mass Spectrometer. Part 1: Techniques of data interpretation and error analysis. *J. Geophys. Res.* 108, 4090, doi:10.1029/2002JD002358.
- Allan, J.D., Williams, P.I., Morgan, W.T., Martin, C.L., Flynn, M.J., Lee, J., Nemitz, E., Phillips, G.J., Gallagher, M.W., Coe, H., 2010. Contributions from transport, solid fuel burning and cooking to primary organic aerosols in two UK cities. *Atmospheric Chemistry and Physics* 10, 647–668. <https://doi.org/10.5194/acp-10-647-2010>
- AQ Query Tool [WWW Document], n.d. URL <https://www.arb.ca.gov/aqmis2/aqdselect.php> (accessed 8.16.22).
- ARB Almanac 2013, n.d.
- ARB Almanac 2013 - Chapter 4: Regional Trends and Forecasts, n.d.
- Area Designation Maps [WWW Document], n.d. . California Air Resources Board. URL <https://ww2.arb.ca.gov/resources/documents/maps-state-and-federal-area-designations> (accessed 8.9.22).
- Atkinson, R.W., Ross Anderson, H., Sunyer, J., Ayres, J., Baccini, M., Vonk, J.M., Boumghar, A., Forastiere, F., Forsberg, B., Touloumi, G., Schwartz, J., Katsouyanni, K., 2001. Acute Effects of Particulate Air Pollution on Respiratory Admissions: Results from APHEA 2 Project. *Am J Respir Crit Care Med* 164, 1860–1866. <https://doi.org/10.1164/ajrccm.164.10.2010138>
- Bahreini, R., Ervens, B., Middlebrook, A.M., Warneke, C., Gouw, J.A. de, DeCarlo, P.F., Jimenez, J.L., Atlas, E., Brioude, J., Brock, C.A., Fried, A., Holloway, J.S., Peischl, J., Richter, D., Ryerson, T.B., Stark, H., Walega, J., Weibring, P., Wollny, A.G., Fehsenfeld, F.C., 2009. Organic aerosol formation

- in urban and industrial plumes near Houston and Dallas, TX. *J. Geophys. Res.* 114. <https://doi.org/10.1029/2008JD011493>
- Bahreini, R., Jimenez, J.L., Wang, J., Flagan, R.C., Seinfeld, J.H., Jayne, J.T., Worsnop, D.R., 2003. Aircraft-based aerosol size and composition measurements during ACE-Asia using an Aerodyne aerosol mass spectrometer. *J. Geophys. Res.* 108, 8645, doi:10.1029/2002JD003226.
- Bahreini, R., Middlebrook, A.M., Brock, C.A., de Gouw, J.A., McKeen, S.A., Williams, L.R., Daumit, K.E., Lambe, A.T., Massoli, P., Canagaratna, M.R., Ahmadov, R., Carrasquillo, A.J., Cross, E.S., Ervens, B., Holloway, J.S., Hunter, J.F., Onasch, T.B., Pollack, I.B., Roberts, J.M., Ryerson, T.B., Warneke, C., Davidovits, P., Worsnop, D.R., Kroll, J.H., 2012. Mass Spectral Analysis of Organic Aerosol Formed Downwind of the Deepwater Horizon Oil Spill: Field Studies and Laboratory Confirmations. *Environ. Sci. Technol.* 46, 8025–8034. <https://doi.org/10.1021/es301691k>
- Bannan, T.J., Khan, M.A.H., Le Breton, M., Priestley, M., Worrall, S.D., Bacak, A., Marsden, N.A., Lowe, D., Pitt, J., Allen, G., Topping, D., Coe, H., McFiggans, G., Shallcross, D.E., Percival, C.J., 2019. A Large Source of Atomic Chlorine From ClNO<sub>2</sub> Photolysis at a U.K. Landfill Site. *Geophysical Research Letters* 46, 8508–8516. <https://doi.org/10.1029/2019GL083764>
- Blanchard, C.L., Shaw, S.L., Edgerton, E.S., Schwab, J.J., 2019. Emission influences on air pollutant concentrations in New York State: I. ozone. *Atmospheric Environment: X* 3, 100033. <https://doi.org/10.1016/j.aeaoa.2019.100033>
- Cai, X., Griffin, R.J., 2003. Modeling the formation of secondary organic aerosol in coastal areas: Role of the sea-salt aerosol organic layer. *Journal of Geophysical Research: Atmospheres* 108. <https://doi.org/10.1029/2002JD003053>
- Canagaratna, M.R., Jayne, J.T., Jimenez, J.L., Allan, J.D., Alfarra, M.R., Zhang, Q., Onasch, T.B., Drewnick, F., Coe, H., Middlebrook, A.M., Delia, A., Williams, L.R., Trimborn, A.M., Northway, M.J., DeCarlo, P.F., Kolb, C.E., Davidovits, P., Worsnop, D.R., 2007. Chemical and Microphysical Characterization of Ambient Aerosols with the Aerodyne Aerosol Mass Spectrometer. *Mass Spectrometry Reviews* 26, 185–222.
- Chen, C., Zhang, H., Yan, W., Wu, N., Zhang, Q., & He, K. (2021). Aerosol water content enhancement leads to changes in the major formation mechanisms of nitrate and secondary organic aerosols in winter over the North China Plain. *Environmental Pollution*, 287, 117625. <https://doi.org/10.1016/j.envpol.2021.117625>
- Chen, J., Lu, J., Avise, J.C., DaMassa, J.A., Kleeman, M.J., Kaduwela, A.P., 2014. Seasonal modeling of PM<sub>2.5</sub> in California's San Joaquin Valley. *Atmospheric Environment* 92, 182–190. <https://doi.org/10.1016/j.atmosenv.2014.04.030>
- Community Air Protection Program [WWW Document], n.d. . California Air Resources Board. URL <https://ww2.arb.ca.gov/capp/about>
- Cubison, M.J., Hayes, A.M.O.P.L., Farmer, D.K., Day, D., Lechner, M.J., Brune, W.H., Apel, E., Diskin, G.S., Fisher, J.A., Fuelberg, H.E., Hecobian, A., Knapp, D.J., Mikoviny, T., Riemer, D., Sachse, G.W., Sessions, W., Weber, R.J., Weinheimer, A.J., Wisthaler, A., Jimenez, J.L., 2011. Effects of aging on organic aerosol from open biomass burning smoke in aircraft and laboratory studies. *Atmos. Chem. Phys.* 11, 2049–12064. <https://doi.org/10.5194/acp-11-2049-2011>
- Day, D.A., Campuzano-Jost, P., Nault, B.A., Palm, B.B., Hu, W., Guo, H., Wooldridge, P.J., Cohen, R.C., Docherty, K.S., Huffman, J.A., de Sá, S.S., Martin, S.T., Jimenez, J.L., 2022. A systematic re-evaluation of methods for quantification of bulk particle-phase organic nitrates using real-time aerosol mass spectrometry. *Atmospheric Measurement Techniques* 15, 459–483. <https://doi.org/10.5194/amt-15-459-2022>

- DeCarlo, P.F., Dunlea, E.J., Kimmel, J.R., Aiken, A.C., Jimenez, J.L., 2008. Fast Airborne Aerosol Size and Chemistry Measurements with the High Resolution Aerosol Mass Spectrometer during the Milagro- Mex Field Campaign. *Atmos. Chem. Phys.* 8, 4027–4048.
- Dingle, J.H., Vu, K., Bahreini, R., Apel, E.C., Campos, T.L., Flocke, F., Fried, A., Herndon, S., Hills, A.J., Hornbrook, R.S., Huey, G., Kaser, L., Montzka, D.D., Nowak, J.B., Reeves, M., Richter, D., Roscioli, J.R., Shertz, S., Stell, M., Tanner, D., Tyndall, G., Walega, J., Weibring, P., Weinheimer, A., 2016. Aerosol Optical Extinction during the Front Range Air Pollution and Photochemistry Experiment (FRAPPÉ) 2014 Summertime Field Campaign, Colorado U.S.A. *Atmos. Chem. Phys.* 2016, 1–21. <https://doi.org/10.5194/acp-16-11207-2016>
- Dingle, J.H., Zimmerman, S., Min, J., Jung, H., Bahreini, R., 2019. Complex Refractive Index, Single Scattering Albedo, and Mass Absorption Coefficient of Secondary Organic Aerosols Generated from Oxidation of Biogenic and Anthropogenic Precursors. *Aerosol Sci. Technol.* <https://doi.org/10.1021/acs.estlett.9b00017>
- Dockery, D.W., Pope, C.A., Xu, X., Spengler, J.D., Ware, J.H., Fay, M.E., Ferris, B.G., Speizer, F.E., 1993. An Association between Air Pollution and Mortality in Six U.S. Cities. *N Engl J Med* 329, 1753–1759. <https://doi.org/10.1056/NEJM199312093292401>
- Enayati Ahangar, F., Pakbin, P., Hasheminassab, S., Epstein, S.A., Li, X., Polidori, A., Low, J., 2021. Long-term trends of PM<sub>2.5</sub> and its carbon content in the South Coast Air Basin: A focus on the impact of wildfires. *Atmospheric Environment* 255, 118431. <https://doi.org/10.1016/j.atmosenv.2021.118431>
- Fares, S., Park, J.-H., Gentner, D.R., Weber, R., Ormeño, E., Karlik, J., Goldstein, A.H., 2012. Seasonal cycles of biogenic volatile organic compound fluxes and concentrations in a California citrus orchard. *Atmospheric Chemistry and Physics* 12, 9865–9880. <https://doi.org/10.5194/acp-12-9865-2012>
- Farmer, D.K., Matsunaga, A., Docherty, K.S., Surratt, J.D., Seinfeld, J.H., Ziemann, P.Z., Jimenez, J.L., 2010. Response of an aerosol mass spectrometer to organonitrates and organosulfate and implications for atmospheric chemistry. *Proc. Natl. Acad. Sci. U. S. A.* 107. <https://doi.org/10.1073/pnas.0912340107>
- Feng, Z., Liu, Y., Zheng, F., Yan, C., Fu, P., Zhang, Y., Lian, C., Wang, W., Cai, J., Du, W., Chu, B., Wang, Y., Kangasluoma, J., Bianchi, F., Petäjä, T., & Kulmala, M. (2022). Highly oxidized organic aerosols in Beijing: Possible contribution of aqueous-phase chemistry. *Atmospheric Environment*, 273, 118971. <https://doi.org/10.1016/j.atmosenv.2022.118971>
- Ferretti, F., Saltelli, A., Tarantola, S., 2016. Trends in sensitivity analysis practice in the last decade. *Science of The Total Environment* 568, 666–670. <https://doi.org/10.1016/j.scitotenv.2016.02.133>
- Finlayson-Pitts, B.J., 2003. The Tropospheric Chemistry of Sea Salt: A Molecular-Level View of the Chemistry of NaCl and NaBr. *Chem. Rev.* 103, 4801–4822. <https://doi.org/10.1021/cr020653t>
- Fry, J.L., Draper, D.C., Zarzana, K.J., Campuzano-Jost, P., Day, D.A., Jimenez, J.L., Brown, S.S., Cohen, R.C., Kaser, L., Hansel, A., Cappellin, L., Karl, T., Roux, A.H., Turnipseed, A., Cantrell, C., Lefer, B.L., Grossberg, N., 2013. Observations of gas- and aerosol-phase organic nitrates at BEACHON-RoMBAS 2011. *Atmos. Chem. Phys.* 13. <https://doi.org/10.5194/acp-13-8585-2013>
- Gao, S., Ng, N.L., Keywood, M., Varutbangkul, V., Bahreini, R., Nenes, A., He, J., Yoo, K.Y., Flagan, R.C., Seinfeld, J.H., 2004. Particle phase acidity and oligomer formation in secondary organic aerosol. *Environ. Sci. Technol.* doi: 10.10.
- Gao, Z., Ivey, C.E., Blanchard, C.L., Do, K., Lee, S.-M., Russell, A.G., 2022. Separating emissions and meteorological impacts on peak ozone concentrations in Southern California using generalized

- additive modeling. *Environmental Pollution* 307, 119503.  
<https://doi.org/10.1016/j.envpol.2022.119503>
- Hafner, H.R., Penfold, B.M., 2018. PAMS Data Validation and Analysis Training Material.
- Halonen, J.I., Lanki, T., Yli-Tuomi, T., Kulmala, M., Tiittanen, P., Pekkanen, J., 2008. Urban air pollution, and asthma and COPD hospital emergency room visits. *Thorax* 63, 635–641.  
<https://doi.org/10.1136/thx.2007.091371>
- Hao, L., Kari, E., Leskinen, A., Worsnop, D.R., Virtanen, A., 2020. Direct contribution of ammonia to  $\alpha$ -pinene secondary organic aerosol formation. *Atmospheric Chemistry and Physics* 20, 14393–14405.  
<https://doi.org/10.5194/acp-20-14393-2020>
- Hastie, T., Tibshirani, R., 1986. Generalized Additive Models. *Statist. Sci.* 1, 297–310.  
<https://doi.org/10.1214/ss/1177013604>
- Hayes, P.L., Ortega, A.M., Cubison, M.J., Froyd, K.D., Zhao, Y., Cliff, S.S., Hu, W.W., Toohey, D.W., Flynn, J.H., Lefer, B.L., Grossberg, N., Alvarez, S., Rappenglueck, B., Taylor, J.W., Allan, J.D., Holloway, J.S., Gilman, J.B., Kuster, W.C., De Gouw, J.A., Massoli, P., Zhang, X., Liu, J., Weber, R.J., Corrigan, A.L., Russell, L.M., Isaacman, G., Worton, D.R., Kreisberg, N.M., Goldstein, A.H., Thalman, R., Waxman, E.M., Volkamer, R., Lin, Y.H., Surratt, J.D., Kleindienst, T.E., Offenberg, J.H., Dusanter, S., Griffith, S., Stevens, P.S., Brioude, J., Angevine, W.M., Jimenez, J.L., 2013. Organic aerosol composition and sources in Pasadena, California, during the 2010 CalNex campaign. *Journal of Geophysical Research-Atmospheres* 118, 9233–9257. <https://doi.org/10.1002/jgrd.50530>
- He, Q., Tomaz, S., Li, C., Zhu, M., Meidan, D., Riva, M., Laskin, A., Brown, S.S., George, C., Wang, X., Rudich, Y., 2021. Optical Properties of Secondary Organic Aerosol Produced by Nitrate Radical Oxidation of Biogenic Volatile Organic Compounds. *Environmental Science & Technology* 55, 2878–2889. <https://doi.org/10.1021/acs.est.0c06838>
- Hersey, S. P., J. S. Craven, K. A. Schilling, A. R. Metcalf, A. Sorooshian, M. N. Chan, R. C. Flagan, and J. H. Seinfeld. 2011. “The Pasadena Aerosol Characterization Observatory (PACO): Chemical and Physical Analysis of the Western Los Angeles Basin Aerosol.” *Atmospheric Chemistry and Physics* 11(15):7417–43. doi:10.5194/acp-11-7417-2011.
- Hettiyadura, A.P.S., Al-Naiema, I.M., Hughes, D.D., Fang, T., Stone, E.A., 2019. Organosulfates in Atlanta, Georgia: anthropogenic influences on biogenic secondary organic aerosol formation. *Atmospheric Chemistry and Physics* 19, 3191–3206. <https://doi.org/10.5194/acp-19-3191-2019>
- Ivey, C.E., Blanchard, C.L., Russell, A.G., Gao, Z., Do, K., 2022. Ozone Meteorology Study Final Report. For South Coast Air Quality Management District, Diamond Bar, CA.
- Jang, M., Czoschke, N.M., Lee, S., Kamens, R.M., 2002. Heterogeneous atmospheric aerosol production by acid-catalyzed particle-phase reactions. *Science* 298, 814–817.
- Jayne, J.T., Leard, D.C., Zhang, X., Davidovits, P., Smith, K.A., Kolb, C.E., Worsnop, D.W., 2000. Development of an Aerosol Mass Spectrometer for size and composition analysis of submicron particles. *Aerosol Science and Technology* 33, 49–70.
- Kang, E., Root, M.J., Toohey, D.W., Brune, W.H., 2007. Introducing the concept of Potential Aerosol Mass (PAM). *Atmos. Chem. Phys.* 7, 5727–5744.
- Laskin, A., Moffet, R.C., Gilles, M.K., Fast, J.D., Zaveri, R.A., Wang, B., Nigge, P., Shutthanandan, J., 2012. Tropospheric chemistry of internally mixed sea salt and organic particles: Surprising reactivity of NaCl with weak organic acids. *Journal of Geophysical Research: Atmospheres* 117.  
<https://doi.org/10.1029/2012JD017743>

- Liu, S., Ahlm, L., Day, D.A., Russell, L.M., Zhao, Y.L., Gentner, D.R., Weber, R.J., Goldstein, A.H., Jaoui, M., Offenberg, J.H., Kleindienst, T.E., Rubitschun, C., Surratt, J.D., Sheesley, R.J., Scheller, S., 2012. Secondary organic aerosol formation from fossil fuel sources contribute majority of summertime organic mass at Bakersfield. *Journal of Geophysical Research-Atmospheres* 117. <https://doi.org/10.1029/2012jd018170>
- Marjollet, A., Montelongo, M., Siong, P., Thao, C., Warner, D., 2015. *Guidance for Assessing and Mitigating Air Quality Impacts*.
- McLafferty, F.W., Turecek, F., 1993a. No Title, in: *Interpretation of Mass Spectra*. University Science Books, Sausalito, CA.
- McLafferty, F.W., Turecek, F., 1993b. No Title, in: *Interpretation of Mass Spectra*. University Science Books, Sausalito, CA.
- Meng, X., Wu, Z., Chen, J., Qiu, Y., Zong, T., Song, M., Lee, J., & Hu, M. (2024). Particle phase state and aerosol liquid water greatly impact secondary aerosol formation: Insights into phase transition and its role in haze events. *Atmospheric Chemistry and Physics*, 24(4), 2399–2414. <https://doi.org/10.5194/acp-24-2399-2024>
- Middlebrook, A.M., Bahreini, R., Jimenez, J.L., Canagaratna, M.R., 2012. Evaluation of composition-dependent collection efficiencies for the Aerodyne Aerosol Mass Spectrometer using field data. *Aerosol Sci. Technol.* <https://doi.org/10.1080/02786826.2011.620041>
- Mohr, C., DeCarlo, P.F., Heringa, M.F., Chirico, R., Slowik, J.G., Richter, R., Reche, C., Alastuey, A., Querol, X., Seco, R., Peñuelas, J., Jiménez, J.L., Crippa, M., Zimmermann, R., Baltensperger, U., Prévôt, A.S.H., 2012. Identification and quantification of organic aerosol from cooking and other sources in Barcelona using aerosol mass spectrometer data. *Atmospheric Chemistry and Physics* 12, 1649–1665. <https://doi.org/10.5194/acp-12-1649-2012>
- Mohr, C., Huffman, J.A., Aiken, A.C., Docherty, K.S., I.M.Ulbrich, Hannigan, M., Jimenez, J.L., 2009. Characterization of primary organic aerosol emissions from meat cooking, trash burning, and motor vehicles with high-resolution aerosol mass spectrometry and comparison with ambient and chamber observations. *Environ. Sci. Technol.* <https://doi.org/10.1021/es8011518>
- Mysliwiec, M.J., Kleeman, M.J., 2002. Source Apportionment of Secondary Airborne Particulate Matter in a Polluted Atmosphere. *Environ. Sci. Technol.* 36, 5376–5384. <https://doi.org/10.1021/es020832s>
- Nakayama, T., Suzuki, H., Kagamitani, S., Ikeda, Y., Uchiyama, A., Matsumi, Y., 2015. Characterization of a Three Wavelength Photoacoustic Soot Spectrometer (PASS-3) and a Photoacoustic Extinctionmeter (PAX). *J. of the Meteorological Society of Japan. Ser. II* 93. <https://doi.org/doi.org/10.2151/jmsj.2015-016>
- Ng, N.L., Canagaratna, M.R., Zhang, Q., Jimenez, J.L., Ulbrich, I.M., Kroll, J.H., Docherty, K.S., Chhabra, P.S., Bahreini, R., Murphy, S.M., Seinfeld, J.H., Hildebrandt, L., Donahue, N.M., DeCarlo, P.F., Lanz, V.A., Prévôt, A.S.H., Dinar, E., Rudich, Y., Worsnop, D.R., 2010. Organic aerosol components observed in Northern Hemispheric datasets from Aerosol Mass Spectrometry. *Atmos. Chem. Phys.* <https://doi.org/10.5194/acp-10-4625-2010>
- Ng, N.L., Chhabra, P.S., Chan, A.W.H., Surratt, J.D., Kroll, J.H., Kwan, A.J., McCabe, D.C., Wennberg, P.O., Sorooshian, A., Murphy, S.M., Dalleska, N.F., Flagan, R.C., Seinfeld, J.H., 2007. Atmospheric Chemistry and Physics Effect of NO<sub>x</sub> level on secondary organic aerosol (SOA) formation from the photooxidation of terpenes.
- NOAA/ESRL/GSL - RAOB [WWW Document], n.d. URL <https://ruc.noaa.gov/raobs/> (accessed 8.16.22).

- Nussbaumer, C. M., Cohen, R.C., 2021. Impact of OA on the Temperature Dependence of PM 2.5 in the Los Angeles Basin. *Environ Sci Technol*. <https://doi.org/10.1021/acs.est.0c07144>
- Nussbaumer, Clara M., Cohen, R.C., 2021. Impact of OA on the Temperature Dependence of PM 2.5 in the Los Angeles Basin. *Environ. Sci. Technol.* 55, 3549–3558. <https://doi.org/10.1021/acs.est.0c07144>
- Ortega, A. M., D. A. Day, M. J. Cubison, W. H. Brune, D. Bon, J. A. De Gouw, and J. L. Jimenez. 2013. “Secondary Organic Aerosol Formation and Primary Organic Aerosol Oxidation from Biomass-Burning Smoke in a Flow Reactor during FLAME-3.” *Atmospheric Chemistry and Physics* 13(22):11551–71. doi:10.5194/acp-13-11551-2013.
- Ortega, A.M., Hayes, P.L., Peng, Z., Palm, B.B., Hu, W., Day, D.A., Li, R., Cubison, M.J., Brune, W.H., Graus, M., Warneke, C., Gilman, J.B., Kuster, W.C., de Gouw, J., Gutiérrez-Montes, C., Jimenez, J.L., 2016. Real-time measurements of secondary organic aerosol formation and aging from ambient air in an oxidation flow reactor in the Los Angeles area. *Atmospheric Chemistry and Physics* 16, 7411–7433. <https://doi.org/10.5194/acp-16-7411-2016>
- Paatero, P., Tapper, U., 1994. Positive Matrix Factorization - a Nonnegative Factor Model with Optimal Utilization of Error-Estimates of Data Values. *Environmetrics* 5, 111-12.
- Palm, B.B., Campuzano-Jost, P., Ortega, A.M., Day, D.A., Kaser, L., Jud, W., Karl, T., Hansel, A., Hunter, J.F., Cross, E.S., Kroll, J.H., Peng, Z., Brune, W.H., Jimenez, J.L., 2016. In situ secondary organic aerosol formation from ambient pine forest air using an oxidation flow reactor. *Atmospheric Chemistry and Physics* 16, 2943–2970. <https://doi.org/10.5194/acp-16-2943-2016>
- Pearce, J.L., Beringer, J., Nicholls, N., Hyndman, R.J., Tapper, N.J., 2011a. Quantifying the influence of local meteorology on air quality using generalized additive models. *Atmospheric Environment* 45, 1328–1336. <https://doi.org/10.1016/j.atmosenv.2010.11.051>
- Pearce, J.L., Beringer, J., Nicholls, N., Hyndman, R.J., Uotila, P., Tapper, N.J., 2011b. Investigating the influence of synoptic-scale meteorology on air quality using self-organizing maps and generalized additive modelling. *Atmospheric Environment* 45, 128–136. <https://doi.org/10.1016/j.atmosenv.2010.09.032>
- Peng, J., Hu, M., Guo, S., Du, Z., Shang, D., Zheng, Jing, Zheng, Jun, Zeng, L., Shao, M., Wu, Y., Collins, D., Zhang, R., 2017. Ageing and hygroscopicity variation of black carbon particles in Beijing measured by a quasi-atmospheric aerosol evolution study (QUALITY) chamber. *Atmospheric Chemistry and Physics* 17, 10333–10348. <https://doi.org/10.5194/acp-17-10333-2017>
- Peng, J., Hu, M., Guo, S., Du, Z., Zheng, Jing, Shang, D., Zamora, M.L., Zeng, L., Shao, M., Wu, Y.S., Zheng, Jun, Wang, Y., Glen, C.R., Collins, D.R., Molina, M.J., Zhang, R., 2016. Markedly enhanced absorption and direct radiative forcing of black carbon under polluted urban environments. *Proceedings of the National Academy of Sciences of the United States of America* 113, 4266–4271. <https://doi.org/10.1073/pnas.1602310113>
- Peng, Z., Jimenez, J.L., 2019. KinSim: A Research-Grade, User-Friendly, Visual Kinetics Simulator for Chemical-Kinetics and Environmental-Chemistry Teaching. *J. Chem. Educ.* 96, 806–811. <https://doi.org/10.1021/acs.jchemed.9b00033>
- Perperoglou, A., Sauerbrei, W., Abrahamowicz, M., Schmid, M., 2019. A review of spline function procedures in R. *BMC Medical Research Methodology* 19, 46. <https://doi.org/10.1186/s12874-019-0666-3>
- Pfaffenberger, L., P. Barmet, J. G. Slowik, A. P. Praplan, J. Dommen, A. S. H. Prévôt, and U. Baltensperger. 2013. “The Link between Organic Aerosol Mass Loading and Degree of

- Oxygenation: An  $\alpha$ -Pinene Photooxidation Study.” *Atmospheric Chemistry and Physics* 13(13):6493–6506. doi:10.5194/acp-13-6493-2013.
- Pfannerstill, E.Y., Arata, C., Zhu, Q., Schulze, B.C., Ward, R., Woods, R., Harkins, C., Schwantes, R.H., Seinfeld, J.H., Bucholtz, A., Cohen, R.C., Goldstein, A.H., 2024. Temperature-dependent emissions dominate aerosol and ozone formation in Los Angeles. *Science* 384, 1324–1329. <https://doi.org/10.1126/science.adg8204>
- Pope, C.A., Thun, M.J., Namboodiri, M.M., Dockery, D.W., Evans, J.S., Speizer, F.E., Heath, C.W., 1995. Particulate Air Pollution as a Predictor of Mortality in a Prospective Study of U.S. Adults. *Am J Respir Crit Care Med* 151, 669–674. [https://doi.org/10.1164/ajrccm/151.3\\_Pt\\_1.669](https://doi.org/10.1164/ajrccm/151.3_Pt_1.669)
- Protecting Public Health in the San Francisco Bay Area, 2012.
- Puy, A., Piano, S.L., Saltelli, A., Levin, S.A., 2021. sensobol: an R package to compute variance-based sensitivity indices.
- R Core Team, 2021. R: A Language and Environment for Statistical Computing.
- R: Generalized additive models [WWW Document], n.d. URL <https://stat.ethz.ch/R-manual/R-devel/library/mgcv/html/gam.html> (accessed 8.17.22).
- Raizenne, M., Neas, L.M., Damokosh, A.I., Dockery, D.W., Spengler, J.D., Koutrakis, P., Ware, J.H., Speizer, F.E., 1996. Health effects of acid aerosols on North American children: pulmonary function. *Environmental Health Perspectives* 104, 506–514. <https://doi.org/10.1289/ehp.96104506>
- Rollins, A.W., Pusede, S., Wooldridge, P., Min, K.-E., Gentner, D.R., Goldstein, A.H., Liu, S., Day, D.A., Russell, L.M., Rubitschun, C.L., Surratt, J.D., Cohen, R.C., 2013. Gas/particle partitioning of total alkyl nitrates observed with TD-LIF in Bakersfield. *Journal of Geophysical Research: Atmospheres* 118, 6651–6662. <https://doi.org/10.1002/jgrd.50522>
- Saarikoski, S., Reyes, F., Vázquez, Y., Tagle, M., Timonen, H., Aurela, M., Carbone, S., Worsnop, D.R., Hillamo, R., Oyola, P., 2019. Characterization of submicron aerosol chemical composition and sources in the coastal area of Central Chile. *Atmospheric Environment* 199, 391–401. <https://doi.org/10.1016/j.atmosenv.2018.11.040>
- Sareen, N., Waxman, E. M., Turpin, B. J., Volkamer, R., and Carlton, A. G.: Potential of Aerosol Liquid Water to Facilitate Organic Aerosol Formation: Assessing Knowledge Gaps about Precursors and Partitioning, *Environmental Science & Technology*, 51, 3327-3335, 10.1021/acs.est.6b04540, 2017.
- Sareen, N., Carlton, A. G., Surratt, J. D., Gold, A., Lee, B., Lopez-Hilfiker, F. D., Mohr, C., Thornton, J. A., Zhang, Z., Lim, Y. B., and Turpin, B. J.: Identifying precursors and aqueous organic aerosol formation pathways during the SOAS campaign, *Atmospheric Chemistry and Physics*, 16, 14409-14420, 10.5194/acp-16-14409-2016, 2016.
- Sarratzadeh, M., Wildt, J., Pullinen, I., Springer, M., Kleist, E., Tillmann, R., Schmitt, S.H., Wu, C., Mentel, T.F., Zhao, D., Hastie, D.R., Kiendler-Scharr, A., 2016. Impact of NO<sub>x</sub> and OH on secondary organic aerosol formation from  $\beta$ -pinene photooxidation. *Atmospheric Chemistry and Physics* 16, 11237–11248. <https://doi.org/10.5194/acp-16-11237-2016>
- SB 535 Map, n.d.
- Schlosser, J.S., Braun, R.A., Bradley, T., Dadashazar, H., MacDonald, A.B., Aldhaif, A.A., Aghdam, M.A., Mardi, A.H., Xian, P., Sorooshian, A., 2017. Analysis of aerosol composition data for western United States wildfires between 2005 and 2015: Dust emissions, chloride depletion, and most enhanced aerosol constituents. *Journal of Geophysical Research: Atmospheres* 122, 8951–8966. <https://doi.org/10.1002/2017JD026547>

- Seinfeld, J.H., Pandis, S.N., 2016. Atmospheric chemistry and physics: from air pollution to climate change, Third edition. ed. John Wiley & Sons, Hoboken, New Jersey.
- Sirmollo, C.L., Collins, D.R., McCormick, J.M., Milan, C.F., Erickson, M.H., Flynn, J.H., Sheesley, R.J., Usenko, S., Wallace, H.W., Bui, A.A.T., Griffin, R.J., Tezak, M., Kinahan, S.M., Santarpia, J.L., 2021. Captive Aerosol Growth and Evolution (CAGE) chamber system to investigate particle growth due to secondary aerosol formation. *Atmospheric Measurement Techniques* 14, 3351–3370. <https://doi.org/10.5194/amt-14-3351-2021>
- Tingey, D.T., Manning, M., Grothaus, L.C., Burns, W.F., 1979. The Influence of Light and Temperature on Isoprene Emission Rates from Live Oak. *Physiologia Plantarum* 47, 112–118. <https://doi.org/10.1111/j.1399-3054.1979.tb03200.x>
- Ulbrich, I.M., Canagaratna, M.R., Zhang, Q., Worsnop, D.R., Jimenez, J.L., 2009. Interpretations of organic components from Positive Matrix Factorization of aerosol mass spectrometric data. *Atmos. Chem. Phys.* 9, 2891–2918.
- Understanding Particulate Matter: Protecting Public Health in the San Francisco Bay Area, 2012.
- US EPA, 2023. EPA Proposes to Strengthen Air Quality Standards to Protect the Public from Harmful Effects of Soot [WWW Document]. URL <https://www.epa.gov/newsreleases/epa-proposes-strengthen-air-quality-standards-protect-public-harmful-effects-soot> (accessed 4.21.23).
- Vasilakopoulou, C.N., Florou, K., Kaltsonoudis, C., Stavroulas, I., Mihalopoulos, N., Pandis, S.N., 2023. Development and evaluation of an improved offline aerosol mass spectrometry technique. *Atmospheric Measurement Techniques* 16, 2837–2850. <https://doi.org/10.5194/amt-16-2837-2023>
- Voliotis, A., Du, M., Wang, Y., Shao, Y., Alfara, M.R., Bannan, T.J., Hu, D., Pereira, K.L., Hamilton, J.F., Hallquist, M., Mentel, T.F., McFiggans, G., 2022. Chamber investigation of the formation and transformation of secondary organic aerosol in mixtures of biogenic and anthropogenic volatile organic compounds. *Atmospheric Chemistry and Physics* 22, 14147–14175. <https://doi.org/10.5194/acp-22-14147-2022>
- Vu, K.T., Dingle, J.H., Bahreini, R., Reddy, P.J., Apel, E.C., Campos, T.L., Digangi, J.P., Diskin, G.S., Fried, A., Herndon, S.C., Hills, A.J., Hornbrook, R.S., Huey, G., Kaser, L., Montzka, D.D., Nowak, J.B., Pusede, S.E., Richter, D., Roscioli, J.R., Sachse, G.W., Shertz, S., Stell, M., Tanner, D., Tyndall, G.S., Walega, J., Weibring, P., Weinheimer, A.J., Pfister, G., Flocke, F., 2016. Impacts of the Denver Cyclone on regional air quality and aerosol formation in the Colorado Front Range during FRAPPÉ 2014. *Atmospheric Chemistry and Physics* 16. <https://doi.org/10.5194/acp-16-12039-2016>
- Vutukuru, S., Griffin, R.J., Dabdub, D., 2006. Simulation and analysis of secondary organic aerosol dynamics in the South Coast Air Basin of California: SOA DYNAMICS IN SOUTHERN CALIFORNIA. *J. Geophys. Res.* 111, S12. <https://doi.org/10.1029/2005JD006139>
- Wang, Y., Ma, Y., Kuang, B., Lin, P., Liang, Y., Huang, C., Yu, J.Z., 2022. Abundance of organosulfates derived from biogenic volatile organic compounds: Seasonal and spatial contrasts at four sites in China. *Science of The Total Environment* 806, 151275. <https://doi.org/10.1016/j.scitotenv.2021.151275>
- Wood, S.N., 2011. Fast stable restricted maximum likelihood and marginal likelihood estimation of semiparametric generalized linear models: Estimation of Semiparametric Generalized Linear Models. *Journal of the Royal Statistical Society: Series B (Statistical Methodology)* 73, 3–36. <https://doi.org/10.1111/j.1467-9868.2010.00749.x>
- Wood, S.N., 2000. Modelling and smoothing parameter estimation with multiple quadratic penalties. *J. Royal Statistical Soc B* 62, 413–428. <https://doi.org/10.1111/1467-9868.00240>

- Wood, S.N., Pya, N., Säfken, B., 2016. Smoothing Parameter and Model Selection for General Smooth Models. *Journal of the American Statistical Association* 111, 1548–1563. <https://doi.org/10.1080/01621459.2016.1180986>
- Woody, M.C., Baker, K.R., Hayes, P.L., Jimenez, J.L., Koo, B., Pye, H.O.T., 2016. Understanding sources of organic aerosol during CalNex-2010 using the CMAQ-VBS. *Atmospheric Chemistry and Physics* 16, 4081–4100. <https://doi.org/10.5194/acp-16-4081-2016>
- Xu, N., Le, C., Cocker, D.R., Chen, K., Lin, Y.-H., Collins, D.R., 2024. An oxidation flow reactor for simulating and accelerating secondary aerosol formation in aerosol liquid water and cloud droplets. *Atmospheric Measurement Techniques* 17, 4227–4243. <https://doi.org/10.5194/amt-17-4227-2024>
- Xu, W., Li, Z., Lambe, A.T., Li, J., Liu, T., Du, A., Zhang, Z., Zhou, W., Sun, Y., 2022. Secondary organic aerosol formation and aging from ambient air in an oxidation flow reactor during wintertime in Beijing, China. *Environmental Research* 209, 112751. <https://doi.org/10.1016/j.envres.2022.112751>
- Zanobetti, A., Schwartz, J., Dockery, D.W., 2000. Airborne particles are a risk factor for hospital admissions for heart and lung disease. *Environmental Health Perspectives* 108, 1071–1077. <https://doi.org/10.1289/ehp.001081071>
- Zhang, H., Worton, D.R., Lewandowski, M., Ortega, J., Rubitschun, C.L., Park, J.-H., Kristensen, K., Campuzano-Jost, P., Day, D.A., Jimenez, J.L., Jaoui, M., Offenberg, J.H., Kleindienst, T.E., Gilman, J., Kuster, W.C., de Gouw, J., Park, C., Schade, G.W., Frossard, A.A., Russell, L., Kaser, L., Jud, W., Hansel, A., Cappellin, L., Karl, T., Glasius, M., Guenther, A., Goldstein, A.H., Seinfeld, J.H., Gold, A., Kamens, R.M., Surratt, J.D., 2012. Organosulfates as Tracers for Secondary Organic Aerosol (SOA) Formation from 2-Methyl-3-Buten-2-ol (MBO) in the Atmosphere. *Environmental Science & Technology* 46, 9437–9446. <https://doi.org/10.1021/es301648z>
- Zhang, Q., Jimenez, J.L., Canagaratna, M.R., Allan, J.D., Coe, H., Ulbrich, I., Alfarra, M.R., Takami, A., Middlebrook, A.M., Sun, Y.L., Dzepina, K., Dunlea, E., Docherty, K., DeCarlo, P.F., Salcedo, D., Onasch, T., Jayne, J.T., Miyoshi, T., Shimono, A., Hatakeyama, S., Takegawa, N., Kondo, Y., Schneider, J., Drewnick, F., Borrmann, S., Weimer, W., Demerjian, K., Williams, P., Bower, K., Bahreini, R., Cottrell, L., Griffin, R.J., Rautiainen, J., Sun, J.Y., Zhang, Y.M., Worsnop, D.R., Weimer, S., Demerjian, K., Williams, P., Bower, K., Bahreini, R., Cottrell, L., Griffin, R.J., Rautiainen, J., Sun, J.Y., Zhang, Y.M., Worsnop, D.R., 2007. Ubiquity and dominance of oxygenated species in organic aerosols in anthropogenically-influenced Northern Hemisphere mid latitudes. *Geophys. Res. Lett.* 34, L1380. <https://doi.org/10.1029/2007GL029979>
- Zhang, Q., Jimenez, J.L., Canagaratna, M.R., Ulbrich, I.M., Ng, N.L., Worsnop, D.R., Sun, Y., 2011. Understanding atmospheric organic aerosols via factor analysis of aerosol mass spectrometry: a review. *Anal. Bioanal. Chem.* 401, 3045–3067. <https://doi.org/10.1007/s00216-11-5355-y>
- Zhang, Q., Worsnop, D.R., Canagaratna, M.R., Jimenez, J.L., 2005. Hydrocarbon-like and oxygenated organic aerosols in Pittsburgh: insights into sources and processes of organic aerosols. *Atmos. Chem. Phys.* 5, 3289–3311.
- Zhang, Y., Favez, O., Petit, J.-E., Canonaco, F., Truong, F., Bonnaire, N., Crenn, V., Amodeo, T., Prévôt, A.S.H., Sciare, J., Gros, V., Albinet, A., 2019. Six-year source apportionment of submicron organic aerosols from near-continuous highly time-resolved measurements at SIRTa (Paris area, France). *Atmospheric Chemistry and Physics* 19, 14755–14776. <https://doi.org/10.5194/acp-19-14755-2019>
- Zhang, Y.P., Williams, B.J., Goldstein, A.H., Docherty, K., Ulbrich, I.M., Jimenez, J.L., 2014. A Technique for Rapid Gas Chromatography Analysis Applied to Ambient Organic Aerosol Measurements from the Thermal Desorption Aerosol Gas Chromatograph (TAG). *Aerosol Science and Technology* 48, 1166–1182. <https://doi.org/10.1080/02786826.2014.967832>

- Zhang, Z., Xu, W., Zeng, S., Liu, Y., Liu, T., Zhang, Y., Du, A., Li, Y., Zhang, N., Wang, J., Aruffo, E., Han, P., Li, J., Wang, Z., Sun, Y., 2024. Secondary Organic Aerosol Formation from Ambient Air in Summer in Urban Beijing: Contribution of S/IVOCs and Impacts of Heat Waves. *Environ. Sci. Technol. Lett.* 11, 738–745. <https://doi.org/10.1021/acs.estlett.4c00415>
- Zhao, Y., Kreisberg, N.M., Worton, D.R., Isaacman, G., Gentner, D.R., Chan, A.W.H., Weber, R.J., Liu, S., Day, D.A., Russell, L.M., Hering, S.V., Goldstein, A.H., 2013. Sources of organic aerosol investigated using organic compounds as tracers measured during CalNex in Bakersfield: SOURCES OF ORGANIC AEROSOL. *J. Geophys. Res. Atmos.* 118, 11,388-11,398. <https://doi.org/10.1002/jgrd.50825>
- Zhu, S., Horne, J.R., Mac Kinnon, M., Samuelsen, G.S., Dabdub, D., 2019. Comprehensively assessing the drivers of future air quality in California. *Environment International* 125, 386–398. <https://doi.org/10.1016/j.envint.2019.02.007>
- Zhu, Z., Du, X., Collins, D.R., 2025. Direct measurement of the growth of small particles in ambient air using captive aerosol chambers. *Atmospheric Environment* 340. <https://doi.org/10.1016/j.atmosenv.2024.120915>